Fundamentals of the growth mechanism, tailored properties and applications of 3D hollow carbon foams

Vom Promotionsausschuss der

Technischen Universität Hamburg

zur Erlangung des akademischen Grades

Doktor-Ingenieur (Dr.-Ing.)

genehmigte Dissertation

von

Janik Marx

aus Hermeskeil

2019

Vorsitzender: Prof. Dr. rer. nat. Patrick Huber

(Hamburg University of Technology)

Gutachter: Prof. Dr.-Ing. habil. Bodo Fiedler

(Hamburg University of Technology)

Prof. Dr. rer. nat. Rainer Adelung

(Kiel University)

Tag der mündlichen Prüfung: 14. Mai 2019

Technisch-Wissenschaftliche Schriftenreihe

Acknowledgement

I

Kurzzusammenfassung

Durch die Entdeckung von Kohlenstoffnanostrukturen (1D, 2D Strukturen) im vergangenen Jahrhundert begann in den darauffolgenden Jahren ein Wettlauf zur Verwendung dieses neuen Werkstofftyps mit herausragenden physikalischen Eigenschaften. Aufgrund der geometrischen Beschränkung von 1D und 2D Kohlenstoffstrukturen wurden um die Jahrtausendwende verschiedenste Herstellungstechniken entwickelt, um 3D Kohlenstoffstrukturen zu synthetisieren, welche auch als Kohlenstoffschäume bezeichnet werden. Diese bieten auf Basis deren Morphologie gegenüber den bisherigen Strukturen entscheidende Vorteile, womit sich potentiell neue Anwendungsgebiete im Bereich der Energiespeichersysteme und Katalysatoren ergeben. Dabei beeinflussen insbesondere die Wachstumsmechanismen der Kohlenstoffstrukturen die späteren Eigenschaften. Im Zuge dessen entstehen in der Ausbildung der Kohlenstoffanordnung im hexagonalen Gitter immer wieder Defekte, welche die elektrischen und mechanischen Eigenschaften der Struktur verringern. Diese Defekte können durch Ausheilungsprozesse wie eine Hochtemperaturbehandlung verringert werden. Neben Defekten, wurde auch gezeigt, dass die Anzahl der Kohlenstofflagen die Eigenschaften maßgeblich beeinflussen. Diese Arbeit befasst sich mit der Analyse des Wachstumsmechanismus der 3D Kohlenstoffstruktur Aerographit. Dieser Kohlenstoffschaum weist eine tetrapodischen Morphologie auf und zeichnet sich durch dessen hohe mechanische und elektrische Eigenschaften bei einer geringen Dichte von bis ~ 2 mg/cm³ aus. Im Zuge dessen wird vor allem der Einfluss des Wachstumsmechanismus auf die Eigenschaften beziehungsweise die kontrollierte Veränderung der Eigenschaften wie zum Beispiel der elektrischen Leitfähigkeit untersucht. Dabei kann durch eine gezielte Prozessführung, während der Synthese

von Aerographit in der chemischen Gasphasenabscheidung, die Wandstärke der Tetrapoden gezielt variiert werden. Wobei durch eine nachgeschaltete Temperaturbehandlung von Aerographit, in Abhängigkeit der Temperatur und deren Haltezeit, kommt es zu einer schrittweisen Steigerung der elektrischen Leitfähigkeit. Weiterhin wird in dieser Arbeit eine Variation der Morphologie und des Herstellungsprozesses für 3D Kohlenstoffschäume untersucht. Dabei liegt das Hauptaugenmerk auf eine anwendungsbezogene Morphologie und eines vergleichsweise vereinfachten Herstellungsprozesses der neu entwickelten Kohlenstoffstruktur. Der dabei entwickelte Kohlenstoffschaum weist eine globulare Morphologie auf und wird auf Basis eines keramischen Grundkörpers hergestellt. Durch dieses Herstellungsverfahren lassen sich unter Verwendung von thermodynamischen Berechnungen katalytisch aktive Materialien dem keramischen Grundkörper zufügen, welche gezielt nach dem CVD Prozess in dem gebildeten Kohlenstoffschaum verbleiben. Dabei kann diese Methode zu einem beliebig vielfältigen Anwendungsspektrum im Bereich der Katalysatoren führen

Abstract

The discovery of 1D carbon nanostructures in the 20th century and subsequently of 2D carbon nanostructures in the past century, a competition for possible applications of this material with outstanding physical properties began. Due to the geometric restriction of 1D and 2D carbon structures, a variety of manufacturing techniques have been developed around of the millennium to synthesise 3D carbon structures, which are also referred to as carbon aerogels or carbon foams. Based on their morphology, these structures offer decisive advantages over the existing structures and thus potentially new fields of application arise in the field of energy storage systems and catalysts. The growth mechanism of carbon structures has a property-defining influence on their properties. During their growth, carbon atoms arrange in ideal hexagonal lattices, which can also lead to defects that adversely affect the properties. These defects can be reduced by annealing processes such as a high-temperature treatment. Besides to defects, it was also shown that the number of carbon layers significantly affect the properties.

This work concerned with the analysis of the growth mechanism of the 3D carbon structure Aerographite. This carbon foam has a tetrapodal morphology and is distinguished by its high mechanical and electrical properties at a density down to ~2 mg/cm^3. Here, the influence of the growth mechanism via ex-situ studies and the tailoring of the properties such as electrical conductivity is investigated. The wall thickness of the tetrapods can be specifically varied by means of a targeted process control during the synthesis of Aerographite in the CVD process. A stepwise increase in the electrical conductivity occurs because of a subsequent temperature treatment of Aerographite, as a function of the temperature and its

holding time. Additionally, the healing of Aerographite by a thermal treatment and the influence of the graphitisation on the properties of Aerographite is in focus in this work.

Furthermore, this study aims a variation of the morphology and the manufacturing process for 3D carbon foams and the identification of possible applications. The focus here is on an application-related morphology and a comparatively simplified manufacturing process of the carbon structure. The developed carbon foam has a hierarchical globular morphology and is produced based on a porous ceramic template. Based on thermodynamic calculations, a wide range of catalytically active materials can be added to the green body, which are remains after the CVD process. Finally, a carbon foam with incorporated catalysts can be used for several applications.

Table of Contents

VIII

List of Symbols and Abbreviations

Symbol	Unit	Description
Symbols and Constants		
C	F	Capacity
E	Pa	Young´s modulus
E_G	eV	Band gap energy
F	N	Force
g	%	Degree of graphitisation (Raman)
g_{XRD}	%	Degree of graphitisation based on XRD
G	%	Degree of graphitisation (Raman)
K_{IC}	$MPa·m^{1/2}$	Fracture toughness
Δl	mm	Change in length
L_a	nm	Crystalline width
L_0	mm	Initial length
λ	cm^{-1}	Raman Shift
R	Ω	Electrical resistance
$R_{contact,n}$	Ω	Resistance between two tetrapods

X

$R_{composite}$	Ω	Electrical resistance of Aerographite-epoxy composites
$R_{cov,n}$	Ω	Resistance of a covalent bond between two tetrapods
$R_{t,n}$	Ω	Resistance of the single tetrapods
$T_{tunnel,n}$	Ω	Tunneling resistance of two tetrapods
S_L	cm³	Longitudinal shrinkage
S_V	cm³	Volume shrinkage
σ		Sigma bonds
σ	S/m	Electrical conductivity
σ_{CCD}		Charge carrier density
σ_C		Electrical paths
σ_{DD}		Defect density
σ_S		Surface defects
σ_t		Tunneling effect
T	°C	Temperature
θ	°	Peak position
vol%	%	Volume percent
wt%	%	Weight percent

Abbreviations

AG	Aerographite
Au	Gold
C	Carbon
C_{area}	Area under crystalline peak after background removal
Co	Cobalt
CFD	Computational Fluid Dynamics simulation
CH_4	Methane
C_nH_m	Carboxy groups
CNT	Carbon Nanotube
Cu	Copper
CVD	Chemical vapour deposition
D	D-band
D´	D´-band
EDLC	Electric double-layer capacitor
EELS	Electron energy loss spectroscopy

ETEM	Environmental transmission electron microscopy
FLG	Few-layer graphene
F_{area}	Area of the obtained diffractogram before background removal
Fe	Iron
G	G-band
G´	G´-band
GaN	Gallium nitride
GG	Globugraphite
GNs	Graphene nanosheets
GNRs	Graphene nanoribbons
HAADF	High Angle Annular Dark Field
HOPG	Highly oriented pyrolytic graphite
H_2	Hydrogen
H_2O	Water
Mg	Magnesia
MgO	Magnesium oxide
Ni	Nickel

NLDFT	Non-local density functional theory
Pd	Palladium
PNC	Polymer nanocomposite
PVB	Polyvinyl butyral
QSDFT	Quenched solid density functional theory
R	D/G ratio – defect density
RBM	Radial breathing mode
SEM	Scanning electron microscopy
SLG	Single-layer graphene
STEM	Scanning transmission electron microscopy
TEM	Transmission electron microscopy
TGA	Thermogravimetric analysis
Ti	Titanium
TiO_2	Titania
XRD	X-ray diffraction
Zn	Zinc
ZnO	Zinc oxide

1   Introduction

For centuries, carbon modifications, such as carbon nanotubes (CNTs), have been used unintended as additional reinforcing elements in a metal matrix material to improve their mechanical properties, as shown for a damascene sword from the 17th century. These CNTs are synthesised unintentionally during the manufacturing using high temperatures and pressure and the presence of iron as catalyst [1]. After the introduction of carbon nanotubes in the 1950s [2] and their detailed description and confirmation at the end of the 20th century by Iijima [3] carbon nanostructures have become increasingly important. In addition to carbon nanotubes, other carbon modifications such as fullerenes [4,5] and graphene [6,7] have been discovered at the same time. Carbon nanostructures can be used in various fields of applications, e.g. sensors [8], bioimplantats [9], composites [10–12], batteries [13], thermoelectric devices [14,15] or as basis for catalysts with incorporated metallic nano particles [16–18].

The basis for the development of such fields of application is the deepening understanding of the growth behaviour, in which the kinetics of the synthesis of carbon nanostructures are analysed via ex-situ analysis using electron microscopy methods [19,20]. The development of new analytical methods such as the environmental transmission electron microscopy (ETEM) allows in-situ analysis of such growth processes [21–23]. Although ex-situ analysis is a powerful tool for the description of growth processes. But to clarify the influence of catalysts or the formation of graphitic layers for a more detailed observation of such growth processes, an in-situ analysis of these mechanisms are indispensable [24–26].

Due to the geometric limitations of the mentioned structures, the development of 3D cross-linked carbon structures was the next evolutionary step. A variety of manufacturing methods is developed to synthesise carbon foams. Based on this a new field of research emerges.

The manufacturing of these newly developed 3D carbon structures can be distinguished in template-based and template-free methods for the direct synthesis of carbon aerogels [27–29] and the assembly of graphitic structures [30–32]. The recently developed structure, called Aerographite (AG), offers a high application potential by its outstanding electrical and mechanical properties. Depending on the density, different morphologies can be observed, and each substructure has unique properties [28]. The so-called closed-shell variant of Aerographite appears to be particularly interesting for technical applications such as the growth of nerve cells [33], as reinforcing filler in polymer nanocomposites (PNCs) [34,35], as gas sensors [36], as supercapacitors [37] or as basis for the growth of gallium nitride structures (GaN) [38]. The description of the growth mechanism, by means of ex-situ or in situ methods, may reveal new possibilities to understand fundamental properties of Aerographite and to optimize or tailor them according to specific requirements. The basic structure-property relation of Aerographite regarding the technological application are still unknown. For example, in CNTs, the number of layers [39,40] and the degree of graphitisation [41–44], have a considerable influence on the electrical and mechanical properties of carbon structures. In the course of this, the explanation of the fundamental electrical character of Aerographite is of particular interest.

1.1 Aim of the work

This work investigates the growth mechanism of Aerographite via ex-situ methods, which is essential for the further understanding for the tailoring of properties.

Based on the observed mechanism and the proposed model, properties such as the electrical and mechanical properties can be tailored by varying the wall thickness of Aerographite in an adapted synthesis scheme. Moreover, atomic defects were healed in a subsequently treatment process.

As an alternative to the tetrapodal morphology of Aerographite, a new structure with a hierarchical-globular morphology is developed for special applications in the field of catalysts. In this thesis, the fundamentals of the 3D carbon capacitors and the synthesis of the carbon-based catalysts are presented.

1.2 Structure of the Thesis

This thesis is divided in 6 chapters. In the first chapter, carbon structures, their growth mechanism and their properties are described. Followed by the explanation of 3D carbon foams and their applications. Chapter 3 describes the design of the experiments, the used materials and sample geometries, the development of a manufacturing process for ceramic-based templates and the used experimental set-up for the analytical observations. The results of the experiments are presented and discussed in chapter 4. The focus is set on the growth mechanism of Aerographite, its properties modifications and the applications of the new developed carbon morphology. The following chapter summaries the main findings. Chapter 6 contains an outlook of this thesis for further research in the field of 3D carbon foams and their applications.

Results of this thesis and the DFG project cooperation have been published in several journal articles or have been presented on conferences, or have to be submit to journals, as listed on page 89-92. Moreover, all student thesis with a deep impact on this thesis are summarised on page 93.

2 Scientific and technological background

This chapter explains the scientific and technological background, which is necessary for the understanding of the present thesis. Carbon structures, their manufacturing methods or the corresponding growth models and possible fields of application are considered. Based on this, specific modifications of carbon structures are discussed using graphene and CNTs as an example.

Furthermore, the characterisation of carbon structures from graphene, via CNTs to 3D carbon structures, using Raman spectroscopy and the explanation of the formation of characteristic Raman peaks are important. The manufacturing variants of 3D carbon structures as well as the targeted properties of carbon structures.

2.1 Carbon structures (growth models, properties and applications)

Carbon structures such as graphene [6,7], fullerenes [4] or carbon nanotubes [2] rise in importance in the last few decades. This new class of materials can be produced in several manufacturing processes, but the most economically and one of the promising processes for the industrial production of carbon structures is the CVD process.

2.1.1 Graphene

Graphene is a single layer of graphite and the basic carbon modification of fullerenes and CNTs, as shown in Figure 2.1. These carbon structures can be formed by rolling up or folding a graphene sheet. The first description of graphene as carbon allotrope is from the 1940s and described the possible potential in their electrical/mechanical properties [45]. Due to the isolation of graphene monolayers by *Geim* and *Novoselov* [6] at the beginning of the 21th century, the exploration of carbon nanostructures increased the importance

even more. Due to the planar structure consisting of sp² carbon bonding, graphene exhibits high mechanical (1 TPa) [46], thermal >5000 W/mK [47] and electrical properties with a calculated electrical resistivity of approximately 1.0 μΩcm [7].

Graphene offers a high application potential such as e.g. in polymer composites for increasing electrical/mechanical properties [48,49], as energy storage systems [50] such as supercapacitors [51], as fuel cells [52], as bio sensors [53] or in photovoltaic cells [54].
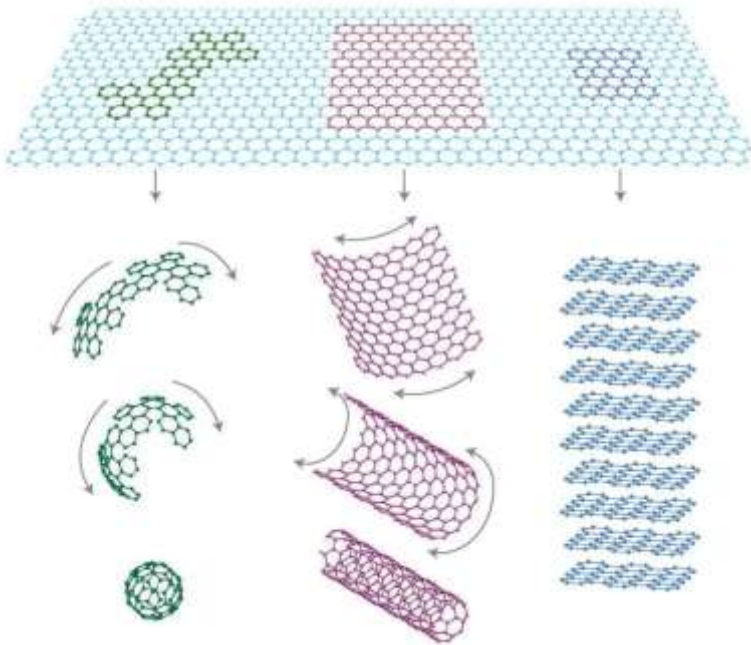
Figure 2.1: Graphene as fundamental structure for carbon allotropes [7].

Technologically, a distinction can be made between single-layer graphene (SLG), few-layer graphene (FLG), graphene nanosheets (GNs) and graphene nanoribbons (GNRs) [53]. An electrical resistance of approx. 3.35 µΩcm was calculated for FLG [55], whereby graphene exhibits individual properties as a function of the number of layers. Furthermore, graphene shows a temperature-dependent electrical behaviour, whereby the conductivity increases with increasing temperature, which is described as semiconductive behaviour [56].

The electrical conductivity of graphene decreases continuously with an increasing number of layers from $0.8 \cdot 10^6$ S/m (2 layers) to $0.18 \cdot 10^6$ S/m (9 layers) [55]. This behaviour can be also observed for the thermal conductivity. The change in the thermal conductivity with increasing number of layers is explained by the change in the phonon dispersion and thus in more resulting phonon states for "Umklapp skattering" [57,58]. An increased number of layers from 2 to 10 layers leads also to a reduction of the Young modulus from 980 GPa to 940 GPa, respectively. This is explained by the weaker van der Waals forces between the individual layers, which makes FLG unstable [59].

Growth model of graphene

Graphene can be synthesised by various manufacturing methods. These can be distinguished into two basic procedural principles, the chemically derived from graphite [60,61] which are followed by sonication and the synthesis in the CVD process [62] with metals as substrate. Similar to CNTs, the same catalysts are used to synthesise graphene (see Chapter 2.1.2), such as copper (Cu) or nickel (Ni) [63,64].

The synthesis of graphene takes place in several steps, as shown in Figure 2.2a,b. The different solubility of carbon into the substrates (nickel (a) and copper (b)) leads to a difference between the growth mechanism [64]. *Wang et al.* reported that the growth of graphene begins preferably at the grain boundaries of the substrate on its surface [65].

By using nickel as substrate (Figure 2.2a), first the adsorption of carbon precursors occurs (1), followed by the dehydrogenation on the substrate surface (2). In the next step carbon diffuse into and through to the substrate material (3). At energetically favorable points takes the diffusion to the substrate surface place (4). Finally, the segregation process of graphene starts. Whereas, copper is used as substrate for the growth of graphene, as shown in Figure 2.2b, desorption of precursors occurs on the substrate surface (1). The segregation process of graphene takes place immediately, without any diffusion process (2) [64].

(a)

Bulk-mediated growth, Ni

(b)

Surface-mediated growth, Cu
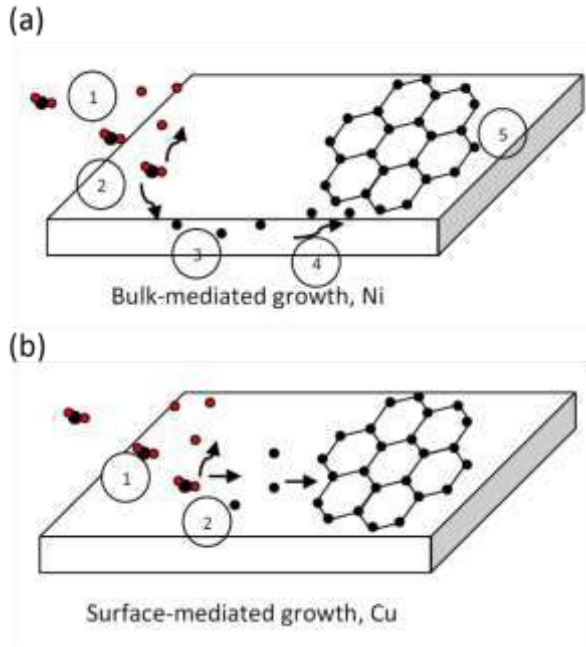
Figure 2.2: Schematic growth mechanism of graphene in the CVD process on a nickel substrate (a) and on a copper substrate (b) [64].

Based on the chemical reactions of the precursor (methane - CH_4) and the dehydrogenation of methane on the surface (s), with injected hydrogen (H_2) according to equation 2.1, 2.2 and the chemisorption of hydrogen on the substrate surface [64], hydrogen has a decisive influence on the quality of graphene.

$$CH_4(g) \rightarrow CH(s) + 4H(s) \qquad (2.1)$$

$$H_2(g) \rightarrow (s) + 2\,H(s) \qquad (2.2)$$
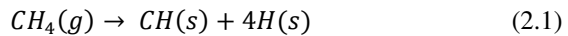
The presence of hydrogen is important for the synthesis of graphene. It was shown that hydrogen reduces the crystallinity and the growth rate of graphene especially on copper [66]. In addition, other studies show that the synthesis of graphene cannot work without the presence of water, because it acts as an activator of the surface and as an etching reagent [67].

2.1.2 Carbon Nanotubes

Carbon nanotubes are another allotropy of carbon and can be described as a rolled-up graphene sheet. Carbon nanotubes can be distinguished between single wall (a-SWCNT), double wall (b-DWCNT) and multi wall (c-MWCNT) carbon nanotubes as shown in Figure 2.3. Since their discovery in the 1950s [2] and their description by *Iijima* approx. 40 years later [3], these structures have become increasingly more researched to identify application fields and to improve already known materials in their properties with CNTs. Because of the C-C bonds and their σ orbitals in the plane direction, CNTs have a high potential in the formation of mechanical, thermal and electrical properties. Additionally, the remaining p-orbital forms a π-bond perpendicular to the CNT direction. By this sp^2 hybridization, the carbon atoms arrange in hexagonal lattices. However, this requires a zero-defect packing of the carbon atoms. In particular, the growth mechanism of CNTs has a considerable influence on the formation of physical properties by formation of defects such as bonding, hybridisation or lattice defects, such as sp^3 orbitales [68]. Experimental studies have shown that CNTs, like graphene, also have high electrical conductivity [69] and high mechanical [70] properties. For defect-free CNTs a theoretically Young modulus of ~1 TPa is calculated [71].

Studies on the influence of defects in CNTs shown a decrease of the mechanical properties [72,73]. The strength and the failure strain can be

reduced by as much as 46 % and 80 % [72] and the tensile strength by 60 % [73]. Based on the presence of defects, the strength of CNTs can be reduced up to 36 GPa [74].
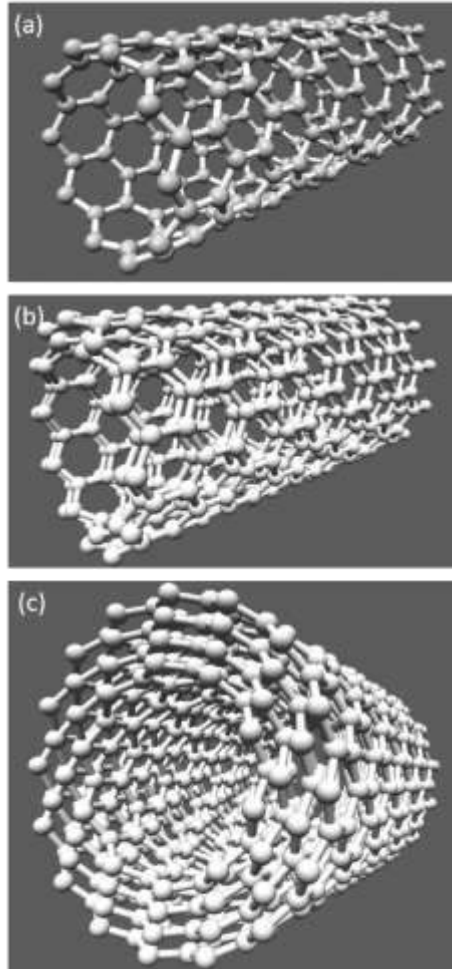
Figure 2.3: CNT modifications: SWCNT (a), DWCNT (b), MWCNT (c).

The wall thickness, or rather the number of carbon layers has an influence of the properties. It could be shown that with increasing wall number the electrical conductivity of CNTs increases and a plateau is reached, which is confirmed by the decrease of the calculated reduction of the band gap energy [40]. The mechanical stiffness of CNTs was simulated and showed that with increasing wall number the Young modulus decreases [75]. Based on the measured specific resistance ρ_R of CNTs films, the band gap energy E_g of CNTs can be calculated with a simple relation with the present temperature T and the Boltzmann constant k_B as shown in equation (2.3). The band gap energy is reduced with increasing number of layers [39].

$$\rho_R = \exp(E_g/2k_B \cdot T) \qquad (2.3)$$

Growth model of carbon nanotubes

The growth of CNTs is observed via electron microscopic methods. Based on these observations the first growth models were created by *Iijima* in the early 1990s [19,20]. On the basis of these models and new analytical methods such as the ETEM [23], the growth of CNTs during their synthesis was observed more in detail.

Three methods have proven as particularly suitable for the production of CNTs. Especially the arc discharge [76] and laser vaporisation [77] is suitable for large scale production of CNTs [78]. In addition, the use of the CVD process [79] is also applied to synthesise CNTs. The growth of CNTs is divided into two different mechanisms. On the one hand the base-growth which also called as extrusion or root growth and the tip-growth mechanism [22,80]. For both mechanisms the presence of a catalyst required. As a catalyst for CNT growth, predominantly metals are used, eg. Fe, Ni, Co [81]

as well as ZnO [82], Au [83], Ni/SiO$_2$ [25], which are introduced during the synthesis.

Both growth mechanisms in the CVD process are based on a physically fundamental mechanism that is described in Figure 2.4a. In the first step, the gaseous hydrocarbon molecules are adsorbed on the catalyst surface (1). Whereupon the dissociation of the precursor (2) and its diffusion on or into the surface of the metal catalyst (3) is followed. Finally, the nucleation and the formation of the carbon structure (4) take place [84]. As described by *Lo et al.* base-growth (Figure 2.4b) or the tip-growth mechanism (Figure 2.4c) depends on the ratio of the substrate temperature T_S to the gas temperature T_G. If T_S is higher than T_G, the base-growth mechanism is dominant, whereas T_G is higher than T_S tip-growth mechanism follows [85]. The basics of the CVD process are described in chapter 2.3 in detail.
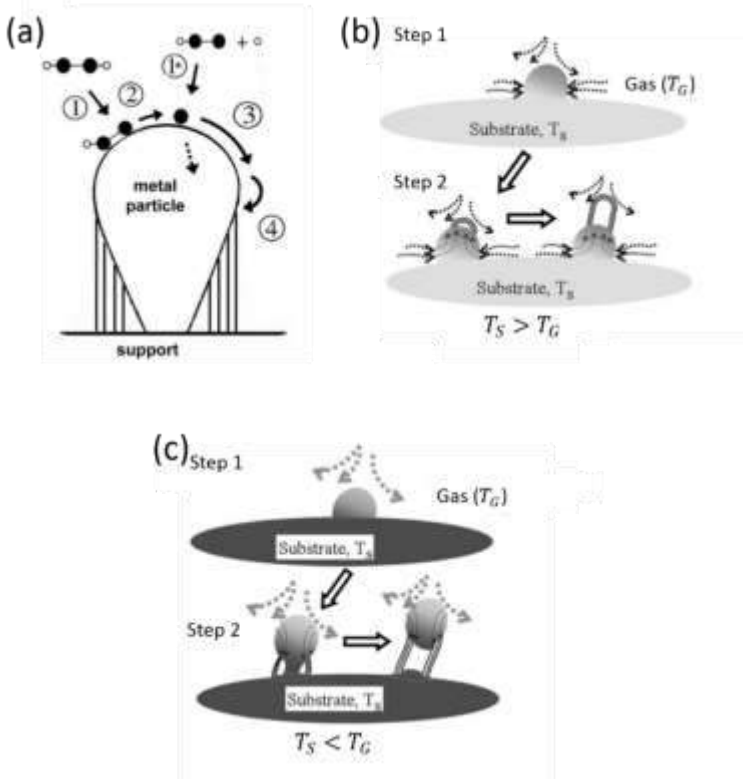
Figure 2.4: Growth model for CNTs (a) [84], growth model for the base-growth mechanism (b) and growth model for the tip-growth mechanism (c) after [85].

Besides to experimental studies, analytical studies, using Computational Fluid Dynamics (CFD) simulation is an effective tool to determine temperature and flow behaviour in the CVD process for the production of CNTs and gained in importance of their description [86,87]. Based on these data, the process can be optimised to generate CNTs of a higher quality [87].

2.1.3   Overview of Raman spectroscopy on carbon structures

For fundamental characterisations of carbon structures and their structure-property relations, Raman spectroscopy has emerged as an effective analysis method over the past decades. Raman spectroscopy provides the possibility of the effects of various treatment methods, such as doping [88,89], functionalisation [90–92], graphitisation of carbon structures [41–44] or the number of layers [40,93] in relation to the resulting properties. However, the penetration depth of laser using during Raman measurements is in the range of few nanometers [94].

Characteristic for sp^2 hybridized carbon structures is the so-called G-band, which is about 1550-1605 cm^{-1} and the so called G'-band or 2D- band between 2500 and 2800 cm^{-1} [95–98], as shown in Figure 2.5a.

The G-band stands for the in-plane oscillation of the carbon atoms at which they move towards each other and can be referred to as C-C stretching mode [96]. Ideally, the peak for pure carbon materials is at 1582 cm^{-1} as described for graphite [98]. The existence of the G'-band indicates a high orientation of carbon atoms in hexagonal lattices and is based on electron-photon and electron-phonon interactions. Therefore this band is referred to as second order Raman scattering, whereas the formation of the G-band is only based on an interaction and can thus be regarded as first order Raman scattering [96,98].

The atomic order of sp^2-hybridised carbon is disturbed by defects such as, lattice defects, which leads to a further band, as can be seen in the Raman spectra. This so-called D-band is located at ~1350 cm^{-1} [95–98] (Figure 2.5a-damaged graphene). The intensity and position of the D-band as described by *Behler et al.* has in particular been dependent on the energy of the used laser [42]. In this case, the intensity ratio is used on D-band and G-band in order

to detect structural changes [98,99] which are determined by the above-mentioned treatment methods and can be referred to as defect densities. A pronounced formation of the D-band indicates the presence of sp^3-hybridized carbon [100]. Especially in the case of SWCNTs, the formation of the radial breathing mode (RBM) occurs between 50 cm^{-1} and 700 cm^{-1} (Figure 2.5a). This is an out-plane oscillation of the carbon atoms and occurs only in closed structures such as CNTs [96–98].

For metallic or semiconducting CNTs, a different formation of the G-band in the Raman spectrum occurs as shown in Figure 2.5b. The metallicity of CNTs results in a wide G-band formation compared to semiconducting CNTs. The thermal treatment of carbon structures such as thermal annealing leads to a structural change at atomic level, which affects the formation of Raman spectra. This is explained in detail more in 2.3.1.
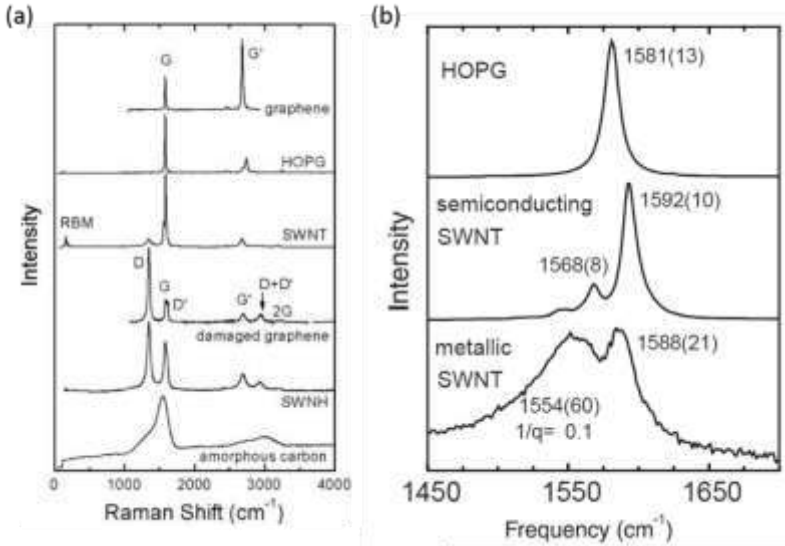
Figure 2.5: Raman spectra of different carbon structures (a) [95,98], Raman spectra of highly orientated pyrolytic graphite (HOPG) metallic and semiconductive SWCNTs (b) [95].

2.1.4   3D carbon foams -synthesis and applications-

3D carbon structures are characterised by their low densities coupled with high specific surfaces. Based on these facts they are called as carbon aerogels or carbon foams. Due to their 3-dimensional morphology, these structures have an extraordinarily high potential in the future compared to graphene or CNTs regarding to their properties and associated potential application fields. These 3D carbon structures consist in their substructure of CNTs or graphene, which can be produced by various methods.

Synthesis of 3D carbon foams

Since the description of carbon aerogels at the end of the 1980s by *Pekala* [101], carbon aerogels steadily gain in importance. The first aerogels were produced based on a sol-gel process with a subsequent freeze-drying [101]. According to *Campbell* [102], different synthesis methods for the manufacturing of 3D carbon aerogels can be distinguished in three synthesis methods, the direct synthesis, the template-free assembly of graphitic structures or a precursor conversion. Table 2.1 shows a summarised overview about the manufacturing methods for 3D carbon foams.

The direct synthesis of carbon aerogels is based on template or template-free manufacturing processes. However, the template-based methods can further split in a removal mechanism of the template via etching or reduction, such as in Aerographite [28]. The most favorable method to synthesise carbon aerogels is based on the removal of the template by etching after the carbon deposition and the reapplication of the template morphology, usually using nickel [27,103–109], metal oxide foams [110] or hybrid materials [111]. Carbon aerogels can also be produced template-free by interconnection of CNTs [29,112] or carbon nanofibers (CNFs) [113].

The assembly of graphitic structures is one of the most promising methods for the synthesis of carbon aerogels. This production method can be subdivided into a template-based [30,114–118], template-free [31,32,101,119–129] or substrate-based [130] synthesis. The methods have in common the use of graphene, graphene oxide and CNTs, which are first dissolved in a solution. In the case of template-based methods, these particles are deposited on the substrate surface and then dried [30,114–116]. Thereupon, the template is removed by an etching process or remains as a hybrid in the structure.

One of the most promising methods for the production of 3D carbon aerogels is the synthesis via sol-gel freeze drying [31,101,119–124]. Additionally, hybrids with metal oxides [125–127] or CNTs [128] can be used for manufacturing. These methods are based on the mixing used resorcinol and formaldehyde mixture and the gelation of this mixture and supercritical drying. In a last step this aerogel is pyrolysed in a tube furnace to get a carbon aerogel as reported by *Pekala* [101]. The structure of these aerogels is randomly oriented and consist of interconnected graphene sheets. Several groups developed a manufacturing method for 3D carbon aerogels based on a single step freeze drying process [32,129].

Table 2.1: Extract from the overview of different manufacturing process of 3D carbon foams after Campbell [101].

Direct synthesis of carbon aerogel	With template	Template removal by etching	Graphene on nickel foam [27,103-109] Graphene on metal oxides [110] Hybrid structure [111]
		Template removal during by reduction	Aerographite [28]
	No template		CNT sponges [29,112]

			CNF sponge [113]
Assembly of graphitic structures	With template	Without removal of the template	Graphene on nickel foam [30,114–116] Graphene on aluminum oxide foam [117]
		Removal of template by etching	CNF aerogel [118]
	No template	Sol gel process with subsequent freeze drying	Graphene aerogels [31,101,119-124] Hybrids with metal oxides [125-127] Hybrids with CNTs [128]
		Freeze drying	Graphene oxide sponge [32,129]
	On a substrate		Graphene aerogel assembled on Zn foil [129]

Especially the development of the synthesis of Aerographite [28,131] which is based on the replication of the template morphology in the CVD process,

shows an important impact on the research of 3D carbon foams. Therefore, the fundamentals of the CVD process are discussed in chapter 2.2. In this unique manufacturing method, ZnO is reduced and removed, so that only a hollow carbon shell remains. However, the occurred replication process in its details is still unknown. This replication process was modified by varying the carbon supply rate, which resulted in different densities and sub-morphologies [28].

These modifications in the morphology of Aerographite are resulting in different properties [35]. The density of Aerographite increases with increasing supply of carbon source. Thereby evolving the morphology from a hollow-framework over a closed-shell to closed-shell filled variant. Resulting of the increased density, the compressive Young´s modulus and the electrical conductivity of Aerographite increases as well [35]. The phenomenon that with increasing density the mechanical properties increase at the same time is already described for foams by *Ashby* [132]. This linear correlation of the modulus and the electrical conductivity is related to the interconnection of single Aerographite tetrapods [35].

Applications for 3D carbon foams

Based on their high specific surface areas (SSAs) and low densities 3D carbon structures are particular suitable for supercapacitors [30,31,37,124,133], fuel cells [103], lithium Ion batteries [109], electromagnetic interference shielding [134] or catalysts [135–140]. Whereas, supercapacitors and catalysts are the most promising applications for 3D carbon structures and are therefore described in more detail below.

Due to the storage mechanism supercapacitors, which are referred as electric double-layer capacitor (EDLC), are characterised by low charge and discharge times at high specific power densities of 15 kW/kg compared to conventional energy storage systems such as Li-ion accumulators (2 kW/kg) [140]. However, EDLCs have comparatively low specific energy densities. EDLCs are suitable for applications in stationary or mobile systems such as car acceleration, emergency systems, and tramways. They are characterised by their long service life, which results from the number of charging and discharging cycles [141]. Electrochemical properties of carbon-based supercapacitors are summarised in Table 2.2. For carbon aerogels, capacities of up to 816 F/g [105] and SSA of up to 1873 m²/g [142] are achieved. The type of used electrolyte is a key parameter for the determined capacities. The capacity for an aqueous electrolyte at 45 F/g and for an organic electrolyte can be significantly lower (10 F/g) [124]. The capacity C of the 3D carbon structures is calculated via equation (2.9) [37,128].

$$C = \frac{I \cdot \Delta t}{m \cdot \Delta V} \qquad (2.4)$$

With, the loaded current I in A, the discharge time Δt in s, the mass of active material m in mg and the potential change during the discharge process ΔV. The capacity and performance of the EDLC dependence on the pore design and, on the specific surfaces area. *Wang et al.* showed that structures with the same pore properties but different designs (2D or 3D pores) influence the capacitive properties of the electrodes [143]. In addition, in another study, the linear dependence of the capacity on the achieved SSA was observed [144].

Table 2.2: Overview of properties of 3D carbon-based supercapacitors.

Material	SSA in m²/g	Density in mg/cm³	Capacitance in F/g	Reference
Graphene aerogel	-	-	366	[30]
Graphene aerogel	512	12-96	128	[31]
Aerographite	-	1-14 [35]	640	[37]
3D NiO/Graphene Networks	-	-	< 816	[105]
ZnO nanorods and graphene foam	214.5	-	400	[111]
Carbon aerogels	400-800	800-1000	10-45	[124]
Graphene/ Polypyrrole Nanotube	-	-	253	[128]
3D graphene-pyrrole/carbon nanotubes/polyaniline	-	-	400	[133]
Nanocellulose-carbon aerogel	418-1873	-	72-302	[142]
Elastic Carbon Aerogel	57.8	4.8-5.9	180	[145]

Nitrogen-containing cotton derived 3D porous carbon frameworks	285	-	200-308	[146]
3D hierarchical porous carbon	823-1224		165-175	[147]

Besides, to the application of 3D carbon structures for energy storage systems, these materials can also serve as the basis for catalysts. The importance of catalysts with a global demand worth US of $33.5 billion for the economy is summarised in a market study from 2014 [148].

In order to be able to use carbon aerogels for catalytic applications, catalytically active materials such as metals or metal oxides must be added to the carbon structure. For sol-gel-based carbon aerogels, a distinction can be drawn between 3 different manufacturing methods for catalytic aerogels after *Moreno-Castilla et al.* as shown in Table 2.3 [135].

The first method for the production of aerogels, catalytically active additives can be added to a mixture of formaldehyde and resorcinol, followed by a supercritical drying [136,137]. In the second method, the gels as described by *Pekala* [101] are produced and supplemented by catalytic additives. This is followed by a carbonization of the metal-loaded organic aerogels at high temperatures in a nitrogen atmosphere [139].

In the third method, catalytic metals are applied to the organic aerogel by adsorption, sublimation and supercritical deposition [135,138,140].

24

Table 2.3: Overview of synthesis methods for carbon foam-based catalysts.

	Dissolving in initial mixture	Polymerisation of resorcinol derivative	Deposition of metal precursor
SSA in m²/g	500-2240 / 1-176	689 -712	483-655 / 629-889
Catalysts	Ce, Zr / Cr, Fe, Co, Ni	Cu	Pt / Pt
References	[136] / [137]	[139]	[138] / [140]

2.2 Fundamentals of the chemical vapour deposition (CVD) - thermodynamic and mechanisms-

For the production of thin films different sub-types of the CVD process are available. In this case, the CVD method is used with regard to its temperature heating methods: Plasma enhanced CVD (PECVD) and thermal CVD, which can be distinguished in a hot-wall and a cold-wall CVD. Furthermore, the CVD process can be classified by the applied system pressures [149]. In the hot-wall CVD process, the reactor is heated by means of resistance heaters, so that the complete reactor chamber is heated. Here the deposition of the injected material takes place both on the template and on the reactor wall. In the case of the cold-wall CVD reactor, only the substrate is heated to the required temperature and the deposition of precursors occur just on the substrate [149].

The growth of thin film during thermal CVD processes are based on the nucleation of atoms from the vapour phase on a template surface [149–153]. The formation of the films is following fundamental key steps [149,151–153], as visualised in Figure 2.6.
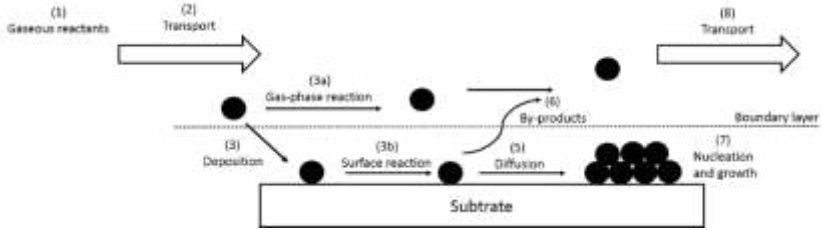
(1)   Formation of gaseous reactants

(2)   Transport into the reactor

(3)   Deposition on the template surface

      a.   Homogeneous gas phase reaction

      b.   Heterogeneous reaction

(4)   Deposition of reactants on the template surface

(5)   Surface diffusion and formation of centers and films

(6)   Remove of gaseous by-products

(7)   Nucleation and growth of the reactants

(8)   Unreacted precursors and by-products are transported out of the reactor

Figure 2.6: Schematic model of the CVD process after [149,151–153].

Due to different diffusion processes, but also by the flow-induced formation of the boundary layer to the substrate, the CVD process is dependent on the slowest partial step of the reaction with respect to the reaction rate [149,151].

The temperature in the preheating zone is lower than in the main zone where the chemical reactions and transformation processes take place. Equation

(2.10) describes a general characterisation of reaction steps in a CVD process after *Rashid et al*. The reaction educts are supplied to the CVD process as solids or as liquid specimen $AB_{2\ (solid\ or\ liquid)}$, whereupon these pass into the gas phase $AB_{2\ (gas)}$ and finally deposit on the substrate $A_{(solid)}$, releasing a gas $B_{2\ (gas)}$ [154].

$$AB_{2\ (solid\ or\ liquid)} \ \rightarrow \ AB_{2\ (gas)} \rightarrow A_{(solid)} + \ B_{2\ (gas)} \qquad (2.5)$$
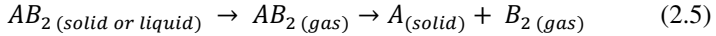
The growth of layers can be divided into three main mechanisms. The nature of the resulting mechanism depends on a combination of surface defects, diffusion, thermodynamics and growth kinetics [155]. The *Frank-van-der-Merwe* growth, which is also referred to as layer growth, proceeds from the single-layered growth of individual layers. The adhesion between the layer and the template surface is approximately the same [156–158]. In the case of *Stranski-Krastanow* growth, the higher adhesion of the first monolayer compared to the substrate surface leads to island growth on the layer [159]. In the case of *Volmer-Weber* growth, which is also referred to as island growth, the adhesion on the new layer is much higher than on the substrate surface, and the formation of islands from the precursor material follows [160]. In addition, the epitaxial growth of the precursor on the substrate can be distinguished in a homo- and heteroepitaxial growth behaviour. Homoepitaxy is the growth of the same material as the substrate. Whereas heteroepitaxy is the growth of a substrate-different material [149,152,161].

The layer growth in the CVD process dependents on the thermal flow behaviour (including the characteristic gas properties), the pressure in the reactor and the reactor geometry has an additional influence on this system [152,161]. The Gibbs free energy (ΔG_r^0) is a key parameter for the description of a CVD process and of possible reactions. Gibbs free energy is composed

of the sum of the individual energies of the products $\sum \Delta G_f^0$ (*products*) and the educts $\sum \Delta G_f^0$ (*reactants*) [149] as described in equation 2.6. In this case, a preference is given to reactions with a negative Gibbs free energy [149,152].

$$\Delta G_r^0 = \sum \Delta G_f^0 \; (products) \; - \; \sum \Delta G_f^0 \; (reactants) \qquad (2.6)$$

The deposition of atoms on the template surface and their clustering to a film dependent on the released Gibbs free energy. Optimal binding forces exist in energetically favourable points such as edges or terraces, as shown in Figure 2.7. *Salanon et al.* described that surface defects such as steps or kinks have lower energies than a defect-free surface [162]. As a result, after the surface diffusion of reactants (I-II), the layer formation starts at energy preferably points such as defects by reduction of the Gibbs free energy (III), as shown in Figure 2.79 [163].
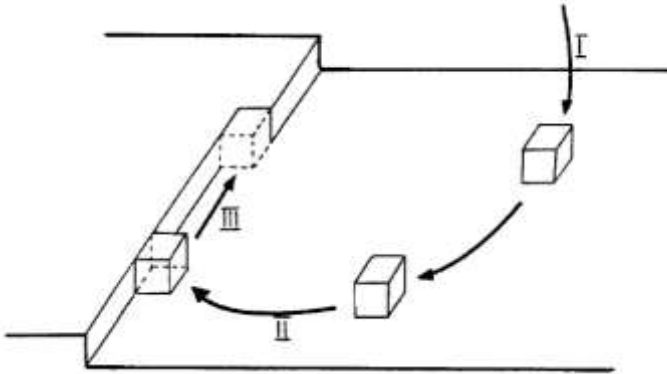

Figure 2.7: Scheme of the incorporation of atoms in energetically favourable sites [159].

2.3   Modification of physical properties (thermal treatment)

The growth process of carbon structures leads to defects in the arrangement of the atoms, which are not considered to be the final stage. By annealing of carbon structures, e.g. CNTs, these lattice defects can be reduced or even eliminated as TEM images of several observations have shown a higher lattice orientation [41–44]. Additionally, to TEM observations, Raman spectra have shown a significant decrease of the D-band and simultaneously an increase of the G-band as presented in Figure 2.8a. Which results in a continuously decrease of the I_D/I_G ratio, or defect density called, with increasing treatment temperature. *Zhao et al.* showed that a treatment temperature above a critical temperature of 2800 °C leads to a formation of graphitisation introduced defects and in the following an increase of the defect density [44]. Consequently, Raman spectra confirms the structural orientation of carbon atoms and is an effective method to analyse the influence of thermal annealing on the formation of graphitic layers. The thermal annealing results in the formation of the D´-band at ~1620 cm^{-1}, by splitting of the G-band, which is not finally clarified [41–44]. The reduction of defects in the carbon lattices results in an improved oxidation resistance up to 13 %, as shown in Figure 2.8b [44]. Finally, by thermal graphitisation the structural improvements in carbon structures leads to a decrease of the electrical resistivity or corresponding in an increase of the electrical conductivity [44], as shown in Figure 2.8c.
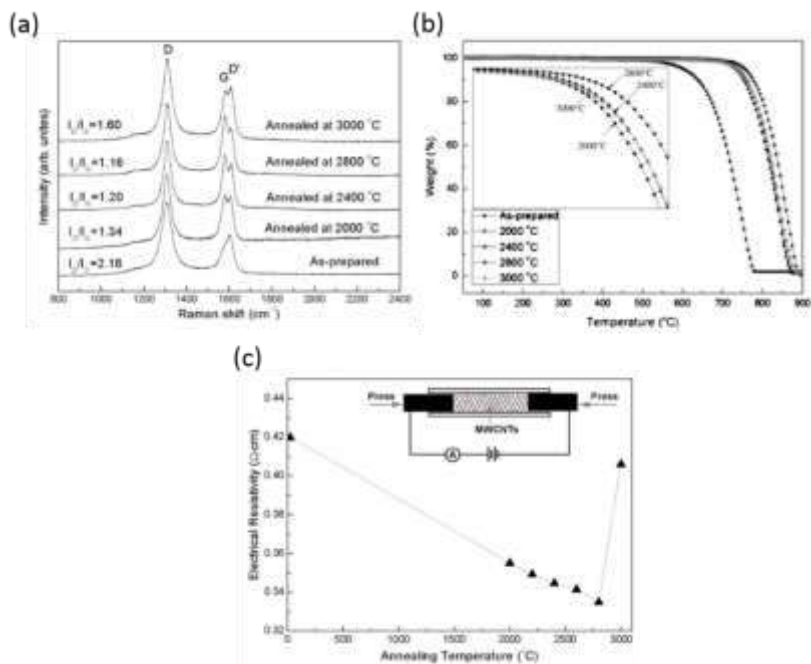
Figure 2.8: Effect of thermal annealing on the formation of Raman spectra (a), decomposition temperature (b) and electrical resistivity of MWCNTs (c) [44].

3   Experimental procedure

This chapter focuses on the used materials for the synthesis of the different carbon structures, the post thermal treatment of Aerographite, manufacturing of Aerographite-PNCs and testing methods for the analysis of physical properties and morphologies.

3.1   Materials and Process

The synthesis of the here presented 3D carbon structures are based on a two-step process. After manufacturing of the ceramic templates [164,165], the replication into the hollow carbon foam in the CVD process was carried out [28]. In the CVD process, a mimicry of the template morphology with a hollow carbon shell occurs, by the simultaneous removal of ZnO caused by the injected hydrogen [131]. Different initial materials are required for both carbon variants.

3.1.1   Materials for the synthesis of the tetrapodal Aerographite template

The synthesis of Aerographite is based on a ZnO template with a tetrapodal morphology as presented in Figure 3.1. The required ZnO template was synthesised in the flame transport synthesis (FTS) [164], by our project partner "Christian-Albrecht-Universität zu Kiel (CAU Kiel)" by Ms. D. Smazna and Ms. M. Mintken. For the manufacturing of this tetrapodal morphology, Zn nanoparticles and Polyvinylbutyral (PVB) were mixed in a ratio of 1:2 (weight ratio) and filled in a ceramic crucible. This mixture was heated up in a muffle oven at 900 °C for 30 min. Due to this process step nano-micro structured blocks were formed, in order to obtain a tetrapodal

network. For a subsequently sintering process, the ZnO powder was pressed into required geometries and heated to 1150 °C for 5 h [164]. All produced ZnO templates regardless of their geometry have a density of 0.3 g/cm³. The synthesised template exhibits directly connected sintering necks (1) but also a high proportion of dead ends (2). These dead ends remain after replication into a hollow carbon structure and do not contribute to electrical conductivity. Whereas the connected tetrapods and their portion are significantly for the electrical conductivity by forming electrical pathways.
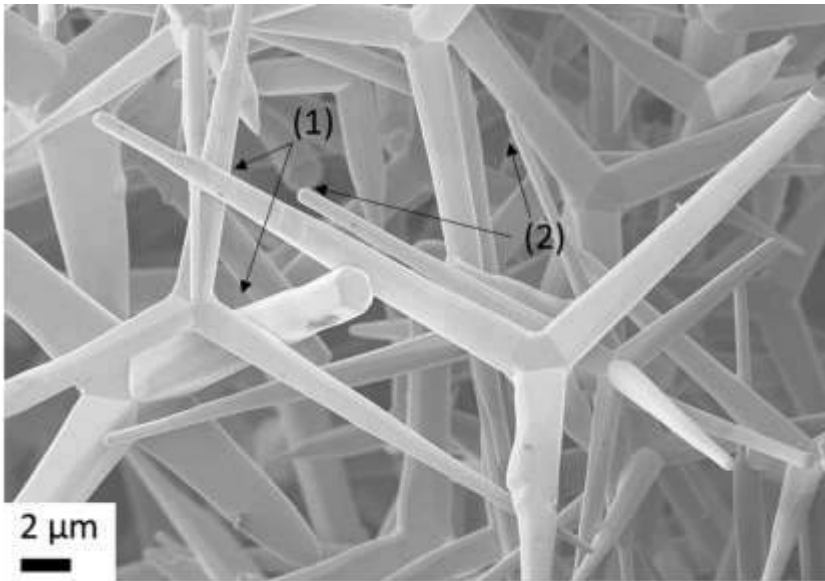

Figure 3.1: Tetrapodal morphology of used ZnO template for Aerographite.

3.1.2 Materials and process development for the manufacturing of a hierarchical porous ceramic template

The template for the synthesis of a 3D hierarchical structure with a globular morphology (Globugraphite) is based on a simple sintering process [165]. For the manufacturing of these structures, a ZnO micro powder (ReagentPlus®, 5.61 g/cm³, 99.9 %) from Sigma-Aldrich® with a mean particle size of <5 µm was used and a ZnO nano powder with a particle size of smaller than 100 nm was used. For the preparation of green bodies, PVB powder (Mowital® B 60 HH, Kuraray®) with a purity of 97.5 % and a bulk density of 1.1 g/cm³ was used.

These templates were produced in a four-step process. First, the green bodies were produced by mixing ZnO powder and the added PVB powder. This mixture contains a volume fraction of 45 vol.% of PVB.

To achieve a homogeneous mixture of ZnO with PVB, the powders were mixed for 1 hour at a rotational speed of 645 min^{-1} in an attritor with distilled water and ceramic balls with a diameter of 3 mm. After mixing, the compound was dried in a rotary evaporator, milled and sieved with a mesh size of 200 µm. In the next step, the ZnO/PVB compounds were shaped in a uniaxial press P/O/WEBER® WHC 10 with a tool diameter of 14 mm at a maximum force of 10 kN in air atmosphere. The maximum force was held for 30 s, to ensure a sufficient cohesion of the green body while at the same time a high porosity remains. The resulting sample dimensions were 14 mm in diameter and 1.6 mm in height.

Finally, the samples were sintered in a sintering furnace in Al_2O_3 cups. To determine the optimum sintering temperature for the formation of sinter necks and a still highly porous structure TGA (TA instruments Q900 TGA) and dilatometry (NETZSCH DIL 402 PC) were used to measure the

evaporation temperatures of the PVB and the shrinkage of the sintered body, as shown in Figure 3.2.

Figure 3.2a shows the volume shrinkage in the dilatometry measurement. The sample was heated with a heating rate of 2 K/min up to 800 °C and the change in length Δl is measured, after determining the initial length l_0 of the sample. Equation (3.1) shows the calculation of the longitudinal shrinkage S_L. Assuming an isotropic shrinkage, the volume shrinkage S_V can be calculated using the equation (3.2).

$$S_L = \frac{\Delta l}{l_0} \tag{3.1}$$

$$S_V = 1 - (1 - S_L)^3 \tag{3.2}$$

Above 225 °C, the shrinkage of the green body is about 1-2 % and constant up to a temperature of 500 °C. A shrinkage of maximum 5 % is required to form only sintering necks [167]. Above 500 °C the shrinkage significantly increases followed by a complete sintering of the green body which leads to a low porous structure [25]. The measurement of the volume shrinkage was completed measuring the oxidation temperature of the filler from the TGA to determine the sintering temperature. The filler is completely decomposed at a temperature of 420 °C as shown by the TGA measurement in Figure 3.2b. Only 1 % of the polymer remains at a temperature of 400 °C in the green body. According to these results, the sintering temperature was set at a temperature of 400 °C. The furnace was heated with a heating rate of 2 K/min in order to slowly approach the oxidation temperature of the PVB and to ensure the stability of the green body. Then the temperature was held for 30 min so that sinter necks can build but still no complete sintering to a pore-free body occurs. Subsequently, the sintered bodies were cooled with a

cooling rate of 2 K/min to stop the sintering process and to prevent crack formation due to residual stresses.
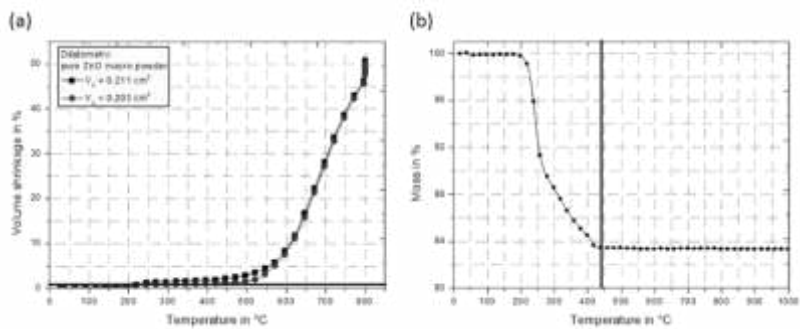
Figure 3.2: Determination of the sintering temperature of ZnO/PVB green bodies via dilatometry (a) and TGA (b).

3.2 Replica CVD process into a 3D carbon foam

The replication of the template morphology, tetrapodal for Aerographite and globular for Globugraphite, was carried out in two CVD reactors. The geometry and the specific flow rates are summarised in Table 3.1.

Table 3.1: Process parameters for the CVD process.

	Carbolite HZS 12/- /900 (a)	Nabertherm RS80/750/11 (b)
Diameter	108 mm	80 mm
Argon flow rate	0.2 l/min	0.15 l/min
Hydrogen flow rate	60 ml/min	45 ml/min
Standard injection rate of toluene	7.5 ml/h	6.5 ml/h
Range of applications	Wall thickness, Globugraphite	Growth mechanism, CFD simulation

The replication process of the template morphology in the CVD process started with the positioning of the samples on a silica wafer in a well-defined position for each reactor, compared to Figure 3.3a,b, for each reactor at position (3) in the main zone of the quartz tube of the reactor (2). The synthesis is basically based on a two-stage process (Figure 3.3c) which began with the heating of the reactor up to 760 °C, while adjusting an argon flow to fill the reactor with inert gas. The replication started in a 1st phase with the injection of the carbon source (toluene, C_7H_8, 99.5 % Alfa Aesar) for usually

60 minutes into the preheated zone (200 °C) of the reactor Figure 3.3a,b (1). For the simultaneous reduction of ZnO to gaseous Zn, hydrogen was supplied with a specific flow rate for each reactor. Here, toluene was evaporated and transported by the introduced gases into the reactor. The replication process was finished, while the reactor was heated up to 900 °C without injection of toluene. This 2nd reaction phase at 900 °C also takes 60 minutes. The synthesis ended with a cooling phase and an argon flow of 0.4 l/min for both reactors and without the supply of hydrogen.
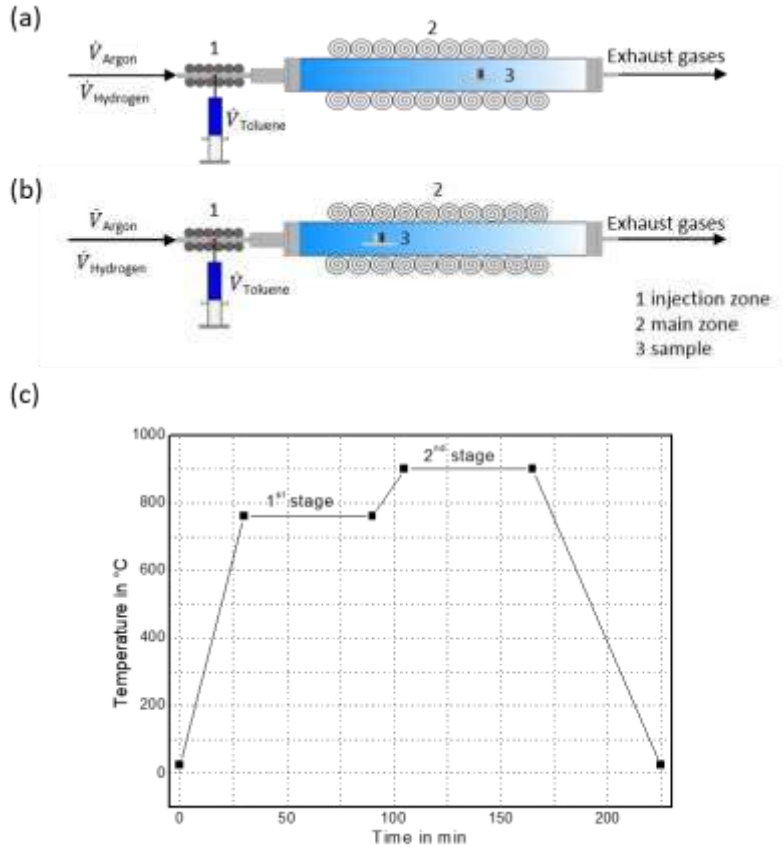
Figure 3.3: Scheme of the CVD process and of the first reactor (a), of the second reactor (b) and process curve of the CVD process (c).

The analysis of the growth mechanism of Aerographite was observed via regularly interrupted synthesis during the 1st phase. Based on these results a modified synthesis is developed to reduce the wall thickness of Aerographite. The injection time was reduced in the 1st phase at the same injection rate, whereby the total carbon amount is reduced.

39

3.3 Sample geometry

Because of the different morphologies and manufacturing methods different sample geometries were used to characterise the physical properties of carbon foams.

Based on the manufacturing of Globugraphite a tablet-like geometry was used for catalytic characterisations as shown in Figure 3.4. For the analysis of the respective properties of Aerographite, various geometries were used. The observation of the growth mechanism and the development of Aerographite with different wall thicknesses was carried out with a volume of 1 cm³. For the investigation of the dependency of the graphitisation and of the wall thickness on the electrical and mechanical properties of neat Aerographite and their composite a rectangular geometry was used. The corresponding samples for the analysis of the fracture toughness were cut into rods according to ASTM D5045. To investigate the graphitisation process, in dependency on the treatment temperature and holding time a cylindrical geometry according to the investigation of the growth mechanism, was used.
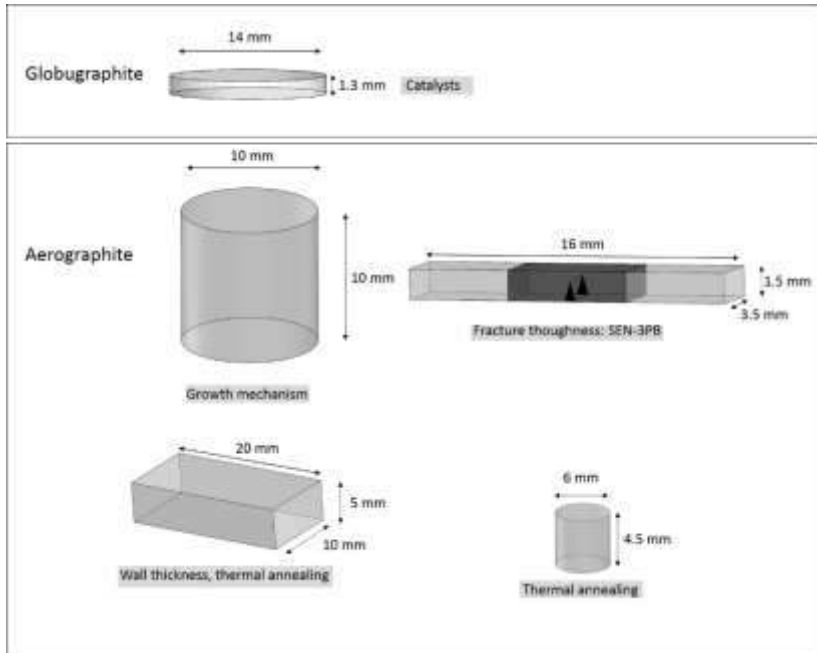
Figure 3.4: Sample geometries of Globugraphite and Aerographite for different analysis methods.

3.4 Manufacturing of Aerographite-epoxy composites

Aerographite-epoxy composites are produced in an already published vacuum-assisted infiltration process [34,35,48]. For the infiltration process an epoxy system (Hexion, RIMR 135/RIMH 137, Momentive) was mixed with a flexibilizer (Huntsman, Jeffamine D-4000). The resulting mixing ratio of 100:19.5:5.25 was set based on the amine ratio. After the infiltration, the samples are curved at 50 °C for 14 h followed by a stage at 80 °C for 6 h. The samples were cut into rods with a cross section of 1.5 mm x 3 mm (ASTM D5045) for the fracture toughness tests [168]. The specimens were pre-

cracked via a razor blade and a resulting ratio of specimen height to the crack length according to ASTM D5045 of 0.45-0.55 was achieved, before the mechanical tests start.

3.5 Thermal treatment of Aerographite

The graphitisation of Aerographite and Globugraphite was carried out in high-temperature furnaces (Gasdrucksinterofen, Dieckmann - TUHH and Gero HTK 8 - TU Ilmenau). The respective furnaces were evacuated several times before the actual annealing process and purged with argon. The thermal annealing was executed in an argon atmosphere at 1 bar. The furnace was heated to the respective temperature at about 20 K/min while maintaining the temperature for 2 h. The temperature was set at 1600 °C, 1800 °C, 2000 °C and 2200 °C, which is the maximum temperature of the furnace.

Additionally, to investigate the influence of the treatment time on the formation of carbon atoms and the healing of defects in carbon lattices the holding time during the thermal treatment was varied from 0, 30, 60 to 240 minutes, according to the previously used process curve, respectively.

3.6 Experimental set-up

3.6.1 Electron microscopic analysis (SEM, TEM/EELS)

The morphology and the wall thickness of Aerographite and Globugraphite was analysed via scanning electron (SEM) and transmission electron microscopy (TEM).

The morphology of Aerographite and Globugraphite as well as the chemical composition were analysed using a SEM (Zeiss Supra VP 55, acceleration voltage 5 kV-10 kV) in combination with energy dispersive X-ray spectroscopy (EDX). The samples were fixed on a sample holder with a

graphite glue and silver lacquer. Because of the low density (~3 g/cm³) of Aerographite, the samples were extra fixed in aluminum foil.

Additionally, to the SEM observations the sub-micrometer structure of Aerographite and Globugraphite is measured via TEM and scanning transmission electron microscopy (STEM). Therefore, a TEM, Talos F200X made by FEI with an acceleration voltage of 200 kV was used. The TEM samples were prepared by dispersing the carbon structures in methanol (LC-MS >99.9 %, Sigma Aldrich) via an ultrasonic sonotrode (Bandelin Sonoplus) for 10 seconds with a power of 10 %. Hereby, the macroscopically connected particles are singled out. Consequently, a sub nanometer sample size is reached for the analysis in the TEM. Finally, the solution was dropped on a TEM grid and dried for 45 minutes at 80 °C on a heating plate.

The determination of the sp^2/sp^3 ratio was executed using electron energy loss spectroscopy (EELS). The measurements are done by Mr. J. Strobel (CAU Kiel) using a Tecnai G2 F30 STwin, 300 kV with an integrated EELS spectrometer (GIF Tridiem 863). The background was corrected with a multiple-scattering method. The sp^2/sp^3 content was calculated based on the calculation method by *Urbonaite et al.* [169] using graphite [170] as reference. However, in contrast to the used intensity maxima the area beneath the typical peaks was used for the determination of the measured amounts.

3.6.2 Electrical studies

The electrical resistance of Aerographite with a cylindrical and Globugraphite with a tablet-like geometry was measured using a 4-wire configuration as shown in Figure 3.5 with a defined current at the source

meter of 1 mA (Keithley 2602 System SourceMeter) and a measuring frequency of 50 Hz at room temperature (25 °C) [34,35].
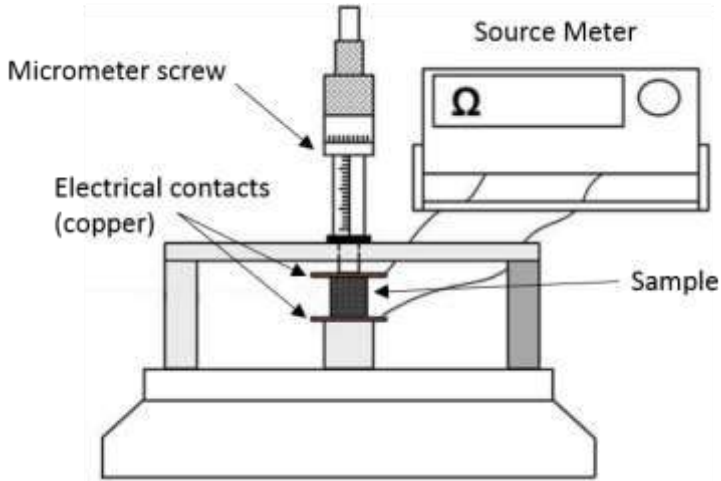
Figure 3.5: Schematic set-up for 4-wire configuration measurement of the electrical conductivity.

The electrical conductivity of Aerographite can be calculated on the basis of cellular materials [171,172]. However, as previously reported Aerographite can be understood more as a random network of conductive pathways [35]. The average electrical conductivity of Aerographite is also dependent on the sample density. By simplifying the relationship of cellular materials, a linear correlation between the electrical conductivity σ, the density ρ and a pre-factor C (0.1-0.8) arises [35,173]:

$$\sigma_{ave} = C \cdot \sigma \cdot \rho \tag{3.3}$$

Practically the electrical conductivity of Aerographite σ_{tot} was calculated as described in equation (3.4) by measuring the total resistance (R_{tot}), the sample

surface at the electrical contacts (*A*) and the distance between the electrical contacts (*h*), which correspond with the sample height as described before [34]. Whereby the distance between the contacts was set once before the start of the measurement and is not changed during the measurements.

$$\sigma_{tot} = \frac{h}{R_{tot} \cdot A} \qquad (3.4)$$

To determine the temperature-dependent electrical conductivity, the samples were heated in 25 °C steps up to 150 °C, with the respective temperature being held for at least 10 minutes before each measurement.

3.6.3   Raman spectroscopy

The analysis of the defect density and the graphitisation progress was executed via Raman spectroscopy (HORIBA Jobin Yvon HR 800) with a He-Ne laser at a wavelength of 632 nm. The Raman spectra were obtained at room temperature (25 °C) with a spectral width of 500-3000 cm^{-1}, an acquisition time of 10 seconds and a set filter of 0.6 at several positions on the sample surface. For evaluating the Raman spectra, in particular the D/G band ratio, the maxima of the individual peaks were correlated with each other. The respective peaks maxima are determined using a Lorentz fit. All samples were measured without any further preparation methods.

3.6.4   X-ray diffraction (XRD) studies

XRD studies were achieved by Mr. R. Behn (TUHH; Institute of Materials Physics and technology) with a Bruker AXS D8 Advance at an applied Cu

K_α source (1.5418 Å) between 15° and 70° and by Mr. J. Strobel (CAU Kiel) using a Seifert XRD 3000TT (Cu K_α source: 1.5418 Å) at 40 kV (20° - 80°).

3.6.5 Brunauer-Emmett-Teller (BET) method

The specific surface area (SSA) was analysed at the Institute of Materials Physics and Technology (Mr. M. Busch, TUHH) using the AUTOSORB® iQ, Quantachrome Instruments®. The SSA was calculated using the quenched solid density functional theory (QSDFT). The measurement error in this method was between 1 % and 5 %. This method is based on the consideration of inhomogeneities and surface roughness and is compared to the non-local density functional theory (NLDFT) suitable for carbon structures [174].

3.6.6 Mechanical studies of Aerographite-epoxy composites

The determination of the fracture toughness of Aerographite composites was performed in a SEN-3PB set-up with a single notch after ASTM D5045. The specimens were pre-cracked with a razor blade. Here, a ratio of specimen height to crack length according to ASTM D5045 of 0.45-0.55 was reached. A Zwick Roell 2.5 Universal testing machine in three-point end notch bending (SEN-3PB) test set-up was used. The distance between the supporting rollers was set at ~12 mm. The experiments were carried out with a crosshead speed of 10 mm/min. The notch depth was measured via microscopical methods (SEM). The determination of the fracture toughness is based on equation (3.5) after Ref. [175]. Here, filler contents between 0.32 wt.% and 0.49 wt.% were achieved.

$$K_{IC} = \frac{F \cdot L}{B \cdot w^{3/2}} \cdot f\left(\frac{a}{w}\right) \tag{3.5}$$

$$f\left(\frac{a}{w}\right) = 3\left(\frac{a}{w}\right)^{1/2} \left\{ \frac{\left[1.99 - \frac{a}{w}(1 - \frac{a}{w}) \cdot (2.15 - 3.93\frac{a}{w} + 2.7\frac{a^2}{w})\right]}{2(1 + 2\frac{a}{w}) \cdot (1 - \frac{a}{w})^{3/2}} \right\} \tag{3.6}$$

Where:

F - Maximum force

L - Span length

B - Width of the specimen

a - Crack length

w - Sample height

3.6.7 Thermogravimetric analysis (TGA)

The oxidation temperature of the presented carbon foams (Aerographite and Globugraphite) and PVB for the determination of the sintering temperature was investigated using the thermogravimetric analysis (TGA, TA instruments Q900 TGA). The samples were heated up to 900 °C with a heating and cooling rate of 20 K/min in a synthetic air (20 vol.% oxygen) atmosphere.

3.6.8 CFD simulation

For the simulation of the CVD reactor using CFD methods, it is required to determine fundamental informations via experimental tests. In this subchapter the experimental set-up and key parameters for the CFD model are shown. The simulation of the CVD process for the manufacturing of a 3D carbon foam occurs in this work for the first time.

47

For the simulation of temperature and flow behaviour, and additionally the mass fraction of the injected gases, samples are placed as shown in Figure 3.6. The 1st row is consisting of 3 cylindrical specimens, whereas the 2nd row consists 2 specimens with an offset to the 1st row.
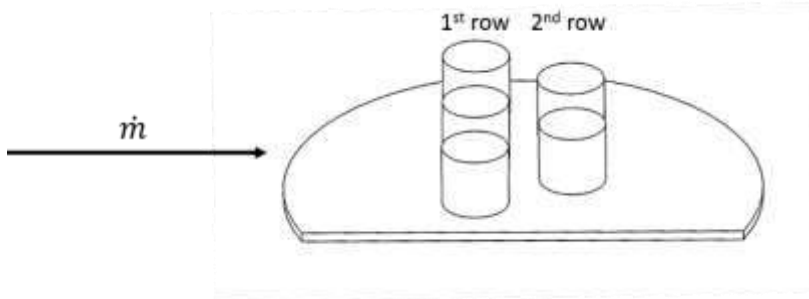
Figure 3.6: Sample position on a silicon waver for the CFD simulation.

The differential pressure is essential for the simulation of the porous ZnO template and the replicated carbon structure and was measured according to the schematic set-up, as shown in Figure 3.7a. Cylindrical ZnO specimens with a diameter of 10 mm and a height of 11.4 mm were fixed in a 3D printed polymer adaptor. The differential pressure was determined by a stepwise variation of the applied argon flow velocity, which was determined with a rotameter (ROTA L 6.3/250-7596) and plotted versus the flow velocity, as shown in Figure 3.7b. Based on this set-up a linear behaviour of the plotted graph is observed. This result will be used for the simulation of flow behaviour through the porous template structure. Several researchers published the influence of the porosity or of the pore volume on the pressure difference [176,177], but mostly for metal foams.
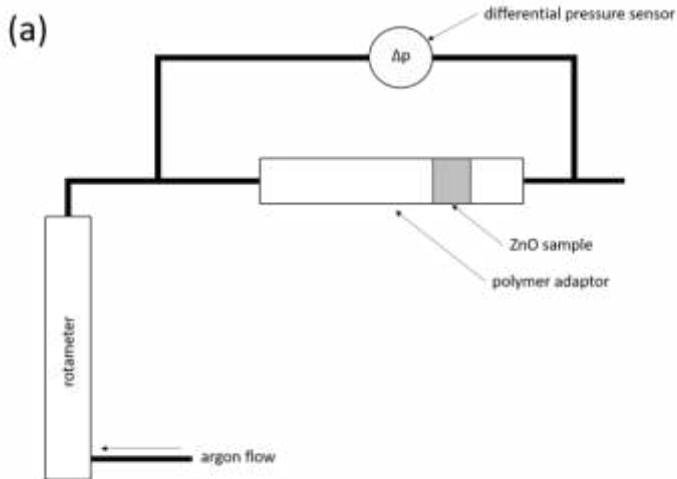
Figure 3.7: Scheme of the experimental set-up (a), measured differential pressure for ZnO (b).

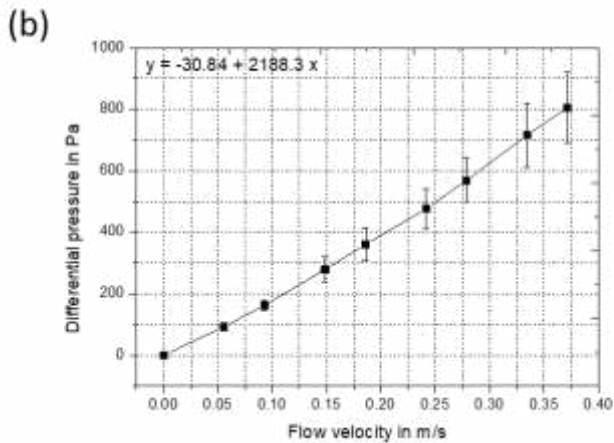The viscous resistance and inertial resistance were calculated using the coefficients of a polynomial 2nd grades, as shown in equation (3.7).

$$\Delta p = 1386.5 \ v^2 + 1620.5 \ v \qquad (3.7)$$

Afterwards, viscous resistance C_2 was calculated based on equation (3.8),

$$C_2 = \frac{2 \cdot 1386.5}{\rho \cdot t} = 170877.5 \ \frac{1}{m} \qquad (3.8)$$

and inertial resistance K was determined based on equation (3.9).

$$\frac{1}{K} = \frac{1620.5}{\mu \cdot t} = 7.63 \cdot 10^9 \ \frac{1}{m^2} \qquad (3.9)$$

Where:

v - Flow velocity in m/s

ρ - Density in g/cm³

μ - Viscosity of argon in Pa·s

t - Sample thickness in m

The numerical simulations were performed using the commercial code of ANSYS Fluent 18.0. The simulation was solved with a *SIMPLE* algorithm as already used by *Mostaghimi et al.* [178]. Additionally, the temperature dependency was solved with a *Surface to Surface* algorithm and the boundary conditions were set for the velocity at the reactor inside of 0 m/s (No Slip).

Table 3.2 is summarising key parameters of the CVD reactor and the applied replication process into the hollow carbon foam. The mass fraction was

calculated based on the used specific flow rates. The injected gases exhibit a temperature of 346 K, which is caused by a preheater in the injection and an inlet velocity of 0.17 m/s. The calculated Mach number *Ma* of 0.0004 which is $\ll 1$ exhibit an incompressible flow behaviour. Due to a Reynolds number *Re* smaller than the critical Reynolds number $Re_{crit} = 2300$ for flows in pipes, a laminar flow can be assumed. Moreover, the flow shows for horizontal cylinder a laminar convection, based on the calculated Rayleigh number *Ra*, which is between $10^4 < Ra < 10^8$.

Table 3.2: Key parameters for the simulation of the CVD process.

	Nabertherm RS80/750/11		*Analytical values*
Diameter/Length	80 mm/1530 mm	Mach number (Ma)	0.0004
Argon flow rate	0.15 l/min	Reynolds number (Re)	50.72
Hydrogen flow rate	45 ml/min	Rayleigh number (Ra)	$2.68 \cdot 10^7$
Toluene injection rate	6.5 ml/h	Mass fraction (Ar)	0.73
		Mass fraction (Toluene)	0.25
		Mass fraction (H_2)	0.01
		Inlet velocity	v_E= 0.17 m/s

4 Results and Discussions

This chapter focuses on the results and their extensive discussions. The understanding of the growth mechanism allows to tailor the electrical and mechanical properties of Aerographite. Finally, the possible application of Globugraphite is shown and their fundamentals will be explained in detail.

4.1 Growth mechanism of Aerographite

The growth mechanism of Aerographite was analysed via interrupted synthesis after 15, 30, 45 and 60 minutes during the 1st phase followed by intense SEM observations (Figure 4.1), respectively. The synthesis starts with neat zinc oxide templates (Figure 4.1a) in different magnifications, with tetrapod arm lengths of >20 µm and a tetrapod arm diameter of about 2 µm.

Immediately after injection of the carbon source and hydrogen into the reactor, a layer of carbon deposits on the surface of the zinc oxide scaffolds without any observable reactions (Figure 4.1b). Followed by the injection of the reaction components and the deposition of carbon on the template surface, the decomposition of the template and its simultaneous replication into a hollow carbon shell take places. This replication process starts at the energetically favorable points of the template, the corner of the ZnO scaffolds at the tetrapods base and continues along the tetrapod to its tip (Figure 4.1c-e). Simultaneously to the carbon deposition, ZnO is removed.

The resulting by-products are transported to the reactor outlet by the applied gas stream (argon). In the subsequently 2nd reaction stage, the remaining ZnO is removed by its reduction. Finally, at the end of the 2nd reaction stage, this mimicry of the template morphology is completed and results in a hollow

carbon structure with the typical thin walled tetrapods of Aerographite, as shown in Figure 4.1f.

Furthermore, it should be noted, that the experiments of interrupted synthesis showed a beginning of the replication process at the specimen backside, with respect to the reactor inlet.
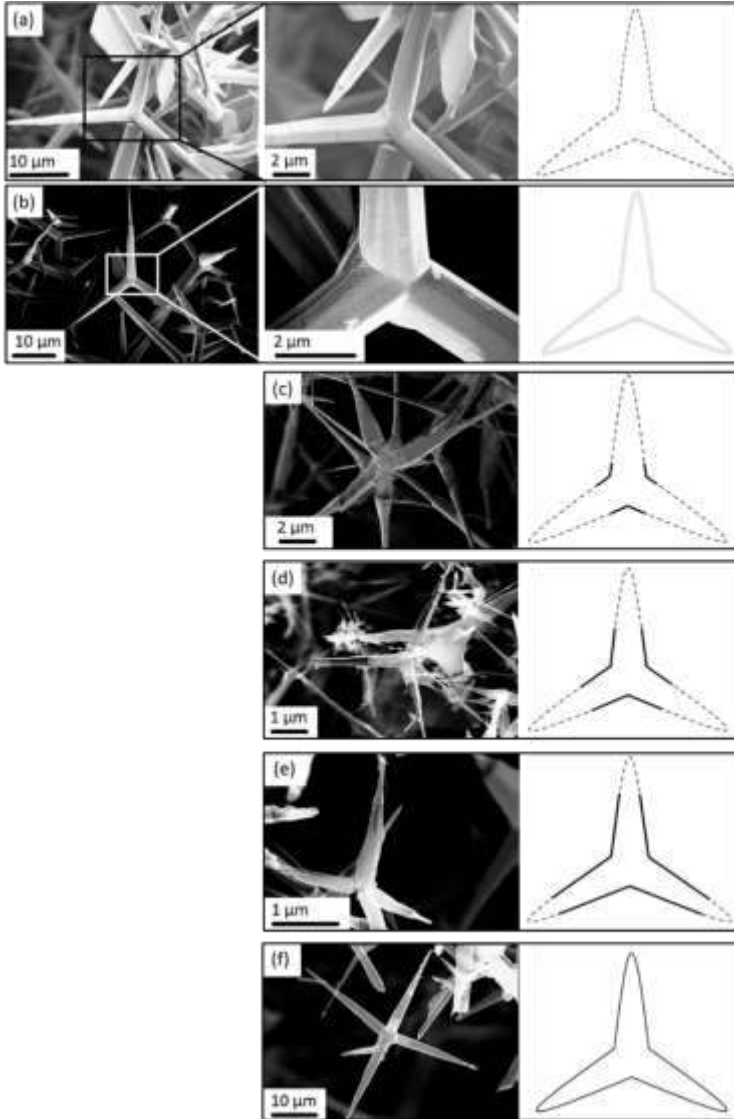
Figure 4.1: SEM images of zinc oxide template (a), interrupted synthesis during the 1st phase: 15 min (b), 30 min (c), 45 min (d), 60 min (e) and after the entire synthesis 135 min (f), the growth mechanism is shown schematically in the corresponding schemes.

However, due to a fast replication progress alongside of single tetrapod arms, ZnO agglomerates of several nanometres are incorporated into the newly formed carbon shell, as shown in Figure 4.2a. These ZnO nanoparticles still exhibits a crystalline lattice structure.

How these ZnO nanoparticles affect the physical properties, such as the electrical conductivity of Aerographite is unknown. Due to these incorporated particles, as shown in Figure 4.2b, the carbon lattice around ZnO is affected and exhibits a different structure. It can be assumed, that similar to the purification of CNT by various methods [179–181] an improvement in the physical properties of Aerographite will be observed.
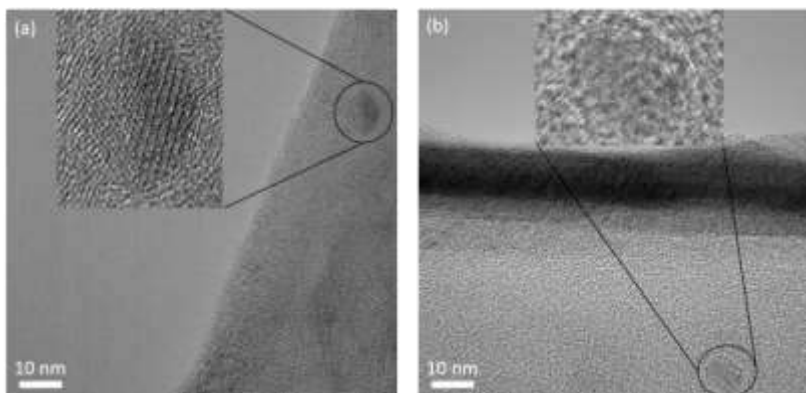
Figure 4.2: Incorporated ZnO nanoparticles (a)-(b), with a scale of ~10 nm in the insets.

Characteristic for the remaining hollow carbon structure is the nature of connection points between the single tetrapods, as already mentioned (Figure 4.3a). The manufacturing process of the ceramic ZnO template structure leads to individual connected tetrapod arms via sintering necks, which are also replicated in the process (Figure 4.3b), as mentioned already in chapter 3.1.1.

In addition, the morphology of Aerographite shows open ends of the single tetrapods, as already described by *Garlof et al.* for Aerographite-epoxy composites, which does not contribute to the electrical conductivity and can be referred to as "dead ends".As a consequence of this structural behaviour, the electrical resistance of Aerographite-epoxy composites $R_{composite}$ is consisting of the resistance of the single tetrapods R_t, resistance of a covalent bond between two tetrapods R_{cov}, the resistance between two tetrapods $R_{contact}$ and the tunneling resistance of two tetrapods R_{tunnel} [34]. However, this equation does not show any structural effects on the electrical conductivity of Aerographite.

$$\frac{1}{R_{composite}} = \sum_{n=1}^{N} \left(\frac{1}{R_{t,n}+R_{cov,n}+R_{contact,n}+R_{tunnel,n}} \right) \qquad (4.1)$$
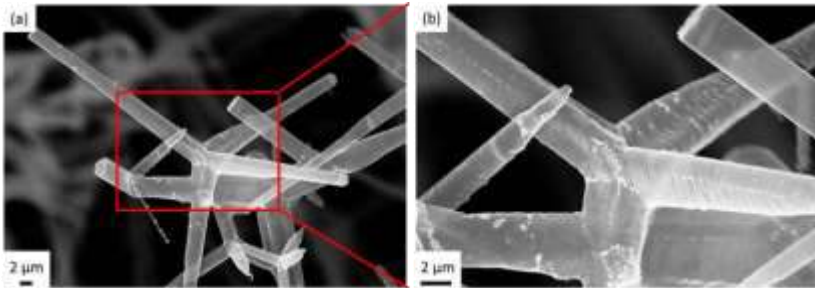
Figure 4.3: Characteristics of the morphology of Aerographite; sintering necks of single tetrapods (a), and its magnification (b).

TEM observations were used additionally to the SEM investigations, to analyse the replication process, as shown in Figure 4.4. The synthesised ZnO template, as given in the CVD process is free of any carbon on the surface (Figure 4.4a). By starting the CVD process, amorphous carbon deposit with a layer thickness of about 5 nm on the templates surface, covering the whole

tetrapod (Figure 4.4b). Without the reduction of ZnO to Zn, as shown Figure 4.4c, the deposited carbon is present as amorphous carbon. Only by the reduction of ZnO into gaseous zinc, amorphous carbon graphitises into short graphitic pieces, as shown in Figure 4.4d.

Consequently, a catalytically graphitisation of amorphous carbon with gaseous zinc as catalyst into graphitic carbon can be assumed. The basics of such catalytic transformations are already known for other metals such as Ti, Mn, Ni or Fe [182,183]. Furthermore, because of the homogeneous layer thickness of carbon on the template surface a layer-by-layer deposition of carbon can be assumed. This growth mechanism was first published by *Frank and van-der-Merwe* [156–158].
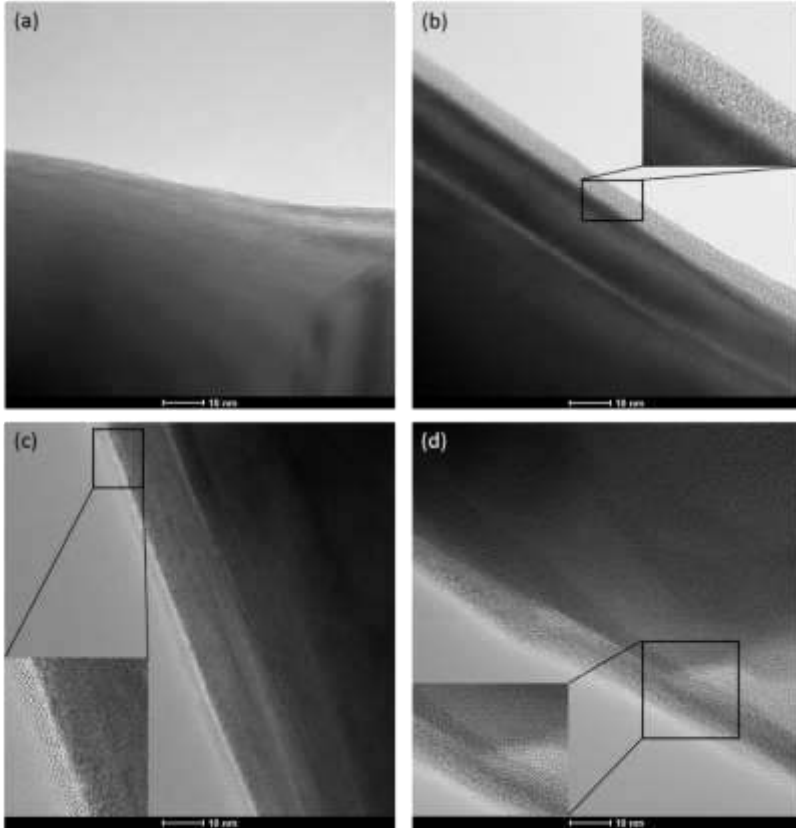
Figure 4.4: TEM image of zinc oxide tetrapod as received from FTS (a), interrupted synthesis during the 1st phase of the process: after 15 min (b), after 30 min (c), after 45 min (d), with a scale of ~15 nm in the insets.

Additionally, to the ex-situ electron microscopic analysis, Raman spectroscopy of the interrupted syntheses was used to understand the synthesis mechanism more detailed. The determination of the sample density and I_D/I_G ratio dependent on the reaction time, as shown in Figure 4.5a, provides additional information on the replication process. Immediately after

starting the synthesis, the carbon deposition leads to a reduction of the density, as well as a significant increase in the I_D/I_G ratio is observed. This indicates the reduction of ZnO to gaseous Zn and its diffusion through the formed carbon wall. The density decreases continuously over the entire replication process and reaches a minimum with beginning of the 2nd stage. Due to the 2nd reaction phase, which leads to the complete removal of the remaining ZnO, a significant increase in the I_D/I_G ratio is observed, which confirms the growth model in its assumptions.

The shortening of graphitic pieces by the diffusion of by-products over the synthesis time through the carbon wall can be determined calculating the crystalline width L_a based on Raman spectra, as shown in Figure 4.5b. *Knight and White* developed, based on the results of *Tuinstra and Koenig* [184], an empirical equation for the determination of the crystalline width of sp² lattices as shown in equation 4.2 [185]. The determination of the crystalline width L_a can be done in addition to Raman measurements by XRD techniques. *Vázquez-Santos et al.* showed a similarity of both techniques [94].

$$L_a = \frac{4.4}{I_D/I_G} \; in \; nm \tag{4.2}$$
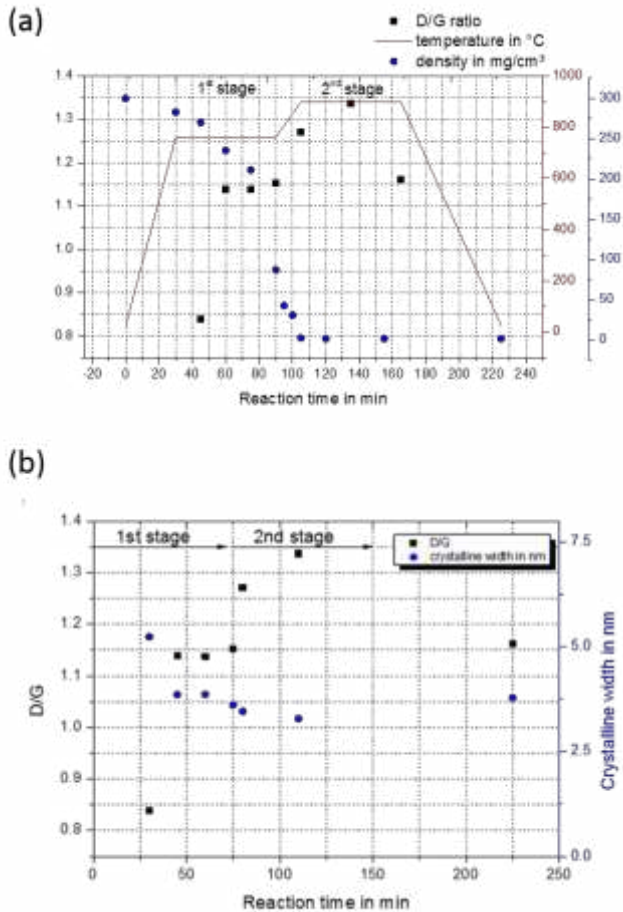
Figure 4.5: I_D/I_G ratio (black curve) and reaction stages (blue curve) over the synthesis time (a), comparison of I_D/I_G ratio with crystalline width (b).

Based on these observations a model of the occurred replication process was created. The replication of the template morphology is based on an epitaxial mechanism. This fundamental growth mechanism is the basis of any CVD process [153] also for the formation of carbon structures such as diamond films [186]. As the SEM observations have shown, this replication process

61

starts at the most energetically points for Aerographite. This confirms the observations and growth models of other carbon structures, e.g. graphene, which also starts at energetically most favourable locations in the CVD process [65,187]. The carbon deposition proceeds in several steps, as shown in Figure 4.6a.

For the deposition of carbon on the tetrapods of the ZnO template, the evaporation of the precursor in the pre-heated zone (200 °C) is of fundamental importance. The toluene splits into several C_nH_m groups and is transported by the gas stream of argon and hydrogen into the reactor (1). Subsequently, the reactants diffuse to the template surface (2) and finally deposit on the ZnO scaffolds (3). The reactants on the template surface can diffuse (4) by means of the temperature of 760 °C in the reactor, resulting in the reaction starting at the energetically most advantageous point, the tetrapod base (5) as to be seen in Figure 4.6b. The reaction takes place according to the following equation:

$$ZnO \text{ (s)} + H_2 \text{ (g)} + C_nH_m \text{ (g)} \rightarrow Zn \text{ (g)} + H_2O \text{ (g)} + H_x \text{ (g)} + C \text{ (s)} \quad (4.3)$$
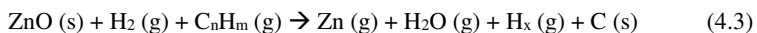
The diffusion of zinc trough the carbon wall (6) and its catalytically arrangement of amorphous carbon to graphitic pieces is shown in Figure 4.6c. This diffusion leads to the formation of discontinuously connected graphitic pieces and not to connected graphite layers. The reduction of ZnO to Zn is essential for the reaction taking place and has already been published several times [131,188,189]. Finally, Aerographite exhibits in contrast to graphene [64] or CNTs [84,85] its own growth mechanism, which is based on a catalytical graphitisation. However, similar to graphene, which grows preferably at grain boundaries [65], the replication process of Aerographite

62

starts also at such defects, such as the tetrapod base (Figure 4.1). Moreover, the deposition of carbon and the removal of ZnO can be described as bottom-up mechanism, which is analogue to CNTs [85].

(1) Transport of the reactants (H_2/C_nH_m)
(2) Gaseous diffusion of reactants to the surface
(3) Deposition of reactants on the surface
(4) Surface diffusion
(5) Start of the reaction
(6) Diffusion of ZnO to the surface; through the formed carbon wall
(7) Gaseous transport of by-products ($Zn, H_2O/H_x$)
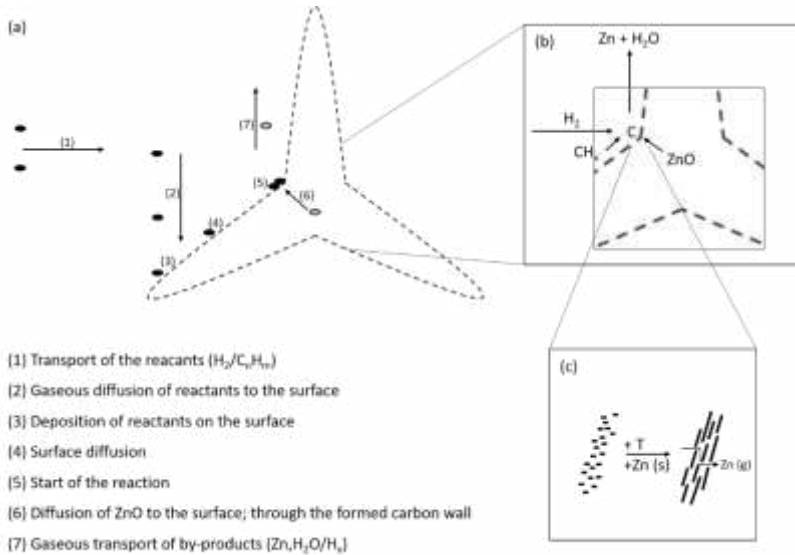
Figure 4.6: Schematic model of the deposition of carbon (a), diffusion of reactants/by-products (b) and the catalytic graphitisation (c) by the temperature T and the solid zinc catalyst - Zn (s) which reduce into gaseous zinc - Zn (g) due to the catalysis of amorphous carbon into graphitic carbon in the formed carbon shell.

Thermodynamic calculations and the experimental validation of the reduction of ZnO by gaseous hydrogen as shown in equation 4.4, shows for a reaction temperature of 760 °C and 900 °C a Gibbs free energy of approx. -68.83 kJ/mol and -48.04 kJ/mol [190]. The reduction of ZnO to Zn proceeds

endothermic, only the formation of the graphitic layers is thermodynamically not quantified yet.

$$ZnO\ (s) + H_2\ (g) \rightarrow Zn\ (g) + H_2O\ (g) \qquad (4.4)$$
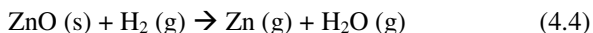
However, based on the CNT growth, the thermodynamic conditions for Aerographite can be estimated. By assuming that C_nH_m is equal to ethene (C_2H_4), analogue to equation 4.4 the Gibbs free energy for the deposition of carbon can be calculated. Resulting from the thermodynamic calculation a Gibbs free energy of -121.80 kJ/mol is estimated. However, if methane is produced instead of ethene (CH_4), as shown in equation 4.6, carbon would also deposit and form a carbon layer on the template surface because of a required Gibbs free energy of -23.22 kJ/mol.

$$C_2H_4(g) \rightarrow 2C\ (s) + 2H_2\ (g) \qquad (4.5)$$

$$CH_4(g) \rightarrow C\ (s) + 2H_2\ (g) \qquad (4.6)$$
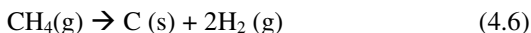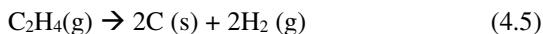
Thus, the replication process of Aerographite takes place with the submission of energy, with a total Gibbs free energy of approx. -190.63 kJ/mol for ethene or -145.02 kJ/mol for methane as the respective carbon source at 760 °C. With increasing n and m, a higher Gibbs free energy would be released, which leads to a preferential reaction of these educts.

Besides, to the ideal growth model of the replication of the ZnO into the carbon structure, defects such as contact points between the tetrapod arms and lattice defects, to be seen in Figure 4.7a, are the starting point of the replication process, respectively. The replication of ZnO into the carbon structure starts as well as on lattice or surface defects as shown in Figure 4.7b. These defects represent the energetically most favourable points of the tetrapods. Besides to defects, the ZnO reduction is carried out at contact points between two tetrapods as shown in Figure 4.7c,d.
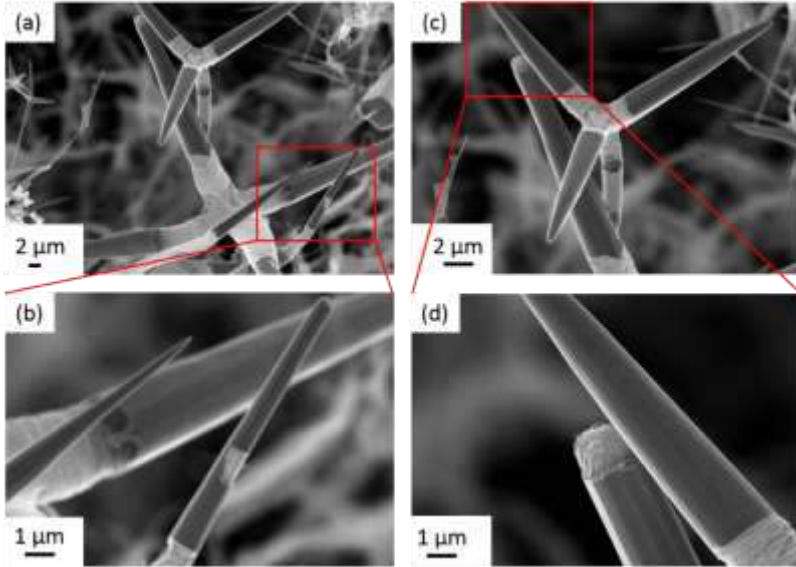
Figure 4.7: SEM image of defect introduced growth (a), start of replication at lattice defects (b), start of growth at contact point between tetrapods (c) and its insert (d).

Resulting of this growth model, the wall thickness of Aerographite can be tailored by variation of the injection time of toluene in the CVD process, as shown in Figure 4.8. The injection time of the carbon precursor in the 1st phase is varied between 5 minutes and 60 minutes. The injection phase is directly followed by the 2nd phase, in which the remaining ZnO is removed as described above.

At a regular supply time of 60 minutes of the carbon source, as shown in Figure 4.8a, a carbon wall of ~22 nm is formed, which is covered by few nanometers of amorphous carbon. The layer of amorphous carbon is formed by the absence of the zinc catalyst, which is necessary for catalytic

graphitisation. Reducing the injection time leads to a decrease of the wall thickness and the thickness of the added amorphous carbon layer, as shown in Figure 4.8b, which constantly continues down to an injection duration of about 30 minutes and a wall thickness of ~12 nm (Figure 4.8c). The further reduction of the injection time to 15 minutes, a formation of amorphous carbon layer is not occurred (Figure 4.8d). However, the shorter carbon supply reduces the wall thickness continuously down to ~3 nm (Figure 4.8 e,f). These TEM observations confirm the previously made assumption of the layer-by-layer growth of Aerographite according to the reported mechanism of *Frank and van der Merwe* [156–158]. A further injection of the carbon source on the already graphitised carbon layer of ~12 nm leads to a second layer of amorphous carbon, because of the diffusion barrier for the required zinc catalyst and the graphitisation process caused by the carbon layer. Furthermore, this amorphous carbon cannot be orientated into graphitic carbon by the temperature of the 2nd reaction stage or without zinc as catalyst.
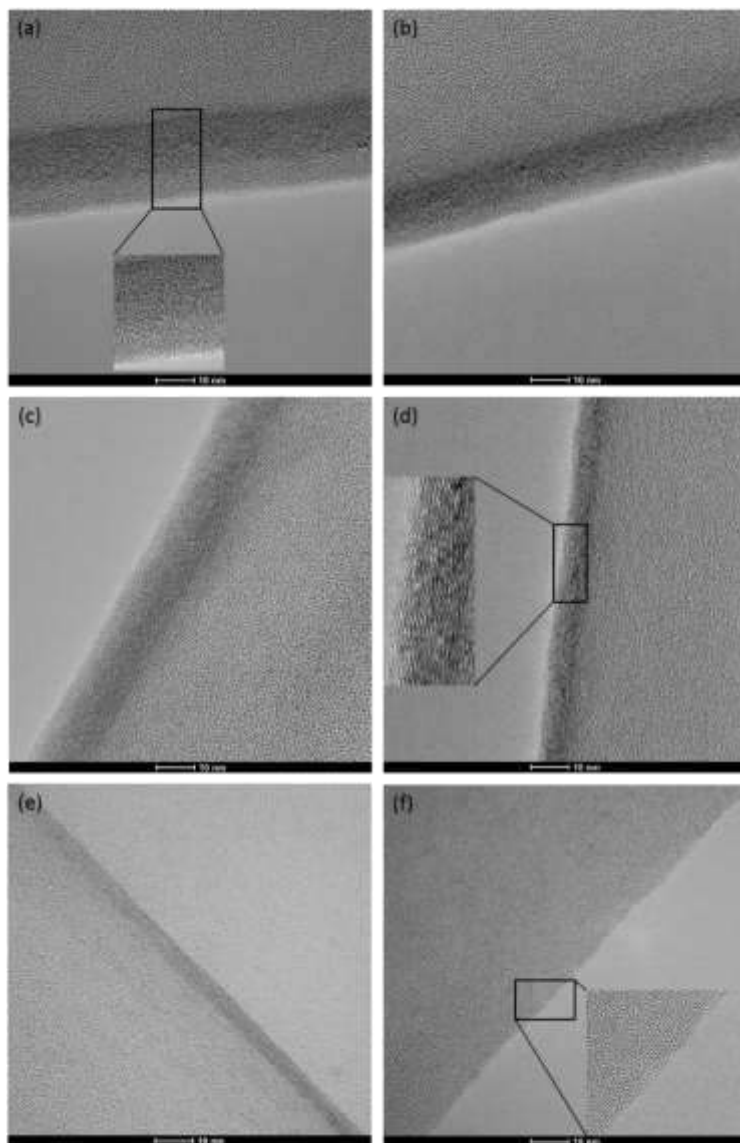
Figure 4.8: Dependence of the wall thickness on the injection time of the precursor (toluene) 60 min (a), 45 min (b), 30 min (c), 15 min (d), 10 min (e), 5 min (f), with a scale of ~10 nm in the insets.

TEM observations indicates a time dependent growth behaviour of the carbon deposition and graphitisation on the surface. By plotting the measured wall thicknesses versus the carbon injection time, as to be seen in Figure 4.9a, the growth of the wall thickness exhibits a linear behaviour. Due to the linear carbon deposition, the wall thickness of Aerographite increases continuously with 0.31 nm/min. This linear deposition behaviour of carbon on the template surface during the growth process of the carbon layer confirms the theory of the layer-by-layer growth by *Frank and van der Merwe* [156–158]. However, it should be mentioned, that at an injection time of 0 minutes a wall thickness of ~3.7-3.9 nm is calculated, which is practically impossible. This can be just observed for an injection rate >7.5 ml/h and is probably caused by a non-linear growth behaviour for an injection time < 10 minutes. The variation of the injection rate, by its reduction to 5.5 ml/h, also leads to a linear growth behaviour, whereas the carbon layer growth rate decreases from 0.31 nm/min to 0.21 nm/min, as shown in Figure 4.9b. On the other hand, with an increased injection rate up to 9.5 ml/h, the carbon deposition takes place with a growth rate of 0.37 nm/min.

Consequently, with an increased injection rate, the growth rate does not increase in the same range. A dependency of the growth rate on diffusion processes to the template can be assumed.
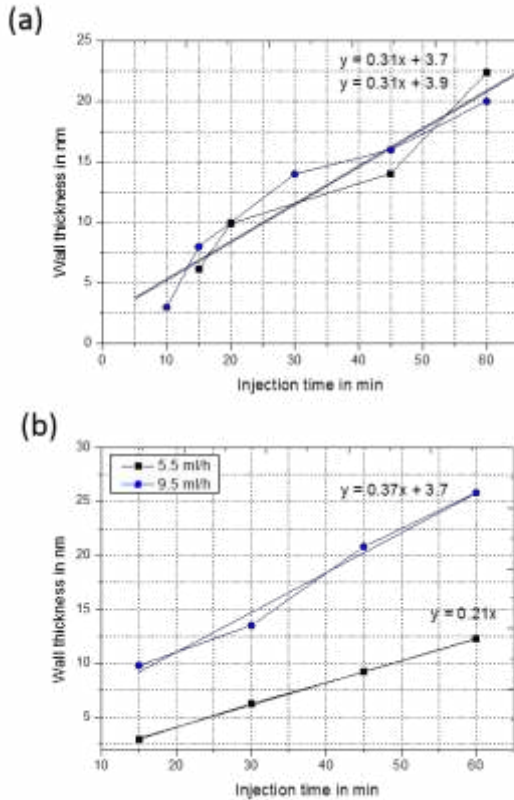
Figure 4.9: Dependency of carbon layer growth rate on the carbon injection time in the CVD process (black curve: results from chapter 4.2.2) (a), carbon layer growth dependent on the carbon injection time with a reduced injection rate of 5.5 ml/h (black curve) and 9.5 ml/h (blue curve) (b).

Besides to experimental observations of the occurred growth mechanism via ex-situ analysis of the growth behaviour, CFD simulation [191] (Figure 4.10) of such processes is an established method to clarify further questions such as the predominant temperature and flow behaviours in the CVD reactor. The

reactor cross-section in x-direction is divided into 4 sections (top-bottom), as can be seen in the scheme of the CVD reactor in Figure 4.10a. Figure 4.10b shows the temperature profile of the CVD reactor in the 1st reaction stage, in which important regions are marked (1)-(4). At the inlet (1), the gas mixture of argon, toluene and hydrogen are injected into the reactor with a temperature of 346 K and sinks immediately to the reactor bottom, due to the low temperature. The gas mixture flows to the reactor center (3) by passing the sample position (2) and is heated up, because of the applied temperature of 1033 K (760 °C). Due to this behaviour the gases are rising up to the reactor top and flowing back to the inlet. This results in partly surpasses of the positioned specimens, as shown in Figure 4.10c. Consequently, the replication process starts at the backside of the specimens, which confirms the observations of the interrupted synthesis as previously mentioned. After the heated fluid reaches the reactor inlet, it cools down at the reactor wall and sinks towards the bottom. This temperature behaviour is resulting in a circulated gas flow in the first half of the reactor. As a result, a division of the gases and a low gas exchange between the reactor halves occurs. By plotting the simulated temperature versus the reactor length in x-direction, as shown in Figure 4.10d and detailed in Figure A1 a significant temperature gradient of 150-200 K on the front side of the samples is observed (2). This is caused by the injected gases with a low temperature. Consequently, the front side is cooled down affecting the replication process. Furthermore, the temperature maxima in the CVD reactor in the middle of the reactor can be observed, which explains as already described the circulation of introduced gases (3). The simulated velocity in Figure 4.10e,f is according with the calculated values. The gases are injected with a velocity of 0.2 m/s into the inlet and their velocity is decreased by their expanse in the increased reactor volume down to 0.03 m/s. The velocity of the back flowed gases increases by heating

up of the injected gases. Furthermore, an increased velocity of the gases by flowing under the silica wafer was simulated whereas the velocity of the back flowed gases through the samples is reduced (Figure 4.10f). The specimens are defined as porous bodies. Regardless, the plotted velocity versus the reactor length (Figure 4.10g) shows a reduced velocity in the porous ZnO templates (2). Moreover, an increased velocity of the heated gases caused by the back flow and by passing the specimen position is observed.
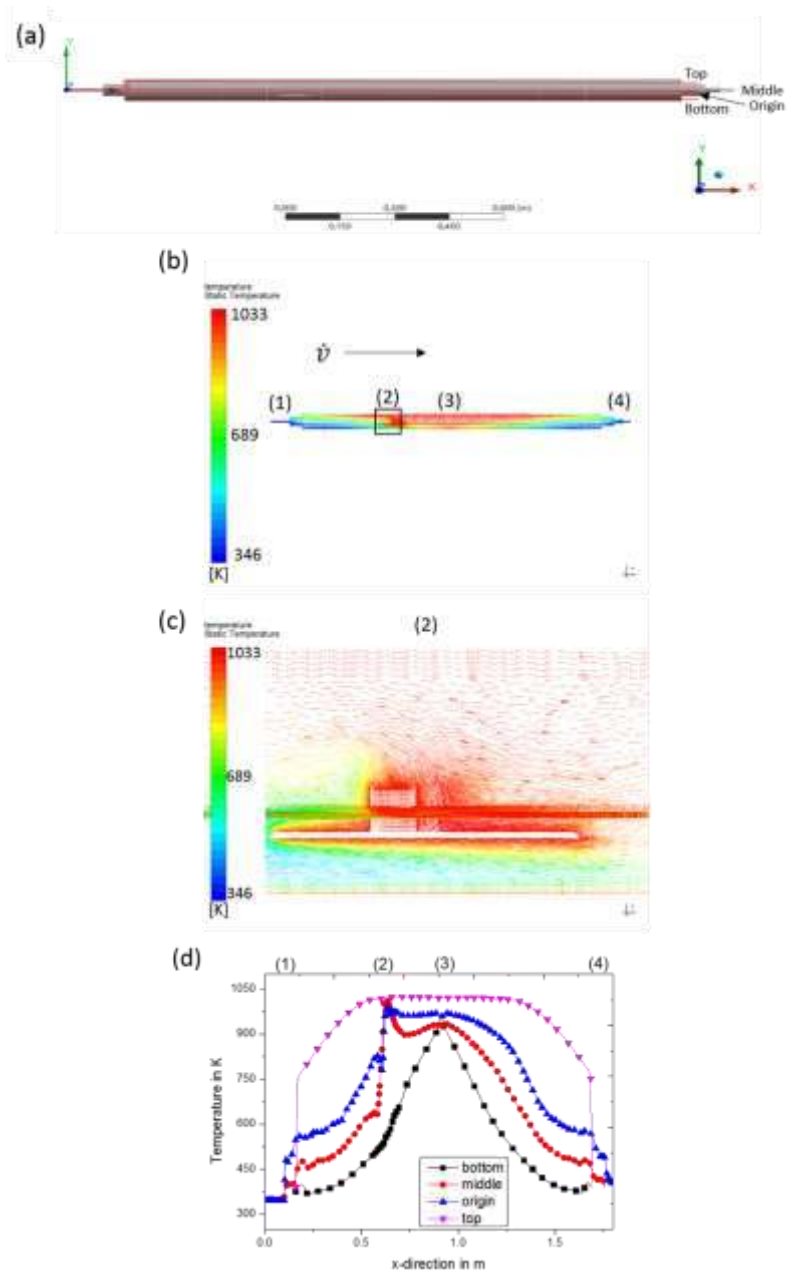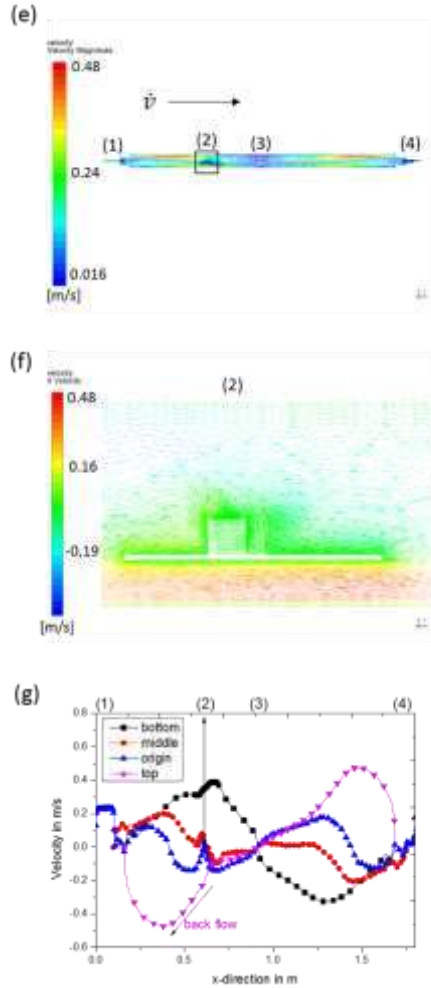
Figure 4.10: Scheme of the CVD reactor (a), simulation of global temperature (b), temperature in the sample area (c), plotted temperature (d), simulated velocity in the CVD reactor (e), local velocity in the sample area (f) and plotted velocity in x-direction (g).

The plotted toluene fraction versus the x-direction of the whole CVD reactor, as shown in Figure 4.11, reveals a rapid decrease from 25.6 % to 25.58 % after its injection into the reactor (1). Since the samples are defined as toluene sink in the simulation, their proportion drops to ~25.46 % (2). As described previously, the temperature barrier in the reactor middle (3) leads to a phase boundary, which is resulting in a toluene concentration gradient. The analysis of the toluene fraction on the silica waver at the sample height (Figure 4.11b - origin) exhibits the same toluene content in the 1st row (a) and 2nd row (b). However, the 2nd row exhibit a higher temperature, which affects the replication process, by its preferred starting point. The replication process starts in the 2nd row, which results from the temperature and flow behaviour as described in Figure 4.10 and Figure A2. The reduced temperature in the 1st row leads to a deformation of the specimens during the replication process by a rapid reduction of ZnO to gaseous Zn and an insufficient covering of the template by carbon.
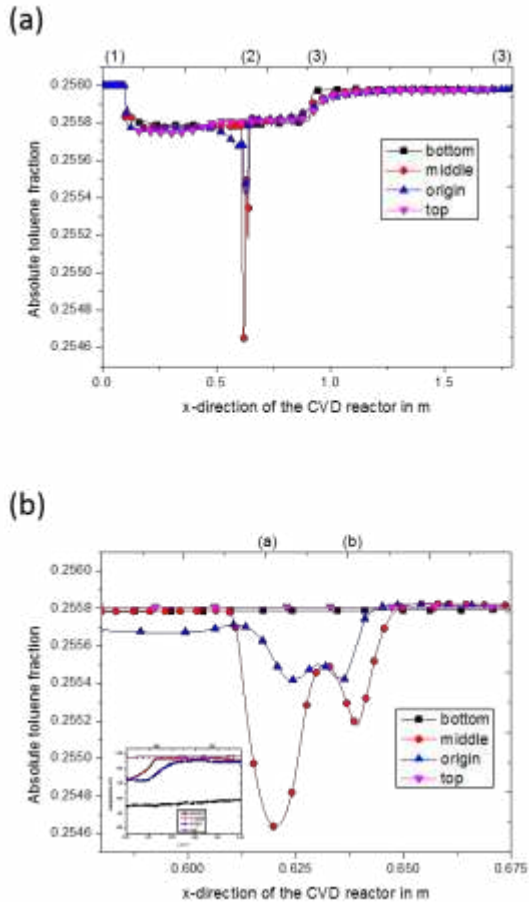
Figure 4.11: Plotted mass fraction of toluene in the CVD reactor (a) and in the surroundings of the samples (b).

As mentioned, the sample position cannot be changed to prevent a temperature gradient between the 1st and the 2nd sample row. The existing optimal distance of the specimens in the CVD reactor to the reactor inlet for

an optimal replication process, which corresponds with an ideal temperature range, cannot be changed. However, this behaviour can be prevented using a thermal barrier, as shown in Figure 4.12. Because of that, the specimens in the 1st row reach the set temperature of 1033 K (760 °C), which is optimal for the replication process. The barrier caused a temperature difference between the 1st and 2nd row of ~5 °C. Consequently, the specimens do not exhibit any deformations, which is confirmed by the synthesis of cylindrical specimens for various analysis.

Figure 4.12: Effect of a thermal barrier on the specimens temperature.

4.2   Tailored properties of Aerographite

Based on the investigated growth mechanism the properties of Aerographite were modified by varying the wall thickness and graphitisation degree. Their influence on the electrical properties of neat Aerographite and the mechanical properties of Aerographite-epoxy composites are discussed briefly. Firstly, the fundamentals of the graphitisation via thermal treatment of Aerographite are shown in detail.

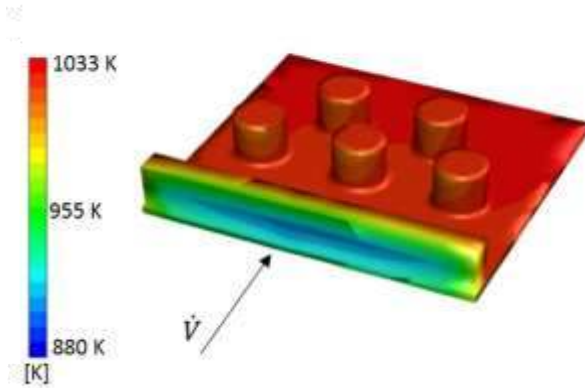### 4.2.1   Basics and effect of thermal treatment on the properties of Aerographite

The thermal treatment is an effective method when it comes to healing of carbon lattices and the improvement of carbon structures, as already known. Similar to CNTs [41–44], Figure 4.13 shows the reorientation and healing of defects between graphitic pieces in Aerographite.

As TEM images in chapter 4.1 and Figure 4.13a have already shown, untreated (as received) Aerographite shows an irregular arrangement of discontinuous graphitic pieces in the arrangement of carbon layers. The formed graphitic pieces are orientated as single pieces with a geometric displacement against the next layer (1) or without a geometric displacement (2), as marked in the inset (Figure 4.13a). Due to the thermal treatment of Aerographite, these defects can be cured, whereby the graphitic pieces join and form comprehensive carbon layers, to be seen in Figure 4.13b,c and its insets. Even the thermal treatment cures lattice defects in Aerographite, the formation of amorphous carbon on the surface into layers of graphitic does not occur, as shown by the inset in Figure 4.13b.

However, not all defects can be healed perfectly, so as the insets of Figure 4.13b,c show, inter-layer breaks still occur, which are red marked. In

consequence of the temperature treatment, these defects are decreasing with increasing temperatures.
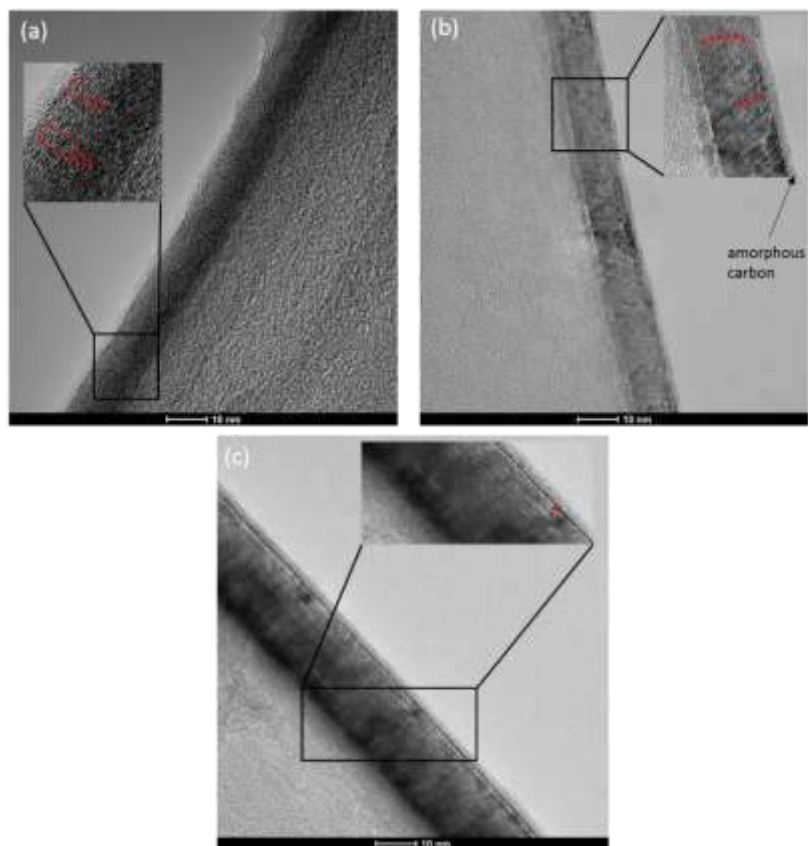
Figure 4.13: TEM images of untreated Aerographite (a), treated at 1800 °C (b), treated at 2200 °C (c), all structures show a wall thickness of ~16 nm, with a scale of ~15 nm in the insets.

EELS data (Figure 4.14a-c) are used to determine the sp^2 and sp^3 content in Aerographite according to [169]. As reference, a spectrum of graphite is

shown as inset in Figure 4.14a and in more detail as Figure A3. Graphite exhibits a clear π^*/ σ^* peak at 285 eV/292 eV.

The spectra are recorded in an energy range of E= 280 – 320 eV. Carbon structures exhibit two characteristic peaks. The 1s $\rightarrow$ π^* transition at ~ 284 eV on the one hand and the 1s $\rightarrow$ σ^* transition peak at ~291 eV on the other hand. Each spectrum is normalised and the background is corrected with a multiple-scattering method.

By plotting the calculated sp² and sp³ amounts versus untreated and thermally treated Aerographite (Figure 4.14c), exhibits a continuous increase/decrease in sp²/sp³ content with applied temperature. This behaviour confirms TEM observations as previously shown in Figure 4.13. Untreated Aerographite shows a sp³ content of ~70 %, which is decreased by thermal treatment to ~18 %. Contemporaneously, the sp² content increases with the thermal treatment from ~30 % up to ~82 %.
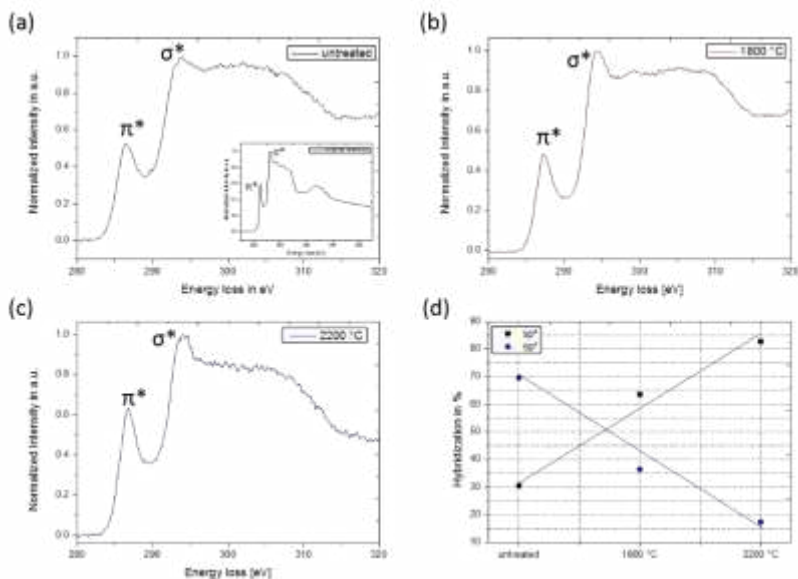
Figure 4.14: EELS spectra of untreated (a), 1800 °C treated (b), and 2200 °C treated Aerographite.

Figure 4.15 shows TEM images of thermally treated Aerographite by variation of the holding time between 0 min and 240 min, at a constant temperature of 1800 °C. Even a heating up without a holding time leads to an arrangement of carbon atoms in a lattice structure, as shown in Figure 4.15a. In dependency of the holding time a healing of defects, such as gaps between graphitic layers are cured continuously with the applied temperature (Figure 4.15b-e).

In order to be able to compare the effect of the treatment process on the properties, such as the electrical conductivity, of the individual specimens, they exhibit a wall thickness of ~10 nm.
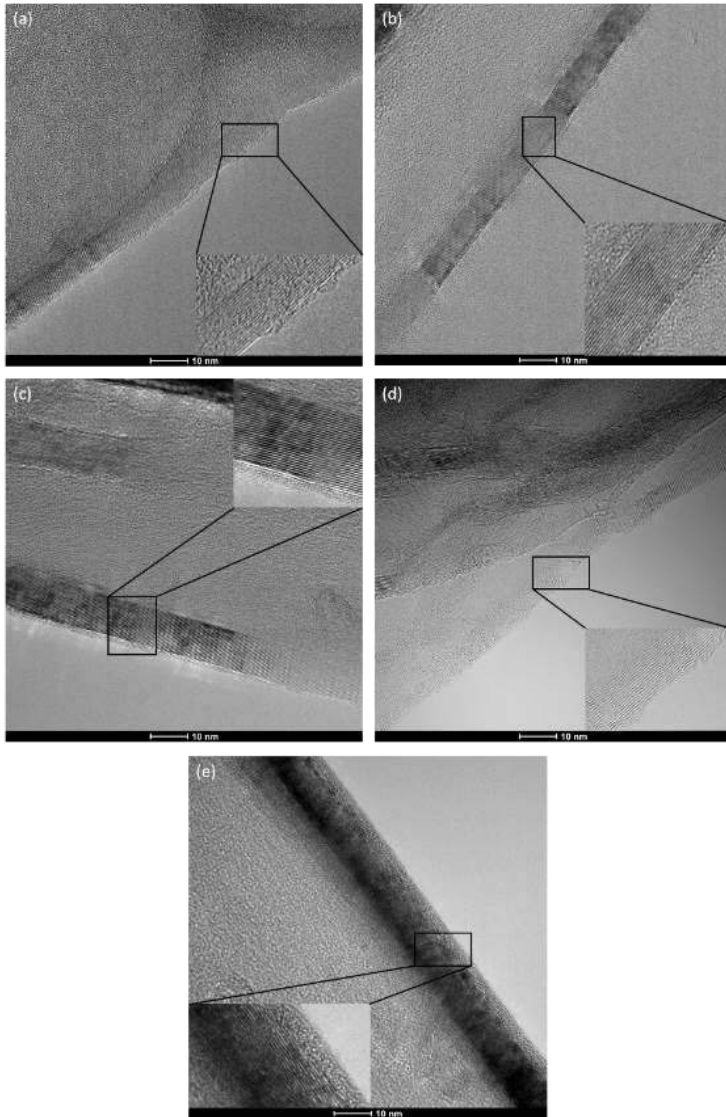
Figure 4.15: TEM images of treated (1800 °C) Aerographite dependent on the holding time: 0 min (a), 30 min (b), 60 min (c), 120 min (d) and 240 min (e), with a scale of ~15 nm in the insets.

The graphitisation of the graphitic pieces and their healing to graphitic layers is additionally analysed via Raman spectroscopy, as shown in Figure 4.16. The thermal treatment of carbon structures, such as CNTs or Aerographite, leads to a healing of structural defects [41–44], as presented in Figure 4.16a. Untreated Aerographite shows a characteristic D-band at ~1330 cm^{-1} and a G-band at ~1580 cm^{-1}, with a D/G ratio higher than 1 [166], as presented in Figure 4.5a. This ratio of the defect density is caused by the diffusion of the reaction species, such as Zn, H_2O through the formed carbon wall, as described in chapter 4.1. Furthermore, the Raman spectra have shown the missing of a clear G' signal at ~2645 cm^{-1} [35,48,166], which indicates a highly unorientated arrangement of carbon atoms. Here, the graphitic pieces are joined to layers as shown by the TEM observations, whereby the D/G ratio decrease significantly below 1, which is accompanied by a higher graphitic orientation of sp^2 hybridised carbon. The graphitisation of carbon structures also leads to a shift of the G-band position from ~1573 cm^{-1} to 1577 cm^{-1}, which is additionally described for CNTs [42] and can be explained by the increase of the graphitic arrangement. Besides, the thermal treatment also shows the formation or splitting of the G-band into a D´-band. This phenomena is described in CNTs as well [42]. The formation of the D´-band describes as well as the D-band, defects in sp^2 lattices such as crosslinking between the carbon layers [192,193]. Due to the graphitisation process the intensity of the D´-band decreases continuously with the applied temperature. This confirms the healing process and the reduction of defects, such as crosslinking's and atomic disorders in the lattices. However, the formation of D´-bands as mentioned in chapter 2.1.3 is not completely clarified yet.

Moreover, the treatment process leads to the formation of the 2D band, or G'-band called, at ~2645 cm^{-1}. Contrary to graphite, a formation of the 2D-1 and

the 2D-2 band [194] does not occur, which is mainly caused by the smaller layer thicknesses or wall thicknesses of 3-20 nm, which is comparable to MWCNTs. The 2D-band indicates a higher order in sp^2 lattices, similar to graphite [99].

Besides the treatment temperature, the holding time is a key parameter for the subatomic healing of carbon structures, as shown in Figure 4.16b. Here, the holding time is varied between 0 minutes and 240 minutes. When starting the thermal treatment an immediately healing of the carbon structures can be observed, which increase with the treatment time. At the beginning, in addition to the formation of the D´ and G´ bands, further bands are formed with a Raman shift of 1650 cm^{-1} to 1770 cm^{-1}. Even by the thermal treatment, these do not completely disappear and are retained a reduced influence. It should be noted that these bands occur regardless of the treatment temperature and thus have no influence on the properties.
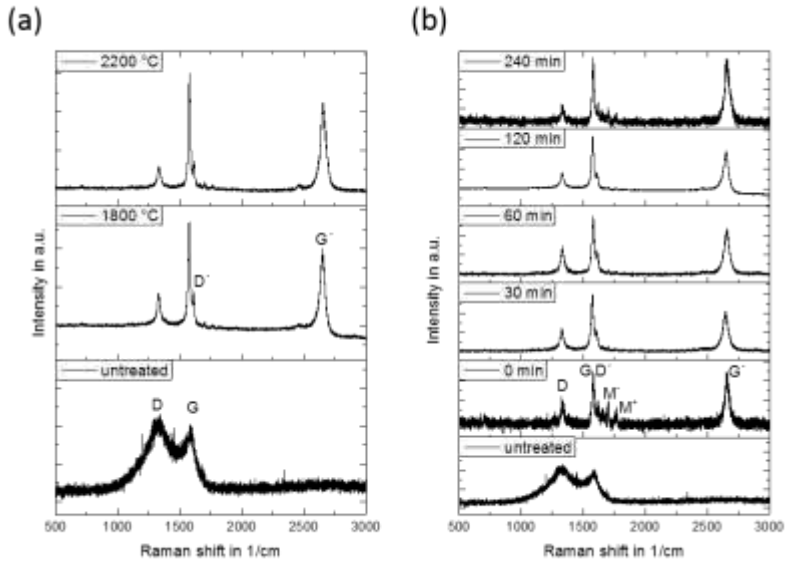
Figure 4.16: Exemplary Raman spectra of annealed Aerographite, dependent on the temperature (a) and on the holding time at 1800 °C (b).

XRD diffractograms of untreated and thermally treated Aerographite, dependent on the treatment temperature after a baseline correction are shown in Figure 4.17. Structural information's or changes can be estimated plotting the intensity versus the set angle (2θ). It´s noteworthy, that carbon structures shown a characteristic peak at ~25°-26°, called ($d_{(002)}$). This peak increase significantly by the treatment process. To determine the structural changes by the treatment process, the distance d between layers can be calculated using the Bragg equation (4.7).

$$d_{(002)} = \frac{\lambda}{2sin\theta}/10 \; in \; nm \qquad (4.7)$$

Where:

λ – Wavelength of the source (Cu K$_\alpha$: 1.5418 Å)

θ – Peak position in °

The thermal treatment leads to a shift of the peak maximum from 25.91° to 25.75° with an increased temperature, which is away from the ideal graphite distance. This shift in the measured peak angle can be additionally observed of thermally treated Aerographite dependent the holding time from 25.43° to 25.64°. The significantly increase in the d$_{(002)}$ intensity depends on the applied temperature during the treatment process. It is noteworthy that further peaks do not appear during the treatment process.
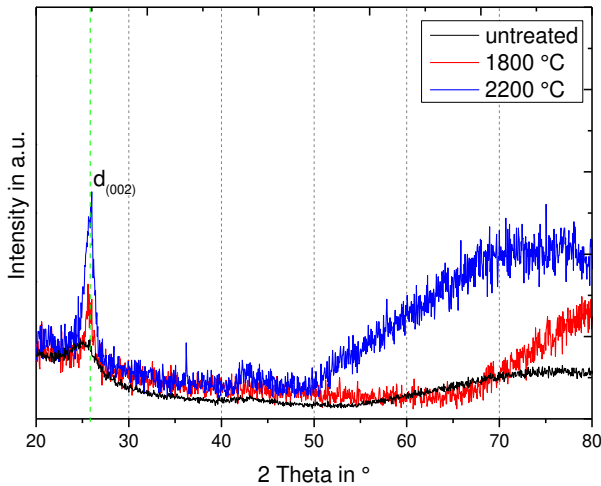
Figure 4.17: XRD diffractogramm of Aerographite dependent on the treatment temperature.

Besides, XRD technique, Raman spectroscopy is an established method to determine structural modifications, such as graphitisation processes in carbon structures. Raman spectroscopy was used additionally to investigate the graphitisation progress in Aerographite. For a correlation of the electrical conductivity and thermal stability with structural changes, it is important to know the degree of graphitisation. The graphitisation degree g, also known as crystallinity index, can be calculated compared to equation (4.8) with the measured I_D/I_G ratio. This empirical equation was developed based on the results of *Chandrasekaran* by determining I_D/I_G ratios and graphitisation of CNTs and graphene structures [175]. Moreover, the graphitisation degree G after *Vázquez-Santos et al.* is determined according to equation (4.9) and is also based on Raman techniques, which is more informative for highly graphitised carbon structures than the I_D/I_G ratio. Comparing Raman techniques with XRD measurements, a determination of $I_G/(I_D/I_G)$ ratios exhibit an exact graphitisation process [94]. In the following, both analytic equations are compared.

$$g = 99.54 - 41.92 \ (I_D/I_G) \qquad (4.8)$$

$$G = \frac{I_G}{I_D + I_G} \cdot 100 \qquad (4.9)$$

In contrast to Raman based techniques, the graphitisation degree g_{XRD} using XRD can also be determined according to equation (4.10) [195].

$$g_{XRD} = \frac{C_{area}}{F_{area}} \cdot 100 \ in \ \% \qquad (4.10)$$

Where:

C_{area} = area under crystalline peak after background removal

F_{area} = area of the obtained diffractogram before background removal

The influence of the treatment temperature on the crystalline width and the degree of graphitisation is shown in Figure 4.18. The I_D/I_G ratio is plotted versus the calculated crystalline width according to equation (4.6) in Figure 4.18a. The thermal graphitisation leads to a healing of defects as already shown by TEM observations. Whereas, a continuous increase of treatment temperature leads to a constantly decrease of I_D/I_G ratio and an asymptotically rise in the crystalline width. The treatment process allows an increase in the crystalline width of ~600 % from ~4 nm to ~24 nm. A comparison of the degree of graphitisation according to equation (4.8), (4.9) and (4.10) and the determination of the sp² content via EELS measurements versus the treatment temperature is shown in Figure 4.18b. The graphitisation degree of untreated Aerographite yields about 40 % for both calculation methods. Thus, the determination of the sp² amount by means of EELS measurements can be assumed as the lower limit of the graphitisation degree, whereas its determination by means of equation (4.10) represents the upper and more realistic limit. However, it can be assumed that the true degree of graphitisation is somewhere in between both values. A variation of the holding time at a treatment temperature of 1800 °C, as presented in Figure 4.18c, shows a continuously increase of the crystalline width versus the measured I_D/I_G ratio. Consequently, the introduced energy for the reorientation and arrangement of carbon atoms in an ideal lattice is affected, not only by the temperature but the holding time as well. The crystalline

width increases by 0.5 nm/(I_D/I_G). The determination of the graphitisation degree, as present in Figure 4.18d shows similar to the temperature influence an upper and lower limit. The determination via Raman spectroscopy exhibits a more realistic description of the occurred processes. In general, the determination of the graphitisation degree using the introduced calculation methods is not standardised. Based on the calculated values a lower and upper graphitisation can be assumed. However, the upper graphitisation, which follows a non-linear behaviour seems to be more realistic. In particular, because of the destructive effect of temperatures >2800 °C [44], a further continuously linear increasing in the graphitisation degree is not possible. Consequently, a true graphitisation degree can be estimated between the lower and the upper degree. Furthermore, it is noteworthy that by comparing different calculation and analysis methods, their penetration depth is in a range from a few nanometers (Raman) to several micrometers (XRD) [94].
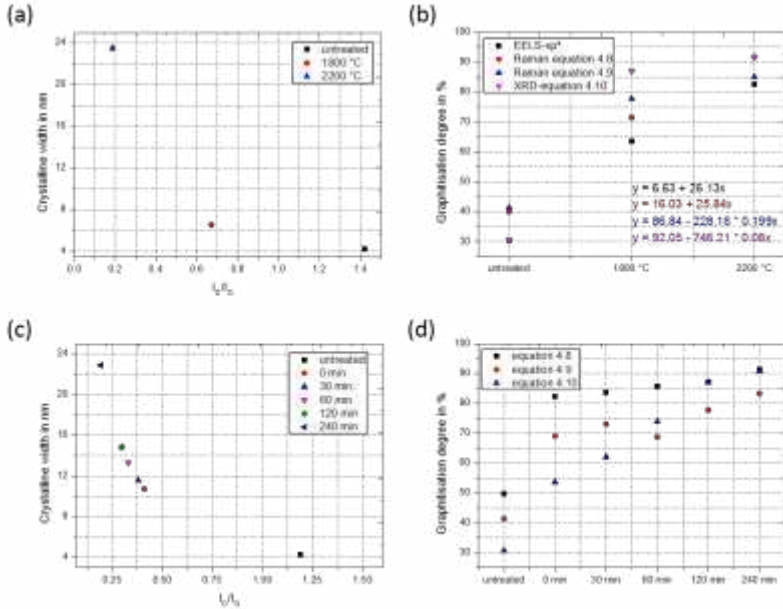
Figure 4.18: Crystalline width depending on the temperature with a constant wall thickness of ~16 nm (a) and graphitisation degree depending on the treatment temperature (b), crystalline width depending on the holding time with a constant wall thickness of ~10 nm (c) and graphitisation degree (d).

The healing of graphitic layers and their alignment leads to an increased electrical conductivity from 3.3 S/m for untreated to up to 27 S/m for annealed Aerographite as shown in Figure 4.19a. The electrical conductivity increases continuously with an increasing annealing temperature. A holding time of the temperature was set to 2 h for annealing. To investigate the influence of the holding time on the reorientation of the graphitic layers and the healing process, the holding time was varied, as shown in Figure 4.19b. A linear increase of the electrical conductivity with the holding time up to 60 min can be observed, whereas the electrical conductivity increases with 0.02

S/(m · min) of the thermal treatment. It can be estimated, that by a further increase in the treatment temperature, the electrical conductivity reaches a plateau.
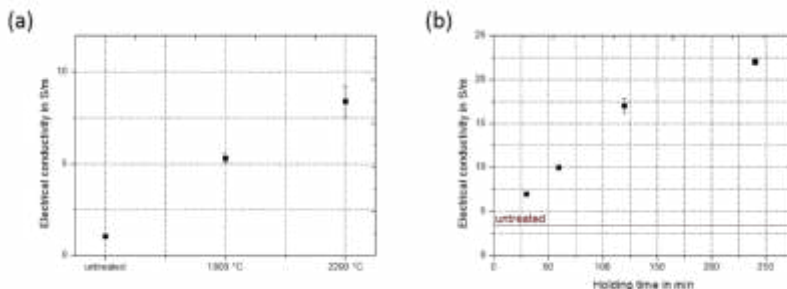
Figure 4.19: Electrical conductivity of annealed Aerographite; depending on the temperature (a) and on holding time at 1800 °C (b).

The healing of graphitic layers is also reflected in the temperature resistance of Aerographite, measured via TGA techniques, which increases with the applied treatment temperature, as shown in Figure 4.20a. Here, the oxidation temperature of untreated Aerographite (~660 °C) is improved by the thermal annealing up to ~752 °C. This behaviour can be explained with the increased crystalline width, which automatically leads to reduce contact points for the occurred oxidation of the carbon structure. Additionally, the variation of the holding time during the thermal treatment leads to a continuous increase of the oxidation temperature (Figure 4.20b), which correlates with a time-dependent rearrangement of the carbon atoms in a hexagonal lattice.

The results of the calculated graphitisation degree exhibit an ideal linear increase at first, before changing to a non-linear increase, which reaches an

optimum (Figure 4.18b,d). This behaviour of a not-linear increase is confirmed by the determination of the oxidation temperature.
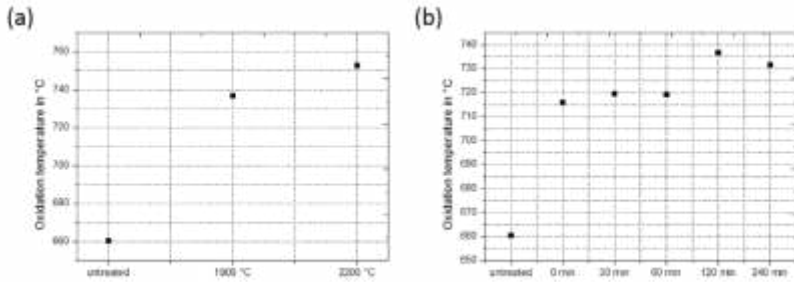
Figure 4.20: Influence of the thermal annealing on the oxidation temperature of Aerographite; depending on the temperature (a), on the holding time at 1800 °C (b).

In conclusion, the thermal treatment leads to an improved arrangement of the graphitic pieces and their healing to graphitic layers. Thus, the physical properties, such as the electrical conductivity and oxidation temperature, are improved by high temperatures. The variation of the holding time at 1800 °C also leads to increased properties, but a plateau is reached with a holding time above 120 min.

4.2.2 Effect of wall thicknesses and graphitisation on structural properties of Aerographite and fundamentals of its electrical conductivity

The controlled reduction of the wall thickness of Aerographite is already explained in chapter 4.1 and the data exhibit indicates a linear growth behaviour. The respective SEM images are shown in Figure A4. For the

91

investigation of the temperature-dependent electrical conductivity of Aerographite dependent of the wall thickness and graphitisation, wall thicknesses between 3 and 22 nm are used as summarised in detail in Table 4.1. It should be noted that the injection time of 60* min were used, despite of the leaking injection unit, in order to achieve an intermediate wall thickness. Furthermore, the graphitisation leads to a reduction in the wall thickness, which can be explained with the orientation of graphitic layers. The standard deviation (min. 3 measurements at different tetrapods) of the measured wall thickness indicates steady growth behaviour.

Table 4.1: Measured wall thicknesses dependent on the injection time, *leaking of the injection unit.*

Injection time of the carbon source in minutes	Wall thickness in nm (untreated)	Wall thickness in nm (treated)
15	6.13 ± 0.36	3.31 ± 0.07
20	9.93 ± 0.24	8.73 ± 0.25
45	14.04 ± 1.04	12.18 ± 0.95
60*	17.10 ± 1.77	13.43 ± 0.24
60	22.39 ± 0.61	16.80 ± 1.22

Garlof et al. already reported an enhanced electrical conductivity with increased densities of Aerographite [35]. This behaviour is also shown for untreated Aerographite with increased wall thicknesses as presented in Figure 4.21a. Based on (4.8), the charge carrier concentration increases with the wall

thickness and at the same time a reduction of the influence of the surface defects can be assumed. Besides, the defect density, the charge carrier is a key parameter when describing the electrical conductivity. An increasing of the wall thickness leads to a minimized influence of the surface defects, whereas with lower wall thicknesses, this influence increases and as a result, the electrical conductivity is reduced. Furthermore, with increasing of the wall thickness an increased charge carrier is assumed. Contrary to this phenomenon, the electrical conductivity increased for thermally treated Aerographite with reduced wall thicknesses, which is similar to the behaviour of graphene [55]. This behaviour for highly oriented Aerographite is similar to carbon fibers, which also show a high carbon orientation, in which with decreasing diameter the mechanical properties reach a certain maximum [196]. This behaviour is related to the probability of defects within the existing volume, which decrease with the cross-sectional area of the conductor tracks. In comparison to untreated Aerographite and constant charge carrier densities, the graphitisation leads to a reduced defect density and higher electrical conductivities. Hereby, the possibility of defects decreases with a smaller volume. Moreover, a correlation of wall thickness and I_D/I_G ratio can be observed, as shown in Figure 4.21b. An optimum wall thickness of ~14 nm for untreated Aerographite and a shifted optimum of ~12 nm for thermally treated Aerographite are achieved. This minimal I_D/I_G ratio is based on the growth mechanism of Aerographite, in which the diffusion of by-products, such as water and Zn, through the carbon wall, catalyse the graphitisation of amorphous carbon into graphitic pieces. A critical wall thickness of 10-12 nm could be identified [166]. However, defects in general and surface defects in particular have a significant influence on the electrical properties. The wall thickness which correlates with the tetrapod diameter of Aerographite has an influence of the I_D/I_G ratio and is already published for

carbon fibers [197]. Based on the calculated slopes a dependency of the I_D/I_G ratio per nanometer wall thickness of 0.02 for untreated Aerographite and 0.06 for treated Aerographite can be assumed. As a consequence a comparison of different Aerograpphite specimens is only possible with comparable wall thicknesses.
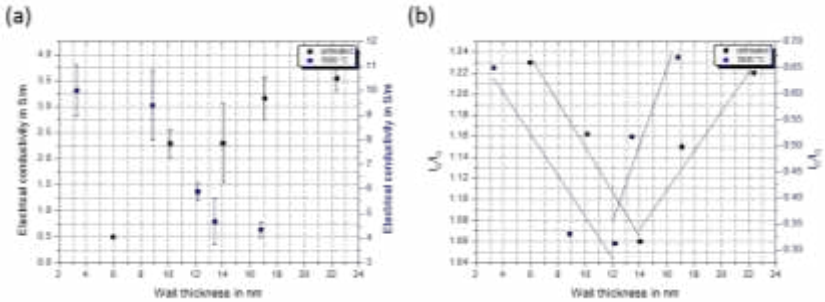
Figure 4.21: Dependency of the electrical conductivity on the wall thickness of Aerographite measured at room temperature (a), dependency of the I_D/I_G ratio on the wall thickness (b).

Based on the observed relation between electrical conductivity and I_D/I_G ratio, a fundamental equation (4.11) for the description of defective and structural influences on the electrical conductivity of Aerographite was developed and published [193,198]. Since, as described in chapter 4.1, the formation of "dead ends" occurs, this phenomenon is considered in the equation. As a result, the total electrical conductivity (σ_{tot}) is composed of the conductivity of the number n of electrical paths σ_c of connected tetrapods, and of the tunneling effect σ_t. The tunnel effect's contribution to the total conductivity is rather small and thus can be neglected. The electrical paths are a function of the charge carrier density σ_{CCD}, the defect density σ_{DD} and especially surface defects σ_s as shown in equation (4.12).

$$\sigma_{tot} = n \cdot f(\sigma_c) + \sigma_t \qquad\qquad (4.11)$$

$$f(\sigma_c) = \sigma_{CCD} + \sigma_{DD} + \sigma_s \qquad\qquad (4.12)$$

The temperature-dependent electrical conductivity of untreated Aerographite (Figure 4.22a) shows a metallic conductive behaviour, in which the electrical resistance increases continuously with the applied temperature. *Fischer et al.* [199] showed a metallic conductive behaviour for CNTs by measuring the temperature-dependent electrical conductivity. The metallic conductive character, presented in Figure 4.22b, remains after thermal treatment at 1800 °C. However, the thermally treated structures exhibit a maximum of the electrical conductivity at about 100 °C. This maximum is probably caused by an improvement in the tunneling of the charge carriers in the carbon foam. The phenome of a local maxima at 100 °C for thermally treated Aerographite is not completely understood yet.
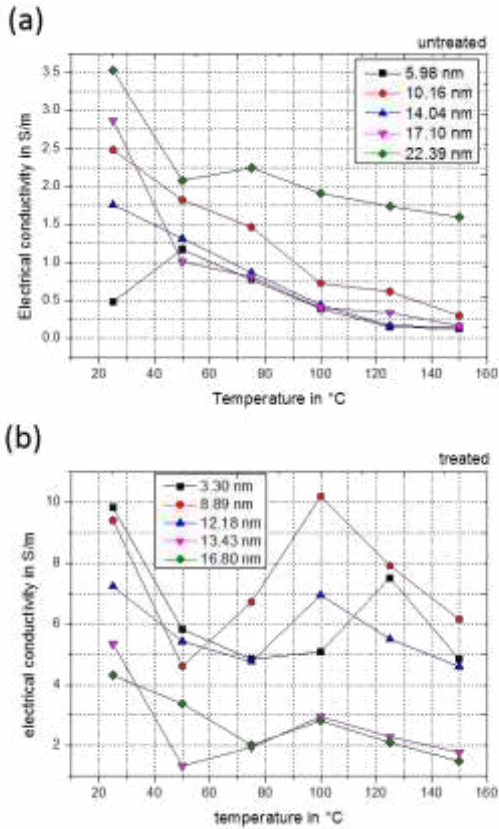
Figure 4.22: Temperature-dependent electrical conductivity of untreated Aerographite (a), and of treated Aerographite (b) with different wall thicknesses.

Based on the measured specific resistance (ρ_R) the band gap energy (E_g) is calculated via equation (2.7) [39]. Consequently, the calculated band gap energy of untreated Aerographite is reduced with increasing wall thickness, contrary to thermally treated Aerographite (Figure 4.23a). The behaviour of

untreated Aerographite corresponds with the observed mechanism of CNTs [39]. A band gap energy of 0.4 - 2.3 eV has been calculated for the entire carbon foam, which is typical for semiconductive materials. Figure 4.23b shows a layer dependent calculation of the band gap energy in Aerographite. The results indicate a decreased band gap energy with increased electrical conductivity. Furthermore, a minimal band gap energy at an electrical conductivity of ~4 S/m is observed. Thus, these calculated layer-dependent band gap energies correspond in their range to those of CNTs as calculated in [39,200]. In Figure 4.23c,d $\ln(\sigma)$ is plotted versus 1000/T. The slope of the fitted curves shows an increase in the temperature-dependent electrical conductivity with increasing wall thickness, which confirms the previously made observations. Moreover, the metallic conductive behaviour for treated Aerographite can be identified clearly. However, based on the observed slopes a transformation process by the thermal treatment can be assumed. Consequently, the electrical conductivity should change its characteristic with increasing temperatures.
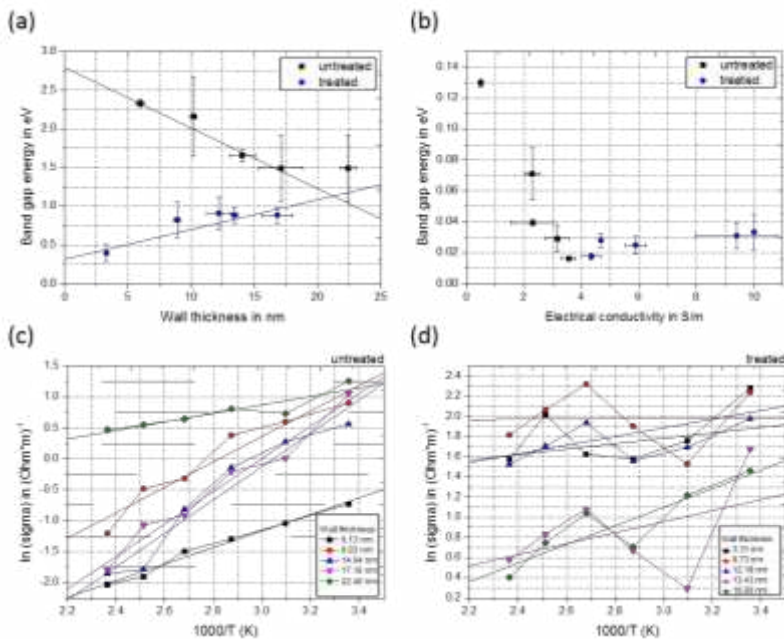
Figure 4.23: Dependence of band gap energy on the wall thickness of the entire carbon structure at 25 °C (a), dependence of the electrical conductivity on the band gap energy of the individual graphitic layers (b), variation of ln(σ) versus 1000/T of untreated Aerographite (c), variation of ln(σ) versus 1000/T of treated Aerographite (d).

This transformation process is completed at a treatment temperature of 2200 °C, in which thermally treated Aerographite exhibits a semiconductive character as graphene [55]. This behavior is confirmed by the increased crystalline width Aerographite, as shown in chapter 4.2.1, which is leading to a highly graphitised structure and a similar behaviour to graphene. Hence, by further treatment at 2200 °C, the metallic conductive character of Aerographite is changed into a semiconductive behaviour, as shown in Figure

4.24a and more significant by the plotted $\ln(\sigma)$ above 1000/T curves in Figure 4.24b.

Similar to CNTs, these changes in the electrical conductive properties are also caused by a displacement of the bands or by a reorientation of carbon layers. This transformation process has not yet been described for carbon nanostructures.
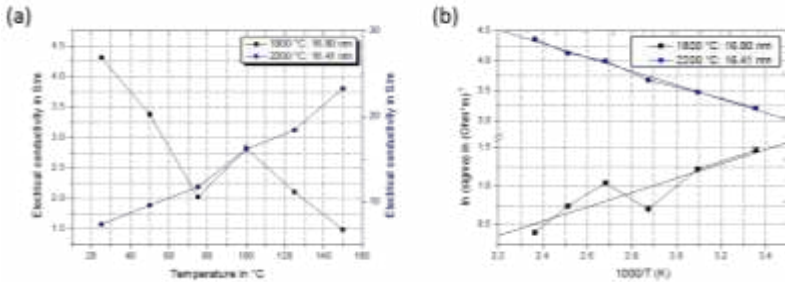
Figure 4.24: Temperature-dependent electrical conductivity of annealed Aerographite at 1800 °C (black curve) and 2200 °C (blue curve) (a), plotted $\ln(\sigma)$ versus 1000/T of 1800 °C (black) and 2200 °C (blue) treated Aerographite.

4.2.3 Effect of crystalline width on the fracture toughness and failure mechanism of Aerographite-epoxy-composite in SEN-3PB tests

Reductions of the wall thickness as well as graphitisation lead to a change in the I_D/I_G ratio. Here, Aerographite with different wall thicknesses according to Table 4.1 was used to investigate the influence of the wall thickness and graphitisation on the fracture toughness of Aerographite-epoxy-composite in SEN-3PB tests [201]. However, only wall thicknesses >10 nm were suitable for infiltration with epoxy resin.

The crystalline width, which is plotted versus the wall thickness in Figure 4.25, can be calculated on the basis of equation 4.2 by determining the I_D/I_G ratios. For the description of the dependency of crystalline width on the wall thickness of Aerographite, the calculated values are labeled with (A1-A3) for untreated and (B1-B3) for thermally treated Aerographite (Figure 4.25). A reduction of the crystalline width with an increasing wall thickness in dependency of the thermal treatment can be assumed. The crystalline width of untreated Aerographite decreases from ~4.2 nm (A1) to ~3.6 nm (A3). A similar dependency is observed for treated Aerographite from ~14 nm (B1) to ~6.5 nm (B3). The reduction of the crystalline width is caused by the growth mechanism [166,198]. This behaviour can be explained with the increasing diffusion length of the produced by-products through the formed carbon wall. Consequently, with an increased wall thickness the crystalline width is reduced by disturbing the arrangement of carbon into graphitic layers, which leads to high defective structures.
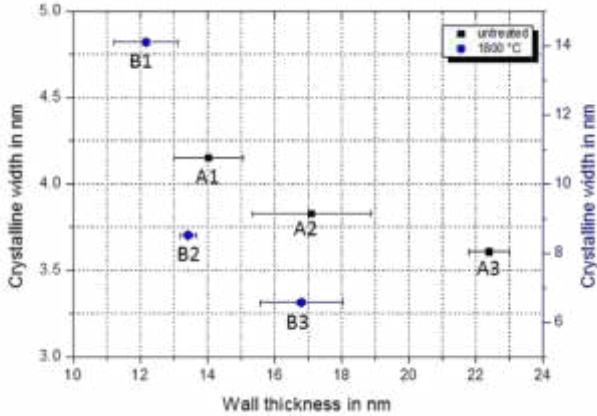
Figure 4.25: Crystalline width of untreated and thermally treated Aerographite dependent on the wall thickness.

As a consequence of the reduction in the crystalline width with increasing wall thicknesses (A3-B3), an improved K_{IC} value is achieved, as shown in Figure 4.26a. Hence, a high crystalline width with thinner walls leads to a reduced K_{IC} value (A1-B1). It is noteworthy, that small variations of even few nanometers in the wall thickness of Aerographite are leading to measurable K_{IC} values. Comparing the fracture toughness of untreated and thermally treated Aerographite a clearly reduced K_{IC} is observed. This reduction is caused by the increased crystalline width and the decreased wall thickness in treated Aerographite. However, similar wall thicknesses of untreated and thermally treated Aerographite have not a significant influence on the mechanical properties. This behaviour is contrary to the observed electrical conductivity, in which the properties increase for thermally treated Aerographite with reduced wall thickness. Consequently, it is not possible to

tailor the properties of Aerographite in a way that high mechanical and electrical values are accomplished. In conclusion, the increase in the crystalline width by thermal treatment increases, on the one hand the electrical conductivity and decreases on the other hand the mechanical properties of composites. In Figure 4.26b, a minimum K_{IC} of ~1.16 MPa.m$^{1/2}$ is shown, plotting the fracture toughness versus the crystalline width. However, further increases in the crystalline width do not affect the resulting fracture toughness. Opposing to the electrical behaviour of thermally treated Aerographite, the mechanical properties are dependent of the number of layers but shows consequently a contrary behaviour to graphene [59] or CNTs [75]. The mechanical stiffness increases with decreased number of layers [59,75]. However, it should be noted that the mechanical test of Aerographite was carried out in epoxy composites, whereas the results of graphene or CNTs were simulated. A detailed overview about the achieved filler contents is shown in Table A1.
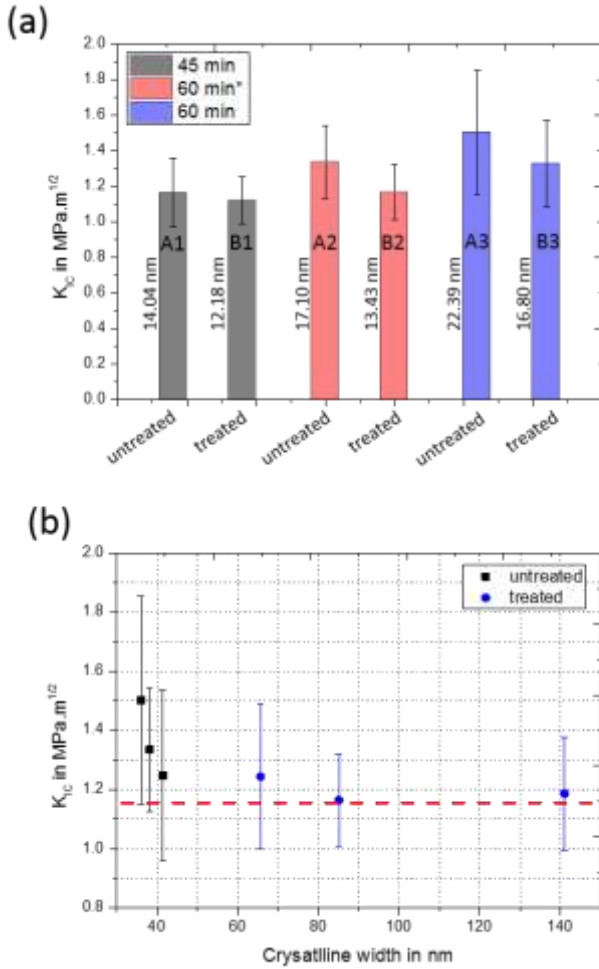
Figure 4.26: Comparison of K_{IC} values for untreated and thermally treated Aerographite-epoxy composites (a), minimum K_{IC} dependent on the crystalline width (b), with achieved filler contents of 0.32 wt.% - 0.49 wt.%.

Figure 4.27 shows exemplary SEM images of surface fractures of Aerographite-epoxy composites after mechanical testing with untreated and treated Aerographite. The observed behaviour of the fracture toughness in dependency of the wall thickness is also reflected in the fracture surface. The failure mechanisms are marked with (1)-(5). The mechanical stress during the three-point bending tests in the polymer composite with untreated Aerographite filler (Figure 4.27a and in its inset b) leads to three failure mechanisms, which are already described by *Chandrasekaran et al.* [48]:

(1) A pull-out of the tetrapod arms
(2) Complete extraction of a tetrapod from the matrix
(3) Breaking of the tetrapod arms.

Pull-outs of nano fillers such as CNTs are well known and already described in detail by *Gojny et al* [201]. This failure mechanism is dependent on the interfacial adhesion to the matrix system [202]. This insufficient bonding between Aerographite and the polymer matrix occurs using Aerographite without any functional surface groups and by the TEM observed amorphous carbon on the surface of the formed graphitic layers (Figure 4.13). These gaps are observed in dependent of the treatment process and wall thickness.

Furthermore, multiple and multi-dimensional fractures are shown in the polymer matrix (4), which are caused by the 3D interconnected structure of Aerographite. Due to the use of Aerographite as filler, additional cracks are guided around the tetrapod arms or through the tetrapodal structure, resulting in crack reversals. Besides, to the presented failures, a 2nd polymer phase is observed through the formation of holes/spheres.This 2nd phase, caused by the added flexibilizer and does not exhibit any influence on the crack propagation or the calculated values. Moreover, these occurred failure

mechanisms are also observed for treated Aerographite, shown in Figure A5. However, the thermal treatment of Aerographite leads to an additional failure behaviour (5), as shown in Figure 4.27c,d. As shown before, treated Aerographite exhibits a higher graphitisation degree and as a consequence of that a higher crystalline width. Due to this increased crystalline width, graphitic regions are tearing out of the tetrapod arms (5). This mechanism is comparable to the mechanism of graphene based PNCs, in which shearing off of graphene layers under mechanical load is already described [203].
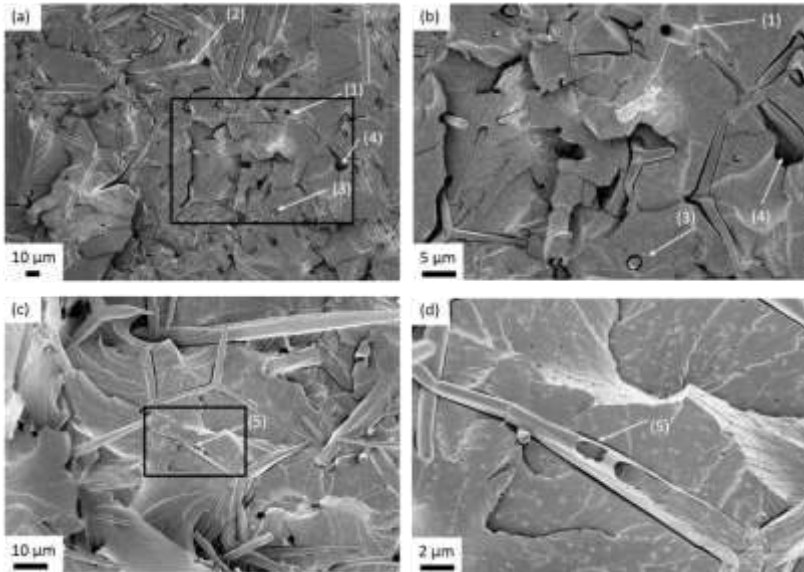

Figure 4.27: Fracture surface of Aerographite-epoxy composite with untreated Aerographite (a) and its magnification (b), treated Aerographite (c) and its magnification (d).

Finally, based on the calculated values and the observed failure mechanisms, a model for the description of the occurred behaviours was developed (Figure

4.28). This model of Aerographite includes the observed nanostructure of Aerographite walls, as shown in Figure 4.13a,b. A detailed scheme of the crack propagation in the carbon wall of Aerographite is shown in Figure A6. An increasing wall thickness, which corresponds with the number of layers, results in a higher crack path length and consequently higher fracture toughness. Due to the reduced crystalline width in untreated Aerographite, an increased crack path length can be assumed, as shown in Figure 4.28a. This behaviour can be explained by redirecting of the initiated cracks on graphitic pieces by passing through the tetrapod. A subsequent thermal treatment of Aerographite leads to a higher crystalline width on the one hand and to a reduced fracture toughness on the other hand. Figure 4.28b shows that the increased crystalline width is resulting in less redirections of cracks in the tetrapod arm. Hence, the initiated cracks are passing through the graphitic layers, which causes tearing out of graphitic regions in independency of the wall thickness of Aerographite. This mechanism is not observed for untreated Aerographite-polymer composites.

The mechanism of breaking single tetrapod arms is schematically shown in Figure 4.28c,d. Similar to the previously observed mechanisms, the initiation of cracks and their passing through the untreated tetrapod of Aerographite leads to several deflections on graphitic pieces and finally to the separation as presented in Figure 4.28c. By increasing of the wall thickness the total crack length can be increased, which correlates with the measured fracture toughness. The thermal treatment of Aerographite, with an increased crystalline width, shows gaps between the newly formed graphitic areas (Figure 4.28d). Due to these gaps, the initiated cracks can pass through the tetrapod arm without any deflections on these areas. This behaviour leads to the reduced fracture toughness in mechanical tests under bending load.
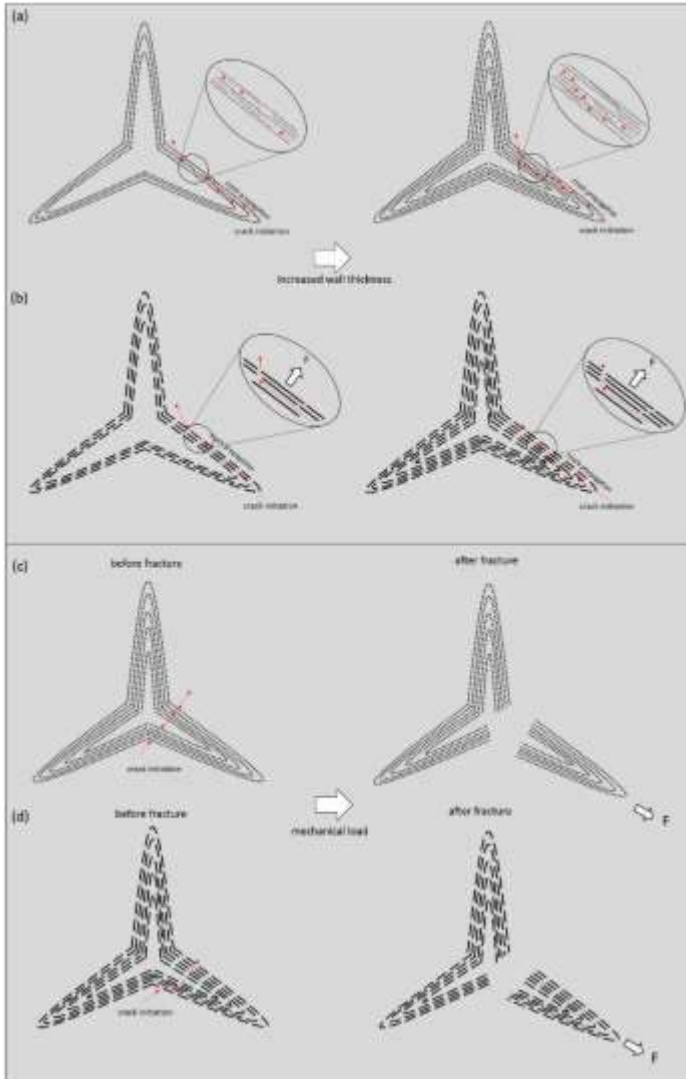
Figure 4.28: Model of failure mechanism in untreated (a) and treated (b) Aerographite-epoxy composites for crack propagation and breaking out mechanism, breaking mechanism of single tetrapods in untreated Aerographite (c) and in treated Aerographite (d).

107

4.3 Globugraphite and its application

This subchapter describes the fundamental properties and the potential application of Globugraphite as catalyst. Therefore, catalytic particles are chosen, based on thermodynamic calculations and incorporated into the carbon structure. The aim of this hierarchical structure is the application as energy storage system [165] or as catalyst [204,205], in which macro pores are used to infiltrate this foam as quick as possible. Due to the variation of the powder grain size different diameters of macro pores can be achieved.

4.3.1 Morphological characterisation and properties of Globugraphite

The morphology of the developed globular carbon foam (Globugraphite) depends decisively on the average grain size of the used ZnO powder, sintering cycle and the carbon injection rate in the CVD process [165]. The manufacturing of the ceramic template by the mixing of ZnO and PVB powder and the subsequent developed sintering process, results as Figure 4.29a-d shows in a porous hierarchical structure. The removing of the polymer binder leads to a macro porous (> 50 nm) structure. Besides, to the macro pores, due to the developed sintering process meso pores (2-50 nm) are formed by the formation of the sintering necks, as shown in Figure 4.29b,d. Moreover, replication process and the diffusion of by-products such as Zn and water through the formed carbon wall leads to the formation of graphitic pieces and resulting of this to micro pores < 2, as shown by TEM observations in Figure 4.31 and confirmed by BET measurement (Figure A7). Due to the CVD process, the globular morphology of the template is completely replicated, as to be seen in Figure 4.29e-h.

The results of the calculated SSA indicate a morphology dependent behaviour of the specific surface area. By using micro globular ZnO powder as basis for the ceramic template, Globugraphite exhibits a SSA of 376 m²/g, which increases using ZnO nano powder to 567 m²/g. Similar to Aerographite [28], Globugraphite exhibits a sub-morphology by decreasing the carbon feed rate, which leads to a SSA of 859 m²/g for a net-like structure. Here, the SSA is calculated using the quenched solid density functional theory (QSDFT). A decreasing powder grain size leads consequently to an increasing SSA. Most of the measured pores are derived of micro pores with a pore width of ~1.6 nm (Figure A7). These pores are resulting from the growth behaviour and the diffusion of reaction components through the carbon wall as described for Aerographite [166].
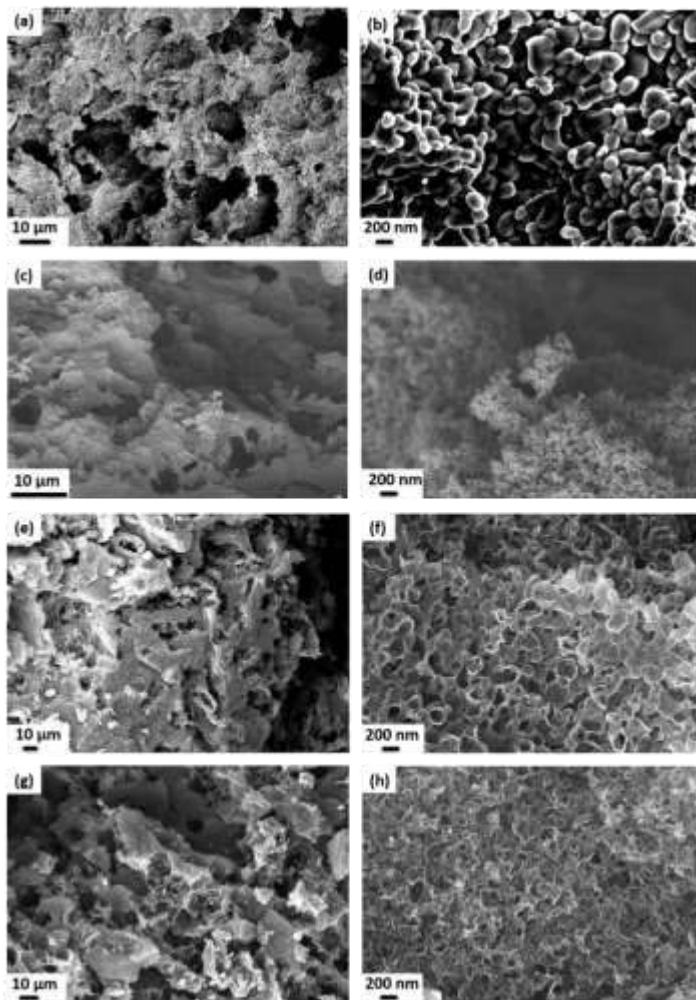
Figure 4.29: SEM images of the zinc oxide template with the hierarchical structure using a ZnO powder with a main grain size of several µm (a) and its magnification (b), ZnO powder with a grain size of several nm (c) and its magnification (d), replicated carbon structure (e) and its magnification (f), replicated carbon structure with nano structure (g) and its magnification (h).

The dependency of the morphology of Globugraphite on the carbon injection rate, similar to Aerographite [28], is shown in Figure 4.30a,b. By decreasing the carbon feed rate, the globular morphology is turned into a net-like structure as presented in Figure 4.30c at low toluene injection rates. However, the characteristic hierarchical structure remains. With this similarity to Aerographite, a dependency of the properties on the morphology can be assumed.
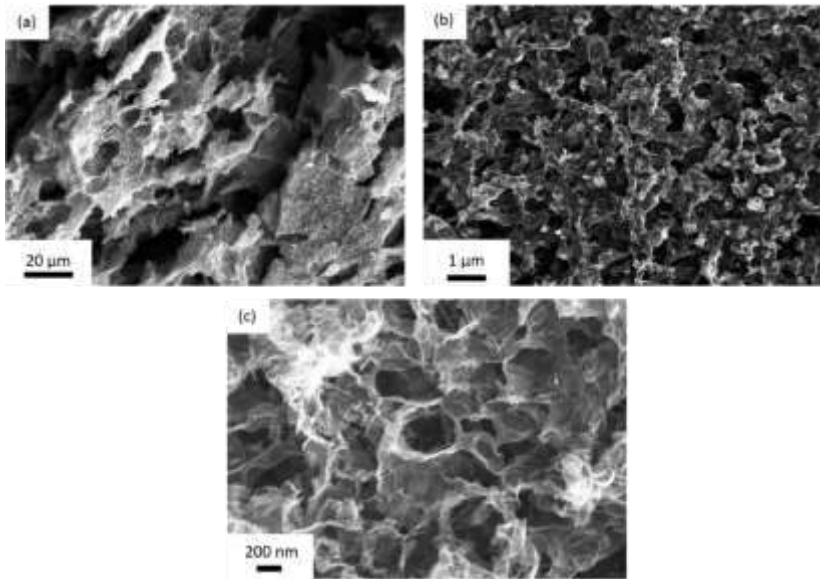
Figure 4.30: SEM image of the net-like carbon structure, overview (a), medium magnification (b), high magnification (c).

Based on the growth mechanism of Aerographite, the same chemical and physical reactions also apply for Globugraphite. Globugraphite has similar wall thicknesses as Aerographite at a carbon feed time of 60 minutes, as shown in Figure 4.31a. In the course of the carbon deposition on the template

surface and the simultaneous reduction of ZnO to gaseous zinc, the template material in the forming carbon shell also becomes entrapped, to be seen in Figure 4.31b, as already described for Aerographite in chapter 4.1. These incorporated ZnO nanoparticles can affect the properties of Globugraphite, such as the electrical conductivity or the electrochemical performance in energy storage systems. Due to the incorporated ZnO, an average amount of ~8 wt.% of ZnO remains after the oxidation of the carbon foam in the TGA under synthetic air, as presented in Figure A8. Similar to Aerographite, the globular carbon foam exhibits an identical thermal oxidative temperature of around 670-700 °C.
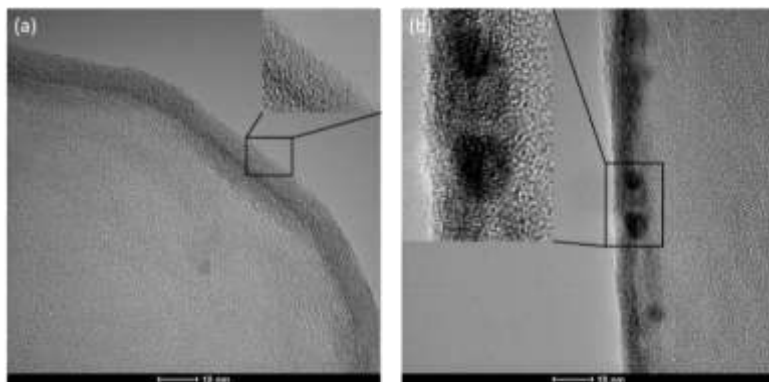
Figure 4.31: TEM image of Globugraphite carbon shell (a), with incorporate ZnO particles (b), with a scale of ~15 nm in the insets.

As a consequence of the morphology dependent properties, related to Aerographite [35], Globugraphite exhibits a similar behaviour. In contrast to Aerographite, a decrease in the electrical conductivity is observed with increasing density, as shown in Figure 4.32. Also, at low densities of ~20

112

mg/cm³ a reduced electrical conductivity is measured. An average density of 31-33 mg/cm³ leads to maximum conductivity. As shown by the results, Globugraphite reveals a continuously increasing electrical conductivity such as Aerographite [35].
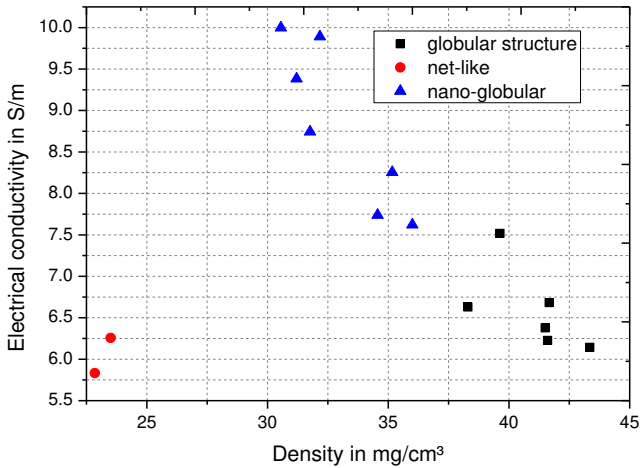
Figure 4.32: Comparison of the electrical conductivity in dependency of the density between the globular and net-like carbon structure.

Based on these results an equation (4.13) for the description of the total electrical conductivity (σ_{tot}) of Globugraphite was developed. This equation is composed of the function of the number n of conductive paths $f(\sigma_c)$ and the conductivity at the sintering necks σ_{SN} [193]. Using ZnO nano powder leads to an increase of the number of conductive paths with improved possible connectivity options by decreasing the grain size compare to ZnO micro powder. In contrast to Aerographite, a dependency of the electrical conductivity could not be observed in this fundamental study. It can be

assumed, that compared to Aerographite, the influence of other defects is negligible due to the higher number of conductive paths.

$$\sigma_{tot} = n \cdot f(\sigma_c) + \sigma_{SN} \qquad (4.13)$$

$$f(\sigma_c) = \sigma_{CCD} + \sigma_{DD} \qquad (4.14)$$

Resulting from this equation for the description of the conduction mechanism, the number of conductive paths in Globugraphite is identified as key parameter for the electrical conductivity. Here the number of conductive paths is increased with a decreasing particle size of the used ZnO powder.

4.3.2 Manufacturing of Globugraphite with incorporated catalytic particles

The manufacturing of Globugraphite with incorporated catalytic particles is described in detail in this subchapter. These catalytic particles are chosen, based on thermodynamic calculations. This recently developed manufacturing methods is also resulting in a patent application [205].

Besides, to the potential application as energy storage electrodes [165], this carbon foam is suitable as basic structure [204,205]. Based on the manufacturing process and the replication into the carbon structure, a catalyst structure based on the unique globular morphology of Globugraphite with incorporated catalytically active metals/metal oxide particles was developed. Due to a possible reduction of metal oxides by hydrogen, the Gibbs free energy for possible interactions/reactions of catalytically metal oxides with hydrogen was calculated, and summarised in Table 4.2 [204]. For the reduction of ZnO by hydrogen a Gibbs free energy of –68.83 kJ/mol was experimentally determined by *Clarke and Fray* [190], as shown in equation 4.4. Furthermore, the reduction of ZnO [188,189] by hydrogen and the reduction of titanium dioxide (titania-TiO_2) [206] in the presence of hydrogen

114

are also well known. Indeed, the reduction of magnesium oxide (MgO) in presence of hydrogen was not observed yet. MgO was used as catalyst for the catalytic decomposition of benzothiophenic and dibenzothiophenic sulfones [207], whereas titania is an already known photo catalyst [208]. To avoid the reduction of the catalytically active metal oxides, the Gibbs free energy must be greater than of the ZnO reduction.

The Gibbs free energy of possible occurred reactions of the added metal oxides was calculated according to equation 4.4 and summarised in 4.15-4.17. For the calculation of the Gibbs free energy of metal oxides and their products the published temperature behaviours of their respective components were used [209]. Besides to metal oxides, palladium (Pd) is used for the incorporation into the replicated carbon foam. Palladium is an excellent catalyst for the electrooxidation of formic acid or the production of hydrogen [210,211]. The advantage of palladium as a metal is that it cannot be further reduced. However, a spontaneous hydrogenation by palladium has been known for more than 150 years [212]. Consequently, the Gibbs free energy of palladium does not have to be calculated.

Table 4.2: Calculated Gibbs free energies of catalyst fillers based on their possible reactions with hydrogen at 760 °C.

$$TiO_2\,(s) + 2H_2\,(g) \rightarrow Ti\,(g) + 2H_2O\,(g) \qquad \begin{array}{l} \Delta G_R^0\,(TiO_2) = \\ 700.15\ kJ/mol \end{array} \qquad (4.15)$$

$$MgO\,(s) + H_2\,(g) \rightarrow Mg\,(g) + H_2O\,(g) \qquad \begin{array}{l} \Delta G_R^0\,(MgO) = \\ 329.37\ kJ/mol \end{array} \qquad (4.16)$$

$$Pd\,(s) + H_2\,(g)\,(s) \rightarrow PdH_2\,(s) \qquad\qquad\qquad\qquad (4.17)$$
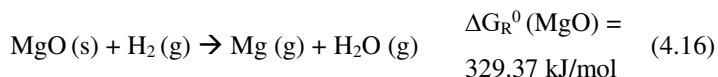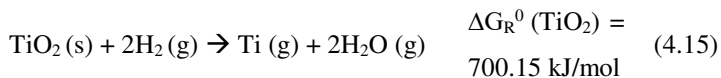
The used powders and their properties are summarised in

Table 4.3. The powders were added to the ZnO-PVB mixture as described in 3.1.2 for the manufacturing of the carbon-based catalyst structures. The respective metal oxides were added to the ZnO/PVB mixture with 1 vol.%, 3 vol.% and 5 vol.%, whereas only 1 vol.% palladium was used. The further production of the green bodies takes place as already described in chapter 3.1.2.

Table 4.3: Metal oxide and metal powders for the manufacturing process, from Sigma Aldrich®.

Powder	Average grain size in µm	Purity in %	Bulk density in g/cm³
TiO_2	< 10	99.0	4.23
MgO	< 5	99.9	3.58
Pd	< 1	99.9	12.02

The hierarchical morphology of the produced ceramic templates with additionally added metal oxides (TiO_2), at different amounts of 1 vol.%, 3 vol.% and 5 vol.%, are shown in Figure 4.33a,c,e and is not affected by these additives. To achieve a macro- and meso-porous morphology, similar to Globugraphite without any added particles, the same sintering cycle was used. Which leads to the formation of sintering necks between the ceramic powder (Figure 4.33b,d,f).

Figure 4.34 shows the replication from the globular ceramic template into the typical hollow carbon shells, as already shown for Globugraphite, with the simultaneous removal of ZnO by hydrogen. Moreover, the SEM observations indicates with an increased initial amount of TiO_2 additives, the remaining catalytic particles in the carbon structures increases as well, as shown in Figure 4.34 b,d,f. However, as previously discussed, it can be assumed that an amount of ZnO residue of ~9 wt.% remains in the carbon shell.

Figure 4.33: SEM image of the porous ceramic structure after the sintering process with incorporated TiO_2 (1 vol.%) particles (a), insert of the overview (b), overview of the ceramic template with 3 vol.% TiO_2 (c), insert of the overview (d), overview of the ceramic template with 5 vol.% TiO_2 (e), insert of the overview (f).

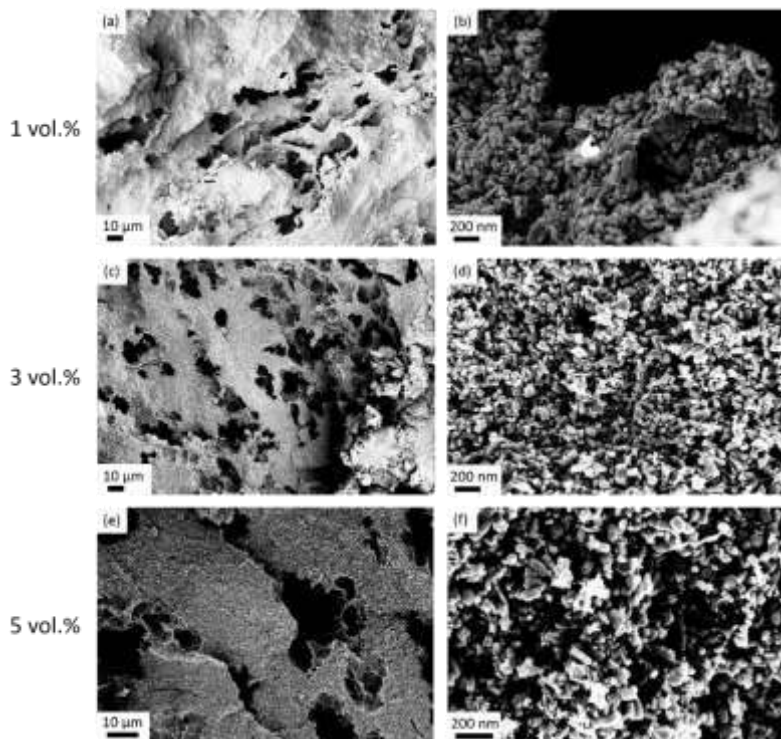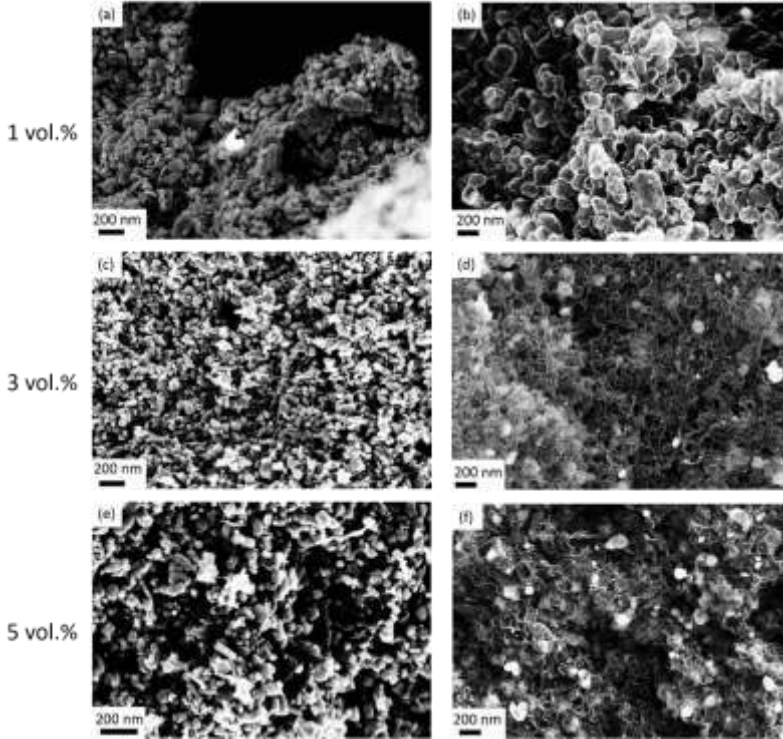Figure 4.34: SEM image of the porous ceramic structure after the sintering process with incorporated TiO_2 (1 vol.%) particles (a), and the corresponding replicated carbon structure (b), SEM image of the ceramic template with 3 vol.% TiO_2 (c), and the corresponding replicated carbon structure (d), SEM image of the ceramic template with 5 vol.% TiO_2 (e), and the corresponding replicated carbon structure (f).

STEM, as shown in Figure 4.35, is used to clarify whether the catalytic additives are coated with carbon, which would cause inactivation for potential applications. In Figure 4.35a, a High Angle Annular Dark Field (HAADF) image of Globugraphite with incorporated TiO_2 is shown. It can be assumed that the particles are mechanically anchored between the carbon shells.

The analysis of the elemental composition of the incorporated catalysts (Figure 4.35b,c) confirms that a reduction of TiO_2 to its metal does not occur. STEM observations of MgO are shown in Figure A9. Palladium also remains in the carbon structure after the replication process, as shown in Figure 4.35d,e.
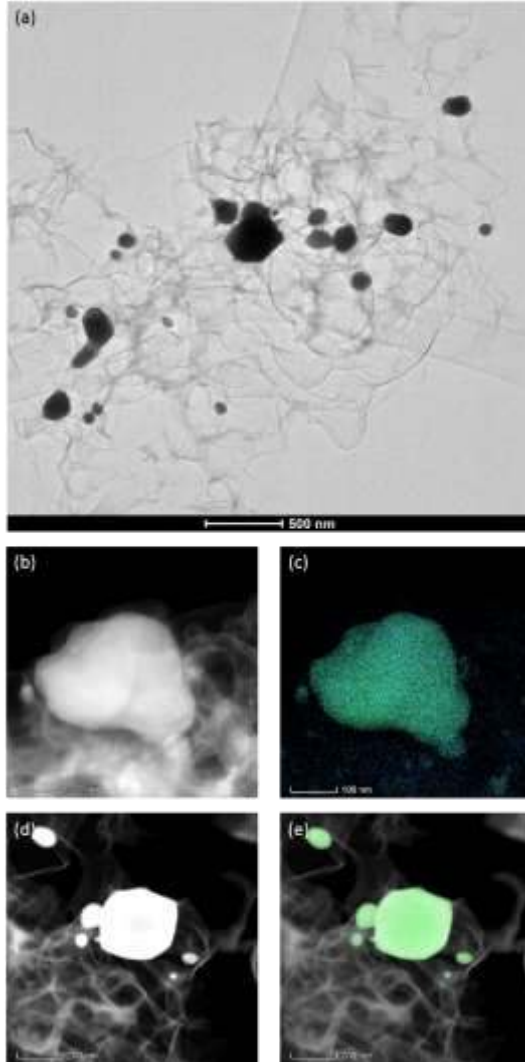
Figure 4.35: TEM overview of incorporated Pd (a), HAADF of Globugraphite with catalytic particles (5 vol% TiO_2) (b), and the respective material combustion oxygen (blue), titanium (green) (c); HAADF of Globugraphite with incorporated Pd (d), and the respective material combustion (Pd-green) (e).

The residues of incorporated catalytic additives are analysed using TGA technique, as presented in Figure 4.35. It should be mentioned that a ZnO content of ~9 wt.% remains in Globugraphite. TGA spectra exhibit a continuously increasing amount of the remaining residues (Figure 4.35a,b). The corresponding spectrum for Pd is shown in Figure A10. However, these data do not provide any information about partial occurred reduction processes of the added particles by hydrogen. The calculated mass fraction of the catalytically active additives as given in the CVD process and after TGA analysis are plotted in Figure 4.35c,d. The ZnO content of 9 wt.% was subtracted from the obtained residues. These calculations confirm the previously made SEM and TEM observations that a reduction of the catalytic particles does not occur. Moreover, a continuous increase of residues is observed. Consequently, a reduction of the added particles can be excluded. However, the slight differences between the initial mass and the calculated mass fraction after TG analysis are based on inhomogenities, which occur during the mixing and pressing process for the manufacturing of the green bodies.
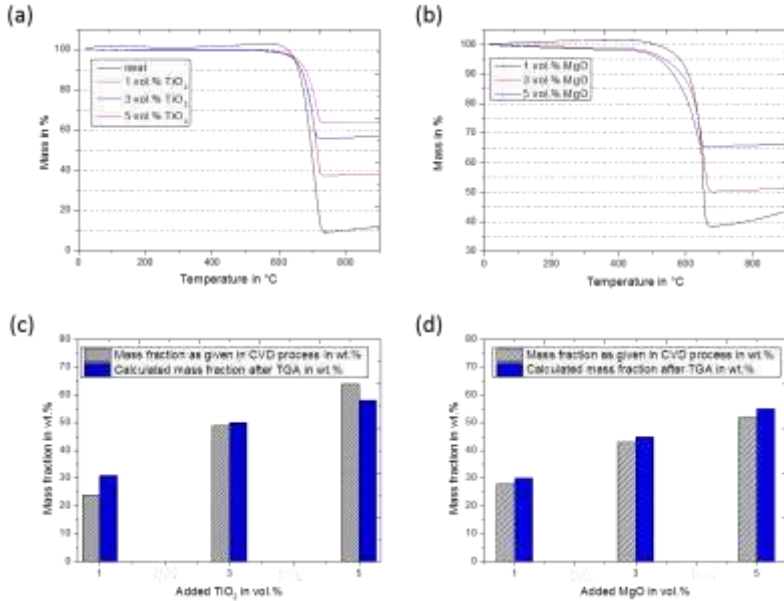
Figure 4.36: Exemplary TGA spectra of neat Globugraphite and Globugraphite-catalysts with incorporated TiO_2 (a) and MgO (b), calculated mass fraction of as given catalytic additive in the CVD process and after TGA measurements for TiO_2 (c) and MgO (d).

The grain size distribution versus the measured grain size is plotted in Figure 4.37 for TiO_2, MgO and Pd. The grain size distribution is calculated by measuring TEM images and counting about 100 particles. TiO_2 and Pd shows a maximum grain size of >300 nm and a main size of 50-200 nm (Figure 4.37a). The reduction of the particle size compared to the as received powder can be explained by the milling and sieving during the green body manufacturing. In general, it should be noted that by decreasing of particle size, the effective surface area of the potential catalytic particle increases. The grain size of incorporated MgO particles, as presented in Figure 4.37b,

123

decreases to a main size of 10-30 nm and a maximum grain size of >60 nm is reached for less than 2.35 %. The incorporation of TiO_2 or Pd particles leads to a significant decrease in the SSA from 376 m²/g of the carbon structure without incorporated particles to 225 m²/g (5 vol.% TiO_2) and respectively 104 m²/g (1 vol.% Pd). In reverse, the effective SSA of catalyst particles increases equally. Due to the added particles, a splitting of the main pore size is observed to 1.9 nm and 2.6 nm (Figure A11), which is contrary to neat Globugraphite.

Figure 4.37: Grain size distribution of incorporated TiO_2 and Pd (a), MgO (b).
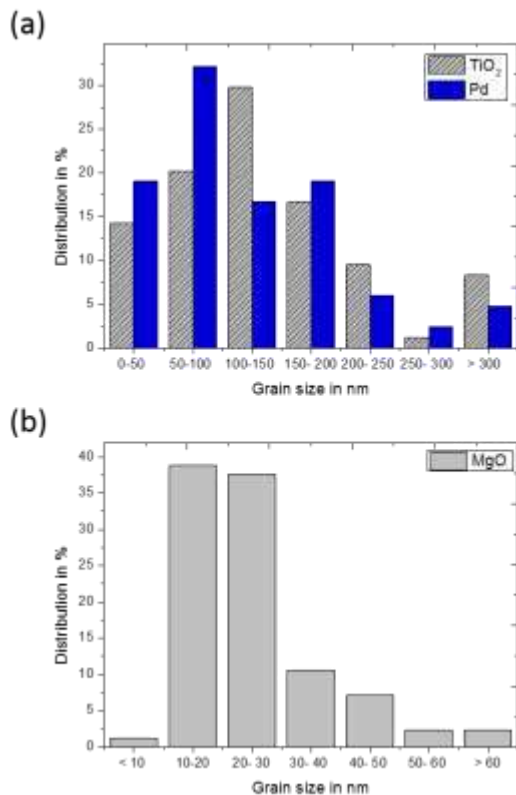
By calculating the Gibbs free energies for other metal oxides, it can be assumed that metal oxides such as Al_2O_3, CuO, CeO_2, Cr_2O_3, OsO_4, V_2O_5 and Co_3O_4 can be added to ZnO/PVB and used as catalysts. Furthermore, it is noteworthy, that any metal with a boiling point > 900 °C can be used as catalytic additives.

5   Conclusion

The aim of this thesis was the investigation of the occurred growth process to synthesise Aerographite in CVD process. Moreover, fundamental structure property relations were analysed. The following chapter summarised the main findings of this work.

The fundamentals of the growth mechanism of Aerographite was determined via ex-situ observations using interrupted syntheses and intense SEM/TEM/Raman techniques. The growth of Aerographite is based on the deposition of amorphous carbon on ZnO template during the CVD process and the simultaneously stepwise removal of the template by its reduction to gaseous Zn. This removal starts at the tetrapodal base ad follows alongside to its tips. In conclusion, the growth process of Aerographite is unique, but can be also referred as a combination of growth processes of graphene and CNTs. Meanwhile the replication of the template morphology starts at the energetically favourable point, the tetrapod base and follows along the scaffolds to its tip.

Additionally, to this mimicry of the template morphology, the graphitisation of the deposited carbon into short graphitic layers via a catalytic graphitisation with gaseous Zn as catalyst was found as key parameter of this unique replication process. Because of the knowledge of the diffusion and the catalysis of Zn through the carbon wall, as received Aerographite exhibits an I_D/I_G ratio of >1, which corresponds with a high defect density.

The Gibbs free energy was calculated based on the estimated reactions. The replication process at 760 °C has a Gibbs free energy of about -239 kJ/mol. Hence, the replication process takes place under energy release.

Besides, to the observed growth process of Aerographite via ex-situ analysis, the CFD simulation is an effective method to determine the occurred flow and temperature behaviour in the CVD reactor. These results exhibit a closed loop of gases in the reactor, which is caused by the temperature. Moreover, the convection is the main factor affecting the flow behaviour.

Based on the investigated growth mechanism, the wall thickness of Aerographite was tailored by varying of the injection time of the carbon source. This synthesis method preserved the tetrapodal morphology of Aerographite, which offers a clear advantage compared to the variation of the carbon injection rate, which leads to a change in the morphology (hollow framework Aerographite to closed-shell filled Aerographite). Based on these results, the structure-property relation between the electrical conductivity and the wall thickness of Aerographite was investigated. Resulting from these observations, a fundamental equation for the description of the electrical conductivity was developed.

The tailored wall thickness of Aerographite also affect the mechanical behaviour of Aerographite-epoxy composites in three-point bending tests. Here, differences of few nanometers were already measurable. It could be shown, that with increasing of the wall thickness, which corresponds to a minimal crystalline width, a maximal fracture toughness was reached. Due to the graphitisation and the increased crystalline width, the mechanical characteristics were reduced. Based on these observations, a fracture model was developed.

For the application as catalysts, the morphology of Aerographite was modified by a newly developed manufacturing method. This method is based on the manufacturing of a highly porous ceramic body with a hierarchical structure by mixing of powder, pressing and sintering. By adding other metal oxides or metals in the mixing process, a wide range of carbon foam-based catalysts with incorporated catalytic additives can be produced. These additives were chosen based on their calculated Gibbs free energy of a possible reduction by hydrogen. However, this carbon structure with incorporated particles distinguish oneself, compare to other carbon-catalyst foam by the reclaiming of these particles by thermal oxidation in an oxygen atmosphere. Consequently, a wide range of catalysts for several processes can be produced just by varying the added catalytically additives, which makes this manufacturing method suitable for an industrial production.

6   Outlook

This work showed fundamental aspects of the growth mechanism and structure-property relations of Aerographite. Due to its unique manufacturing process and alone standing properties, Aerographite and Aerographite-applications will be further investigated.

The following DFG project ("Hochporöse 3-dimensionale Kohlenstoff-Aeromaterialien für energieeffiziente, ultraschnelle und selektive Gasdurchflusssensoren") analyse the growth process of Aerographite and the role of ZnO/Zn in more detail. Therefore, an adapted CVD reactor was developed for the In-beamline analysis at DESY (Hamburg), according to their required conditions, as shown in Figure 6.1.
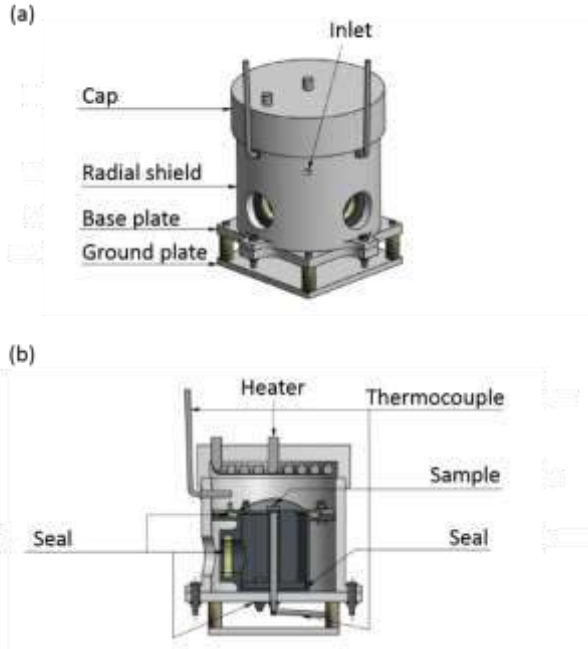
Figure 6.1: Developed CVD reactor for an in-situ analysis of the growth behaviour at DESY (a) and its cross section (b).

Besides to these experimental studies, the simulation via enhanced chemical and CFD techniques is the next step to determine the replication process into the carbon foam. Besides to the analysis of growth processes, the DFG project investigates fundamental structure-property relations, which are a key parameter for tailoring of properties, regarding to applications such as gas sensors and thermoelectric devices. Application-dependent tailored electrical and thermal conductivities for gas sensors and thermoelectric devices will be developed, based on the results of this work, regarding to the influence wall thickness and graphitisation.

Therefore, it is necessary to analyse the charge career densities of Aerographite via Hall measurements. Based on these results in combination with the measured defect density and sp²/sp³ amount (Raman spectroscopy, $\lambda \sim 300\text{-}400$ nm) application dependent properties can be tailored.

Finally, Globugraphite and its application as catalyst will be investigated and characterised in more detail. Especially regarding to the catalytically effectivity and specific applications.

Appendix

A   Growth mechanism
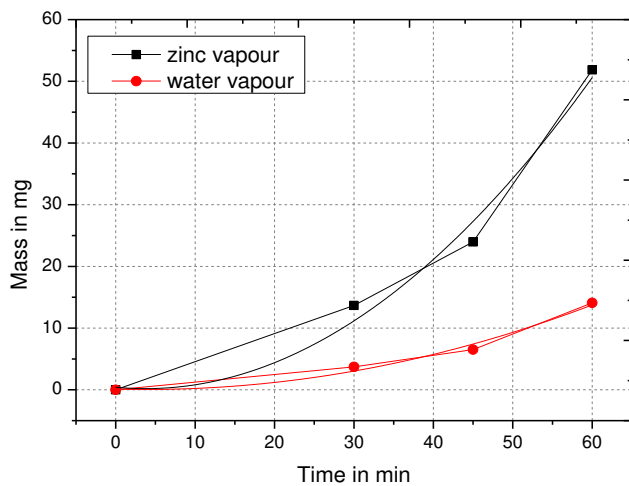
Figure A1: Zinc vapour and water vapour release rate in the 1st reaction stage.
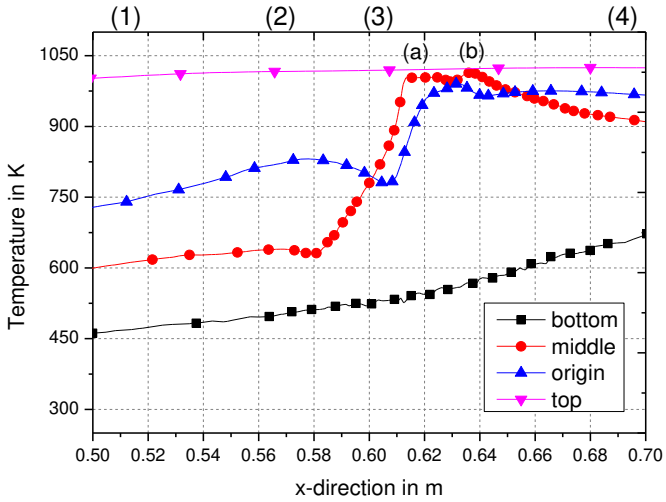
Figure A2: Temperature profile on the silica waver: 1st sample row (a), 2nd sample row (b).

B Basics of thermal treatment
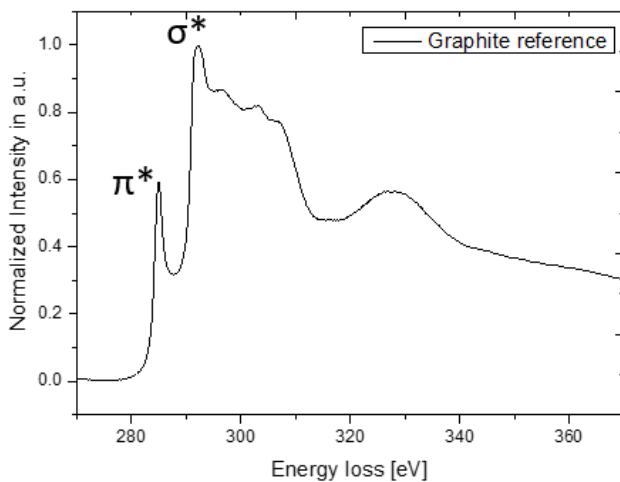
Figure A3: Reference EELS spectra of graphite.

C SEM images of Aerographite with different wall thicknesses
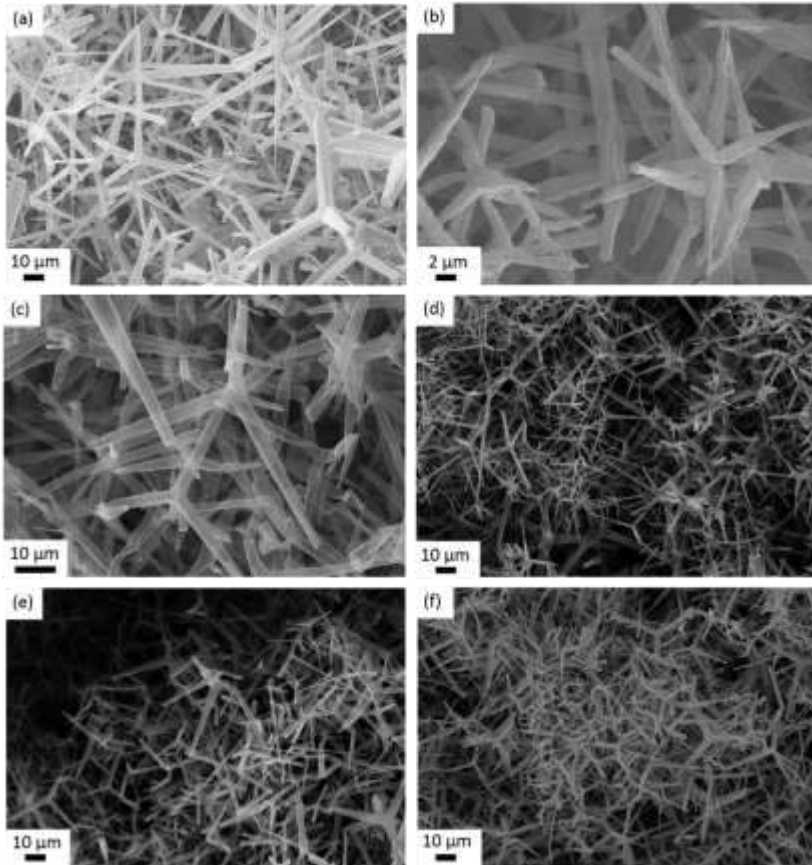
Figure A4: SEM images of neat ZnO (a), different injection times: 15 minutes (b), 20 minutes (c), 45 minutes (d), 60 minutes (e), 60 minutes (f).

D   SEN-3PB tests

Table A1: Overview about the achieved filler contents of Aerographite-epoxy composites for SEN-3PB tests.

Injection time in min	Treatment	Filler content in wt.%
45	Untreated	0.41 ± 0.01
45	Treated	0.39 ± 0.03
60*	Untreated	0.49 ± 0.04
60*	Treated	0.44 ± 0.04
60	Untreated	0.35 ± 0.01
60	Treated	0.32 ± 0.06
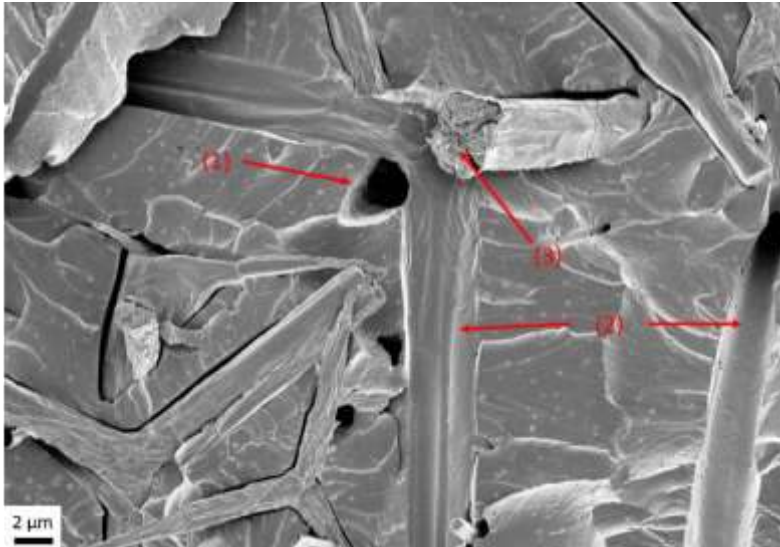
Figure A5: Exemplary fracture surface of treated Aerographite.
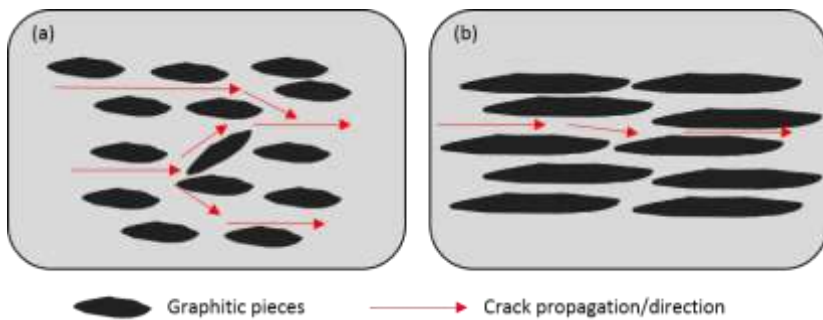
Figure A6: Schematic of crack propagation in untreated Aerographite (a) and thermally treated Aerographite (b).

E   Fundamentals of Globugraphite
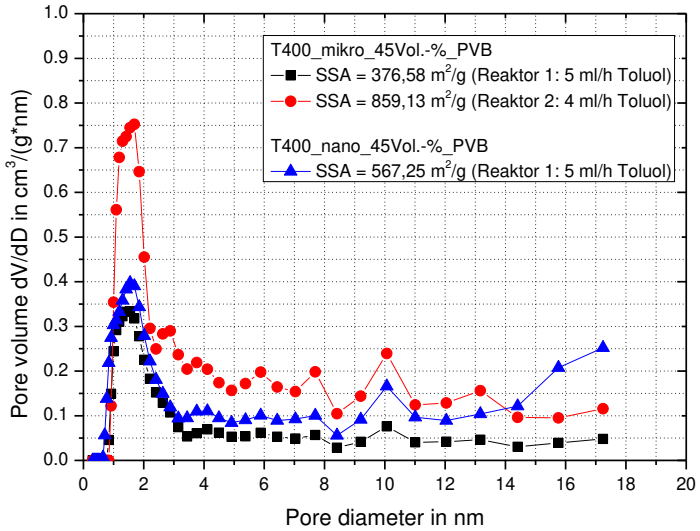
Figure A7: SSA and pore size distribution of Globugraphite.
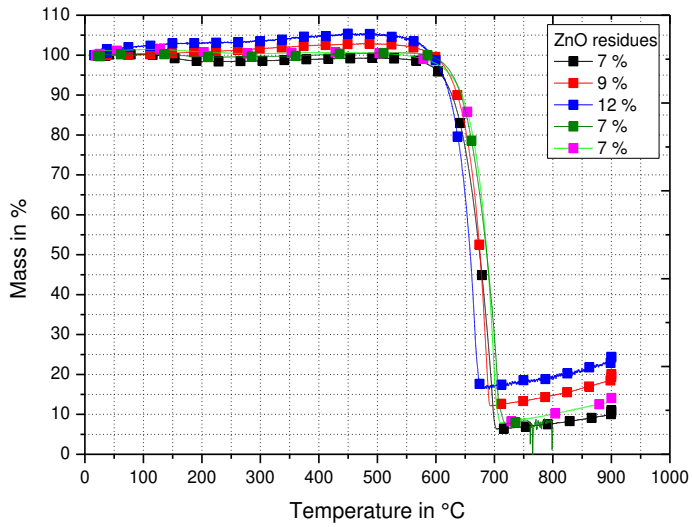
Figure A8: TGA data of Globugraphite containing incorporated ZnO particles.

F   Globugraphite-catalysts
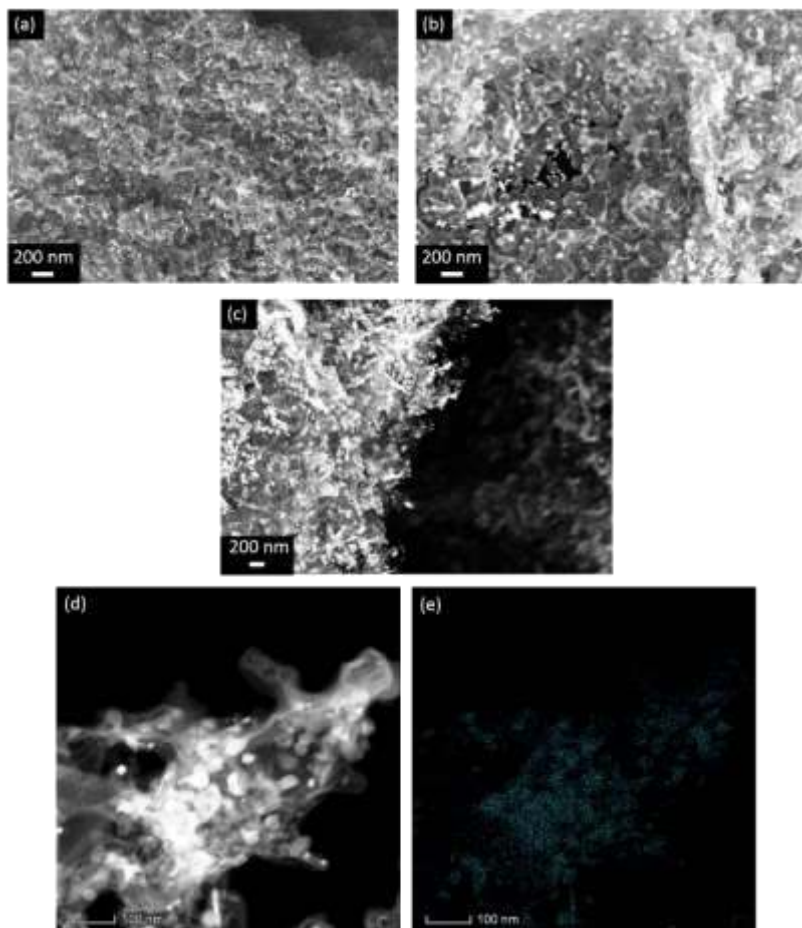
Figure A9: SEM (a)-(c) and STEM (d)-(e) observations of incorporated MgO.
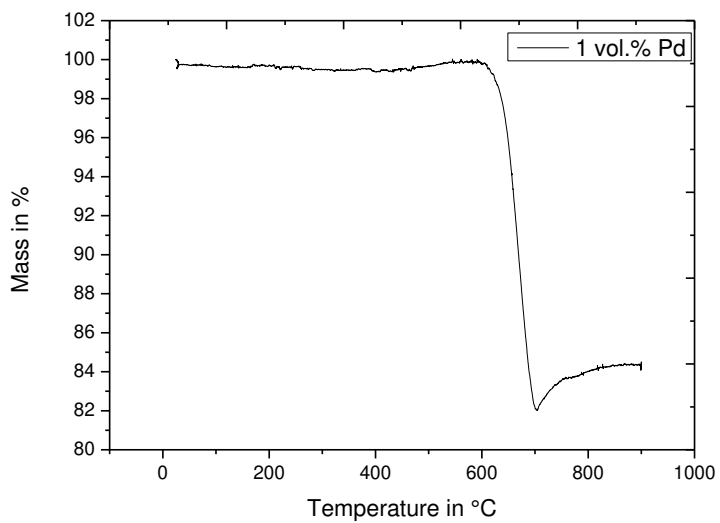
Figure A10: TGA spectra of Globugraphite-catalysts with incorporated Pd.
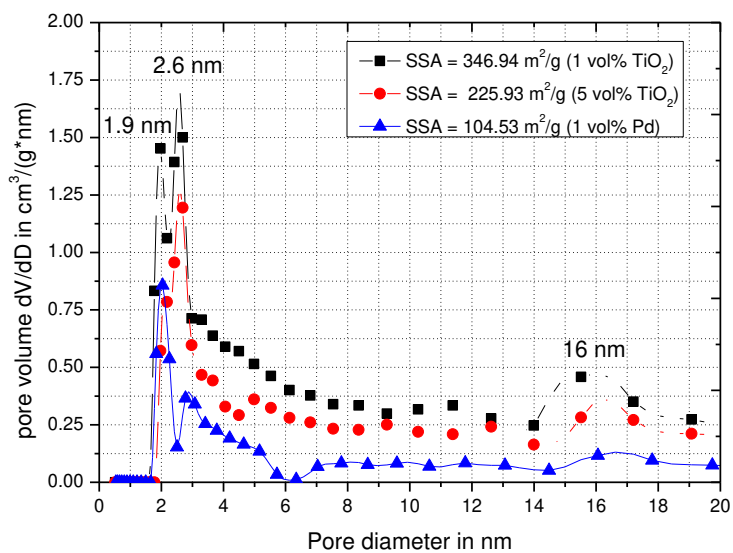
Figure A11: SSA and pore size distribution of Globugraphite with incorporated catalytic particles.

List of supervised student works, with an impact of this thesis

1. Fawcett, Simon: Untersuchung des Einflusses gasförmiger Kohlenstoffderivate (Ethen) und Aerosole auf die Synthese von Aerographit, Bachelorarbeit, August 2016.

2. Timmermann, Johannes: Erstellung und Validierung eines CFD-Modells zur Strömungssimulation eines CVD-Reaktors zur Synthese von 3D vernetzten graphitischen Strukturen, Projektarbeit, August 2016.

3. Löwe Manuel: Konstruktion eines CVD-Reaktors für die In-Beamline-Analyse am DESY, Bachelorarbeit, Februar 2017.

4. Lewke, Marcel: Synthese von Aerographit mit geringen Wandstärken, Bachelorarbeit, Februar 2017.

5. Beisch, Hubert: Evaluation verschiedener Template für die Synthese von 3-dimensionalen Graphitstrukturen (Aerographit) und Charakterisierung der mechanischen und elektrischen Eigenschaften, Masterarbeit, Februar 2017.

6. Wilhelmy, Felix: 3D interconnected globular carbon structures with Me/Me$_x$O$_y$ particles for catalysts, Projektarbeit, August 2017.

7. Brouschkin, Alexander, Einfluss der Wandstärke und Graphitisierung von Aerographit auf die elektro-mechanischen

Eigenschaften von Polymernanokompositen, Projektarbeit, Januar 2018.

8. Roth, Sebastian: Einfluss der Wandstärke und Graphitisierung auf die mechanischen Eigenschaften von Aerographit-Epoxy-Kompositen, Bachelorarbeit, Februar, 2018.

9. Berns, Jan-Christoph: Untersuchung des Einflusses der Zinkverdampfung bei der Synthese von Aerographit auf die Ausbildung der Mikroströmung im CVD Prozess, Masterarbeit, April 2018.

10. Fachri, Abasin: Untersuchung des Einflusses der Probenposition auf die Ausbildung des Temperaturregimes in einer CFD Simulation, Bachelorarbeit, Mai, 2018

7   References

[1] M. Reibold, P. Paufler, A.A. Levin, W. Kochmann, N. Pätzke, D.C. Meyer, Carbon nanotubes in an ancient Damascus sabre, Nature 444, (2006), 286.

[2] L. Radushkevich, V. Lukyanovich, O strukture ugleroda, obrazujucegosja pri termiceskom razlozenii okisi ugleroda na zeleznom kontakte, Zhurnal Fiz. Khimii 12, (1952), 88–95.

[3] S. Iijima, Helical microtubules of graphitic carbon, Letters to Nature 354, (1991), 56–58.

[4] M.J. Yacaman, M.M. Yoshida, L. Rendon, J.G. Santiesteban, Catalytic growth of carbon microtubules with fullerene structure, Appl. Phys. Lett. 1993, 62, 657–659.

[5] H.W. Kroto, J.R. Heath, S.C. Obrien, R.F. Curl, R.E. Smalley, C60 - Buckminsterfullerene, Nature 318, (1985), 162–163.

[6] K.S. Novoselov, AK. Geim, S.V. Morozov, D. Jiang, Y. Zhang, S.V. Dubonos, I.V. Grigorieva, A.A. Firsov, Electric Field Effect in Atomically Thin Carbon Films, Science, 306, (2004), 666–669.

[7] A.K. Geim, K.S. Novoselov, The rise of graphene, nature materials, Vol. 6, (2007), 183–191.

[8] K.S. Karimov, M. Abid, M. Saleem, K.M. Akhmedov, M.M. Bashir, U. Shafique, et al., Temperature gradient sensor based on CNT composite, Physica B 446, (2014), 39–42.

[9] M.A. Hussain, A. Maqbool, F.A. Khalid, N. Bakhsh, A. Hussain, J.U. Rahman, et al., Mechanical properties of CNT reinforced hybrid functionally graded materials for bioimplants, Trans. Nonferrous Met. Soc. China, 24, (2014), 90–98.

References

[10] A. Allaoui, S. Bai, H.M. Cheng, J.B. Bai, Mechanical and electrical properties of a MWNT/epoxy composite, Compos Sci Technol 62, (2002), 1993–1998.

[11] E.T. Thostenson, T.-W. Chou, On the elastic properties of carbon nanotube-based composites: modelling and characterization, J Phys D: Appl Phys 36, (2003), 573–582.

[12] J. Liao and M.-J. Tan, A simple approach to prepare Al/CNT composite: Spread–Dispersion (SD) method, Materials Letters 65, (2011), 2742–2744.

[13] S. Yang, G. Huang, S. Hua, X. Hou, Y. Huang, M. Yue, G. Lei, Improved electro chemical performance of the Li1.2Ni0.13Co0.13Mn0.54O2 wired by CNT networks for lithium-ion batteries, Materials Letters, 118, (2011), 8–11.

[14] Q. Wang, Q. Yao, J. Chang, L. Chen, Enhanced thermoelectric properties of CNT/PANI composite nanofibers by highly orienting the arrangement of polymer chains, J. Mater. Chem. 22, 34, (2012), 17612.

[15] C. Yu, L. Shi, Z. Yao, D. Li, A. Majumdar, Thermal conductance and thermopower of an individual single-wall carbon nanotube, Nano Letters 5, 9, (2005), 1842–1846.

[16] J. Safari, S. Gandomi-Ravandi, Carbon nanotubes supported by titanium dioxide nanoparticles as recyclable and green catalyst for mild synthesis of dihydropyrimidinones/thiones, Journal of Molecular Structure 1065-1066, (2014), 241–247.

[17] W. Han, Z. Tang, P. Zhang, G. Lu, X. Pan, Fabrication and catalytic properties of Pd and Ce decorated carbonnanotube-TiO2composite catalysts for low-temperature CO oxidation, Colloids and Surfaces A: Physicochemical and Engineering Aspects 460, (2014), 422–428.

[18] P.K. Seelam, M. Huuhtanen, A. Sápi, M. Szabó, K. Kordás, E. Turpeinen, G. Tóth, R.L. Keiski, CNT-based catalysts for H2 production by ethanol reforming, International Journal of Hydrogen Energy 35, 22, (2010), 12588–12595.

[19] S. Iijima, P.M. Ajayan, T. Ichihashi, Growth Model of Carbon Nanotubes, Physical Review Letters, 69, (1992), 3100–3103.

[20] S. Iijima, Growth of carbon nanotubes, Materials Science and Engineering, B19, (1993), 172–180.

[21] H. Hashimoto, T. Naiki, T. Eto K. Fujiwara, High temperature gas reaction specimen chamber for an electron microscope, Jpn. J. Appl. Phys., 7, (1968), 946–952.

[22] R.T.K. Baker P.S. Harris, Controlled atmosphere electron-microscopy, J. Phys., E5, (1972), 793–797.

[23] E.D. Boyes, P. Gail, Environmental high resolution electron microscopy and applications to chemical science, Ultramicroscopy, 67, (1997), 219–232.

[24] R. Sharma, Z. Iqbal, In situ observations of carbon nanotube formation using environmental transmission electron microscopy, Appl. Phys. Lett. 84, 6, (2004), 990–992.

[25] R. Sharma, P. Rez, M.M.J. Treacy, S.J. Stuart, In situ observation of the growth mechanisms of carbon nanotubes under diverse reaction conditions, Journal of electron microscopy 54, 3, (2005), 231–237.

[26] X. Feng, S.W. Chee, R. Sharma, K. Liu, X. Xie, Q. Li, S. Fan, K. Jiang, In Situ TEM observation of the gasification and growth of carbon nanotubes using iron catalysts, Nano Res. 4, 8, (2011), 767–779.

[27] Z. Chen, W. Ren, L. Gao, B. Liu, S. Pei, H.-M. Cheng, Three-dimensional flexible and conductive interconnected graphene networks grown by chemical vapour deposition, Nat Mater 10, 6, (2011), 424–428.

References

[28] M. Mecklenburg, A. Schuchardt, Y.K. Mishra, S. Kaps, R. Adelung, A. Lotnyk, L. Kienle, K. Schulte, Aerographite: Ultra Lightweight, Flexible Nanowall, Carbon Microtube Material with Outstanding Mechanical Performance, Advanced Materials 24, (2012), 3486–3490.

[29] G. Xuchun, W. Jinquan, W. Kunlin, C. Anyuan, Z. Hongwei, J. Yi, S. Qinke, W. Dehai, Carbon Nanotube Sponges, Adv. Mater., 22, (2010), 617–621.

[30] Y. Shibing, F, Jiachun, W. Peiyi, Deposition of Three-Dimensional Graphene Aerogel on Nickel Foam as a Binder-Free Supercapacitor Electrode, ACS Appl. Mater. Interfaces, 5, (2013), 7122–7129.

[31] X. Zhang, Z. Sue, B. Xu, S. Yue, Y. Luo, W. Zhan, B. Liu, Mechanically strong and highly conductive graphene aerogel and its use as electrodes for electrochemical power sources, J.Mater.Chem, 21, (2011), 6494–6497.

[32] J. Kuang, L. Liu, Y. Gao, D. Zhou, Z. Chen, B. Han, Z. Zhang, A hierarchically structured graphene foam and its potential as a large-scale strain-gauge sensor, Nanoscale 3, (2013), 12171–12177.

[33] C. Lamprecht, M. Taale, I. Paulowicz, H. Westerhaus, C. Grabosch, A. Schuchardt, M. Mecklenburg, M. Böttner, R. Lucius, K. Schulte, R. Adelung, C. Selhuber-Unkel, A Tunable Scaffold of Microtubular Graphite for 3D Cell Growth, ACS applied materials & interfaces 8, 24, (2016), 14980–14985.

[34] S. Garlof, T. Fukuda, M. Mecklenburg, D. Smazna, Y.K. Mishra, R. Adelung, K. Schulte, B. Fiedler, Electro-mechanical piezoresistive properties of three dimensionally interconnected carbon aerogel (Aerographite)-epoxy composites, Composites Science and Technology 134, (2016), 226–233.

[35] S. Garlof, M. Mecklenburg, D. Smazna, Y.K. Mishra, R. Adelung, K. Schulte, B. Fiedler, 3D carbon networks and their polymer composites, Fabrication and electromechanical investigations of under compressive load neat Aerographite and Aerographite-based PNCs, Carbon 111, (2017), 103–112.

[36] O. Lupan, V. Postica, M. Mecklenburg, K. Schulte, Y.K. Mishra, B. Fiedler, R. Adelung, Low powered, tunable and ultra-light aerographite sensor for climate relevant gas monitoring, J. Mater. Chem. A 4, 42, (2016), 16723–16730.

[37] O. Parlak, Y.K. Mishra, A. Grigoriev, M. Mecklenburg, W. Luo, S. Keene, A. Salleo, K. Schulte, R. Ahuja, R. Adelung, A.P.F. Turner, A. Tiwari, Hierarchical Aerographite nano-microtubular tetrapodal networks based electrodes as lightweight supercapacitor, Nano Energy 34, (2017), 570–577.

[38] A. Schuchardt, T. Braniste, Y.K. Mishra, M. Deng, M. Mecklenburg, M.A. Stevens-Kalceff, S. Raevschi, K. Schulte, L. Kienle, R. Adelung, I. Tiginyanu, Three-dimensional Aerographite-GaN hybrid networks: Single step fabrication of porous and mechanically flexible materials for multifunctional applications, Scientific Reports 5, (2015), 8839.

[39] G. Chen, D.N. Futaba, S. Sakurai, M. Yumura, K. Hata, Interplay of wall number and diameter on the electrical conductivity of carbon nanotube thin films, Carbon 67, (2014), 318–325.

[40] M.R. Golobostanfard, H. Abdizadeh, Influence of carbon nanotube wall thickness on performance of dye sensitized solar cell with hierarchical porous photoanode, Microporous and Mesoporous Materials 191, (2014), 74–81.

[41] E. Castillejos, B. Bachiller-Baeza, M. Pérez-Cadenas, E. Gallegos-Suarez, I. Rodríguez-Ramos, A. Guerrero-Ruiz, K. Tamargo-Martinez,

A. Martinez-Alonso, J.M.D. Tascón, Structural and surface modifications of carbon nanotubes when submitted to high temperature annealing treatments, Journal of Alloys and Compounds 536, (2012), 460–463.

[42] K. Behler, S. Osswald, H. Ye, S. Dimovski, Y. Gogotsi, Effect of Thermal Treatment on the Structure of Multi-walled Carbon Nanotubes, J Nanopart Res 8, 5, (2006), 615–625.

[43] Y.A. Kim, T. Hayashi, K. Osawa, M.S. Dresselhaus, M. Endo, Annealing effect on disordered multi-wall carbon nanotubes, Chemical Physics Letters 380, 3-4, (2003), 319–324.

[44] J. Zhao, Y. Zhang, Y. Su, X. Huang, L. Wei, E.S.-W- Kong, Y. Zhang, Structural improvement of CVD multi-walled carbon nanotubes by a rapid annealing process, Diamond and Related Materials 25, (2012), 24–28.

[45] P.R. Wallace, The Band Theory of Graphite, Phys. Rev. 71, 9, (1947), 622–634.

[46] C. Lee, X. Wei, J.W. Kysar, J. Hone, Measurement of the elastic properties and intrinsic strength of monolayer graphene, Science (New York, N.Y.) 321, 5887, (2008), 385–388.

[47] A.A. Balandin, S. Ghosh, W. Bao, I. Calizo, D. Teweldebrhan, F. Miao, C.N. Lau, Superior thermal conductivity of single-layer graphene, Nano Letters 8, 3, (2008), 902–907.

[48] S. Chandrasekaran, W.V. Liebig, M. Mecklenburg, B. Fiedler, D. Smazna, R. Adelung, K. Schulte, Fracture, failure and compression behaviour of a 3D interconnected carbon aerogel (Aerographite) epoxy composite, Composites Science and Technology 122, (2016), 50–58.

[49] S. Chandrasekaran, C. Seidel, K. Schulte, Preparation and characterization of graphite nano-platelet (GNP)/epoxy nano-composite:

Mechanical, electrical and thermal properties, European Polymer Journal 49, 12, (2013), 3878–3888.

[50] D.A.C. Brownson, D.K. Kampouris, E.C. Banks, An overview of graphene in energy production and storage applications, Journal of Power Sources 196, 11, (2011), 4873–4885.

[51] T. Palaniselvam, J.B. Baek, Graphene based 2D-materials for supercapacitors, 2D Mater. 2, 3, (2015), 32002.

[52] S. Ci, P. Cai, Z. Wen, J. Li, Graphene-based electrode materials for microbial fuel cells, Sci. China Mater. 58, 6, (2015), 496–509.

[53] M. Pumera, Graphene in biosensing, Materials Today 14, 7-8, (2011), 308–315.

[54] H. Park, S. Chang, X. Zhou, J. Kong, T. Palacios, S. Gradecak, Flexible graphene electrode-based organic photovoltaics with record-high efficiency, Nano Letters 14, 9, (2014), 5148–5154.

[55] X.-Y. Fang, X.-X. Yu, H.-M. Zheng, H.-B. Jin, L. Wang, M.-S. Cao, Temperature- and thickness-dependent electrical conductivity of few-layer graphene and graphene nanosheets, Physics Letters A 379, 37, (2015), 2245–2251.

[56] A.I. Romanenko, O.B. Anikeeva, V.L. Kuznetsov, A.N. Obrastsov, A.P. Volkov, A.V. Garshev, Quasi-two-dimensional conductivity and magnetoconductivity of graphite-like nanosize crystallites, Solid State Communications 137, 11, (2006), 625–629.

[57] Z. Yan, D.L. Nika, A.A. Balandin, Thermal properties of graphene and few-layergraphene: applications in electronics, IET Circuits, Devices & Systems 9, 1, (2015), 4–12.

[58] S. Ghosh, W. Bao, D.L. Nika, S. Subrina, E.P. Pokatilov, C.N. Lau, A.A. Balandin, Dimensional crossover of thermal transport in few-layer graphene, nature materials 9, 7, (2010), 555–558.

[59] C.-F. Yu, K.-L. Chen, H.-C. Cheng, W.-H. Chen, A study of mechanical properties of multi-layered graphene using modified Nosé–Hoover based molecular dynamics, Computational Materials Science 117, (2016), 127–138.

[60] W.S. Hummers Jr., R.E. Offeman, Preparation of Graphitic Oxide, Journal of the American Chemical Society 80, 6, (1958), 1339.

[61] L. Staudenmaier, Verfahren zur Darstellung der Graphitsäure, Berichte der deutschen chemischen Gesellschaft 31, 2, (1898), 1481–1487.

[62] S.K. Kim, Y. Zhao, H. Jang, S.Y. Lee, J.M. Kim, K.S. Kim, J.-H. Ahn, P. Kim, J.-Y. Choi, B.H. Hong, Large-scale pattern growth of graphene films for stretchable transparent electrodes, Nature 457, 7230, (2009), 706–710.

[63] M. Losurdo, M.M. Giangregorio, P. Capezzuto, G. Bruno, Graphene CVD growth on copper and nickel: role of hydrogen in kinetics and structure, Physical chemistry chemical physics PCCP 13, 46, (2011), 20836–20843.

[64] C.-M. Seah, S.-P. Chai, A.R. Mohamed, Mechanisms of graphene growth by chemical vapour deposition on transition metals, Carbon 70, (2014), 1–21.

[65] S. Wang L. Qiao C. Zhao X. Zhang, J. Chen H. Tian et al., A growth mechanism for graphene deposited on polycrystalline Co film by plasma enhanced chemical vapor deposition, New Journal of Chemistry, 37, (2013), 1616–1622.

[66] L. Gao, W. Ren, J. Zhao, L-P. Ma, Z. Chen, H.-M. Cheng, Efficient growth of high-quality graphene films on Cu foils by ambient pressure chemical vapor deposition, Appl. Phys. Lett. 97, 18, (2010), 183109.

[67] I. Vlassiouk, M. Regmi, P. Fulvio, S. Dai, P. Datskos, G. Eres, S. Smirnov, Role of hydrogen in chemical vapor deposition growth of large single-crystal graphene, ACS Nano 5, 7, (2011), 6069–6076.

[68] H. Hiura, T.W. Ebbesen, J. Fujita, K. Tanigaki, T. Takada, Role of sp3 defect structures in graphite and carbon nanotubes, Nature 367, (1994), 148–151.

[69] T.W. Ebbesen, H.J. Lezec, H. Hiura, J.W. Bennett, H.F. Ghaemi, T. Thio, Electrical conductivity of individual carbon nanotubes, Nature 382, 6586, (1998), 54–56.

[70] J.P. Lu, Elastic Properties of Carbon Nanotubes and Nanoropes, Phys. Rev. Lett. 79, 7, (1997), 1297–1300.

[71] C. Li, T.W. Chou, Elastic moduli of multi-walled carbon nanotubes and the effect of van der Waals forces, Composites Science and Technology 63, 11, (2003), 1517–1524.

[72] K. Tunvir, A. Kim, S.H. Nahm, The effect of two neighboring defects on the mechanical properties of carbon nanotubes, Nanotechnology 19, 6, (2008), 65703.

[73] M. Sammalkorpi, A. Krasheninnikov, A. Kuronen, K. Nordlund, K. Kaski, Mechanical properties of carbon nanotubes with vacancies and related defects, Phys. Rev. B 70, 24, (2004), 245416.

[74] T. Belytschko, S.P. Xiao, R. Ruoff, Effects of Defects on the Strength of Nanotubes: Experimental-Computational Comparisons. Preprint Archive, Physics. Los Alamos, 2002.

[75] M.D. Ganji, A. Fereidoon, M. Jahanshahi, M.G. Ahangari, Investigation of the Mechanical Properties of Multi-Walled Carbon Nanotubes Using Density Functional Theory Calculations, j comput theor nanosci 9, 7, (2012), 980–985.

[76] C. Journet, W.K. Maser, P. Bernier, A. Loiseau, M. Lamyde la Chapelle, S. Lefrant, P. Deniard, R. Lee, J.E. Fischer, Large-scale production of single-walled carbon nanotubes by the electric-arc technique, Letters to Nature 388, (1997), 756–758.

[77] A. Thess, R. Lee, P. Nikolaev, H. Dai, P. Petit, J. Robert, C. Xu, C., Y.H. Lee, S.G. Kim, A.G. Rinzler, D.T. Colbert, G.E. Scuseria, D. Tomanek, J.E. Fischer, R.E. Smalley, Crystalline Ropes of Metallic Carbon Nanotubes, Science 273, 5274, (1996), 483–487.

[78] H. Dai, Carbon nanotubes: opportunities and challenges, Surface Science 500, (2002), 218–241.

[79] H. Dai, A.G. Rinzler, P. Nikolaev, A. Thess, D.T. Colberty, Richard E., Single-wall nanotubes produced by metal-catalyzed disproportionation of carbon monoxide, Chemical Physics Letters 260, 3-4, (1996), 471–475.

[80] S.B. Sinnott, R. Andrews, D. Qian, A.M. Rao, Z. Mao, E.C. Dickey, F. Derbyshire, Model of carbon nanotube growth through chemical vapor deposition, Chemical Physics Letters 315, 1-2, (1999), 25–30.

[81] F.J. Derbyshire, A.E.B. Presland, D.L. Trimm, Graphite formation by the dissolution—precipitation of carbon in cobalt, nickel and iron, Carbon 13, 2, (1975), 111–113.

[82] S.-F. Lee, Y.-P. Chang, L.-Y. Lee, Effect of ZnO catalyst on carbon nanotube growth by thermal chemical vapor deposition, J. Vac. Sci. Technol. B 26, 5, (2008), 1765.

[83] Y. Homma, Gold Nanoparticles as the Catalyst of Single-Walled Carbon Nanotube Synthesis, Catalysts 4, 1, (2014), 38–48.

[84] S. Hofmann, G. Csányi, A.C. Ferrari, M.C. Payne, J. Robertson, Surface diffusion: the low activation energy path for nanotube growth, Physical Review Letters 95, 3, (2005), 36101.

[85] A.-Y. Lo, S.-B. Liu, C.-T. Kuo, Effect of Temperature Gradient Direction in the Catalyst Nanoparticle on CNTs Growth Mode, Nanoscale Research Letters 5, 9, (2010), 1393–1402.

[86] K. Raji and C.B. Sohabin, Theoretical Analysis of the Catalytic Chemical Vapor Deposition Synthesis of Carbon Nanotubes, JMC 1, 2, (2013), 157–164.

[87] M. Li, Z. Xu, Z. Li, Y. Chen, J. Guo, H. Huo, H. Zhou, H. Huangfu, Z. Cao, H. Wang, An experimental and CFD study on gas flow field distribution in the growth process of multi-walled carbon nanotube arrays by thermal chemical vapor deposition, Crystal Research and Technology 51, 12, (2016), 702–707.

[88] E.M.M. Ibrahim, V.O. Khavrus, A. Leonhardt, S. Hampel, S. Oswald, M.H. Rümmeli, B. Büchner, Synthesis, characterization, and electrical properties of nitrogen-doped single-walled carbon nanotubes with different nitrogen content, Diamond and Related Materials 19, 10, (2010), 1199–1206.

[89] M. Tominaga, M. Togami, M. Tsushida, D. Kawai, Effect of N-doping of single-walled carbon nanotubes on bioelectrocatalysis of laccase, Analytical chemistry 86, 10, (2014), 5053–5060.

[90] F. Pourfayaz, Y. Mortazavi, A.-a. Khodadadi, S.H. Jafari, S. Boroun, M.V. Naseh, A comparison of effects of plasma and acid functionalizations on structure and electrical property of multi-wall carbon nanotubes, Applied Surface Science 295, (2014), 66–70.

[91] E.-C. Shin and G.-H. Jeong, Plasma functionalization of as grown carbon nanotubes for efficient dispersion, Thin Solid Films 519, 20, (2011), 7129–7132.

[92] J. Li, Z. Wu, C. Huang, Z. Chen, R. Huang, L. Li, Plasma functionalization for improving dispersion and interfacial bonding of

multi-wall carbon nanotubes in cyanate ester/epoxy nanocomposites, Colloids and Surfaces A: Physicochemical and Engineering Aspects 433, (2013), 173–180.

[93] S. Costa, E. Borowiak-Palen, M. Kruszynska, A. Bachmatiuk, R.J. Kalenczuk, Characterization of carbon nanotubes by Raman spectroscopy, Materials Science-Poland 26, 2, (2008), 433–441.

[94] M. Vázquez-Santos, E. Geissler, K. László, J.-N. Rouzaud, A. Martínez-Alonso, J.M.D. Tascón, Comparative XRD, Raman, and TEM Study on Graphitization of PBO-Derived Carbon Fibers, J. Phys. Chem. C 116, 1, (2011), 257–268.

[95] M.S. Dresselhaus, J. Ado, Perspectives on Carbon Nanotubes and Graphene Raman Spectroscopy, Nano Letters, 10, (2010), 751–758.

[96] M.S. Dresselhaus, A. Jorio, R. Saito, Characterizing Graphene, Graphite, and Carbon Nanotubes by Raman Spectroscopy, Annu. Rev. Condens. Matter Phys. 1, 1, (2010), 89–108.

[97] M.S. Dresselhaus, G. Dresselhaus, A. Jorio, A.G. Souza Filho, R. Saito, aman spectroscopy on isolated single wall carbon nanotubes, Carbon, 40, (2002), 2043–2061.

[98] M.S. Dresselhaus, G. Dresselhaus, R. Saito, A. Jorio, Raman spectroscopy of carbon nanotubes, Physics Reports 409, (2005), 47–99.

[99] A.C. Ferrari, Raman spectroscopy of graphene and graphite: Disorder, electron-phonon coupling, doping and nonadiabatic effects, Solid State Communications 143, 1-2, (2007), 47–57.

[100] J. Robertson, Diamond-like amorphous carbon, Materials Science and Engineering R 37, (2002), 129–281.

[101] R.W. Pekala, Organic aerogels from the polycondensation of resorcinol with formaldehyde, JOURNAL OF MATERIALS SCIENCE 24, (1989), 3221–3227.

[102] P. Campbell (ed.), Graphene Goes 3D: Synthesis, Properties and Applications of Mesoporous Graphene Bulk Materials. 1st ed., 2017.

[103] Y.-C. Yong, X.-C. Dong, M.B. Chan-Park, H. Song, P. Chen, Macroporous and Monolithic Anode Based on Polyaniline Hybridized Three-Dimensional Graphene for High-Performance Microbial Fuel Cells, ACS Nano 6, 3, (2012), 2394–2400.

[104] M.T. Pettes, H. Ji, R.S. Ruoff, L. Shi, Thermal Transport in Three-Dimensional Foam Architectures of Few-Layer Graphene and Ultrathin Graphite, Nano Lett. 12, 6, (2012), 2959–2964.

[105] X. Cao, Y. Shi, W. Shi, G. Lu, X. Huang, Q. Yan, Q. Zhang, H. Zhang, Preparation of Novel 3D Graphene Networks for Supercapacitor Applications, Small 7, 22, (2011), 3163–3168.

[106] E. Singh, Z. Chen, F. Houshmand, W. Ren, Y. Peles, H.-M. Cheng, N. Koratkar, Superhydrophobic Graphene Foams, Small 9, 1, (2013), 75–80.

[107] Z. Chen, C. Xu, C. Ma, W. Ren, H.-M. Cheng, Lightweight and Flexible Graphene Foam Composites for High-Performance Electromagnetic Interference Shielding, Adv. Mater. 25, 9, (2013), 1296–1300.

[108] F. Yavari, Z. Chen, A.V. Thomas, W. Ren, H.-M. Cheng, N. Koratkar, High Sensitivity Gas Detection Using a Macroscopic Three-Dimensional Graphene Foam Network, Sci. Rep. 1, (2011), 166.

[109] N. Li, Z. Chen, W. Ren, F. Li, H.-M. Cheng, Flexible graphene-based lithium ion batteries with ultrafast charge and discharge rates, Proceedings of the National Academy of Sciences of the United States of America 109, 43, (2012), 17360–17365.

[110] G. Ning, Z. Fan, G. Wang, J. Gao, W. Qian, F. Wei, Gram-scale synthesis of nanomesh graphene with high surface area and its

application in supercapacitor electrodes, Chem. Commun. 47, 21, (2011), 5976.

[111]   X. Dong, Y. Cao, J. Wang, M.B. Chan-Park, L. Wang, W. Huang, P. Chen, Hybrid structure of zinc oxide nanorods and three dimensional graphene foam for supercapacitor and electrochemical sensor applications, RSC Adv. 2, 10, (2012), 4364–4369.

[112]   J. Chen, F. Meng, X. Gui, H. Sun, Z. Zeng, Z. Li, Y. Zhou, Z. Tang, The application of a three dimensional CNT-sponge as the counter electrode for dye-sensitized solar cells, Carbon 50, 15, (2012), 5624–5627.

[113]   X. Ge, W. Yang, J. Wang, D. Long, L. Ling, W. Qiao, Flexible carbon nanofiber sponges for highly efficient and recyclable oil absorption, RSC Adv 5, 86, (2015), 70025–70031.

[114]   H. Wang, G. Wang, Y. Ling, F. Qian, Y. Song, X. Lu, S. Chen, Y. Tong, Y. Li, High power density microbial fuel cell with flexible 3D graphene–nickel foam as anode, Nanoscale 5, 21, (2013), 10283.

[115]   Y. Chen, X. Zhang, P. Yu, Y. Ma, Electrophoretic deposition of graphene nanosheets on nickel foams for electrochemical capacitors, Journal of Power Sources 195, 9, (2010), 3031–3035.

[116]   J. Chen, K. Sheng, P. Luo, C. Li, G. Shi, Graphene Hydrogels Deposited in Nickel Foams for High-Rate Electrochemical Capacitors, Adv. Mater. 24, 33, (2012), 4569–4573.

[117]   M. Zhou, T. Lin, F. Huang, Y. Zhong, Z. Wang, Y. Tang, H. Bi, D. Wan, J. Lin, Highly Conductive Porous Graphene/Ceramic Composites for Heat Transfer and Thermal Energy Storage, Adv. Funct. Mater. 23, 18, (2013), 2263–2269.

[118]   H.W. Liang, Q.-F. Guan, L.-F. Chen, Z. Zhu, W.-J. Zhang, S.-H. Yu, Macroscopic-Scale Template Synthesis of Robust Carbonaceous

Nanofiber Hydrogels and Aerogels and Their Applications, Angew. Chem. Int. Ed. 51, 21, (2012), 5101–5105.

[119] S. Barg, F.M. Perez, N. Ni, P. do Vale Pereira, R.C. Maher, E. Garcia-Tuñon, S. Eslava, S. Agnoli, C. Mattevi, E. Saiz, Mesoscale assembly of chemically modified graphene into complex cellular networks, Nat Comms 5, (2014).

[120] Y. Qian, I.M. Ismail, A. Stein, Ultralight, high-surface-area, multifunctional graphene-based aerogels from self-assembly of graphene oxide and resol, Carbon 68, (2014), 221–231.

[121] M.A. Worsley, P.J. Pauzauskie, T.Y. Olson, J. Biener, J.H. Satcher, T.F. Baumann, Synthesis of Graphene Aerogel with High Electrical Conductivity, J. Am. Chem. Soc. 132, 40, (2010), 14067–14069.

[122] H. Hu, Z. Zhao, W. Wan, Y. Gogotsi, J. Qiu, Ultralight and Highly Compressible Graphene Aerogels, Adv. Mater. 25, 15, (2013), 2219–2223.

[123] Z. Xu, Y. Zhang, P. Li, C. Gao, Strong, Conductive, Lightweight, Neat Graphene Aerogel Fibers with Aligned Pores, ACS Nano 6, 8, (2012), 7103–7113.

[124] R.W. Pekala, J.C. Farmer, C.T. Alviso, T.D. Tran, S.T. Mayer, J.M. Miller, B. Dunn, Carbon aerogels for electrochemical applications, Journal of Non-Crystalline Solids 225, (1998), 74–80.

[125] H. Yin, S. Zhao, J. Wan, H. Tang, L. Chang, L. He, H. Zhao, Y. Gao, Z. Tang, Three-Dimensional Graphene/Metal Oxide Nanoparticle Hybrids for High-Performance Capacitive Deionization of Saline Water, Adv. Mater. 25, 43, (2013), 6270–6276.

[126] X. Li, S. Yang, J. Sun, P. He, X. Xu, G. Ding, Tungsten oxide nanowire-reduced graphene oxide aerogel for high-efficiency visible light photocatalysis, Carbon 78, (2014), 38–48.

References

[127]   Z.-S. Wu, S. Yang, Y. Sun, K. Parvez, X. Feng, K. Müllen, 3D Nitrogen-Doped Graphene Aerogel-Supported Fe 3 O 4 Nanoparticles as Efficient Electrocatalysts for the Oxygen Reduction Reaction, J. Am. Chem. Soc. 134, 22, (2012), 9082–9085.

[128]   S. Ye, J. Feng, Self-assembled three-dimensional hierarchical graphene/polypyrrole nanotube hybrid aerogel and its application for supercapacitors, ACS applied materials & interfaces 6, 12, (2014), 9671–9679.

[129]   L. Qiu, J.Z. Liu, S.L.Y. Chang, Y. Wu, D. Li, Biomimetic superelastic graphene-based cellular monoliths, nature communications 2012, 3:1241.

[130]   B. Song, Z. Wu, Y. Zhu, K.-s. Moon, C.P Wong, IEEE 65th Electronic Components and Technology Conference (ECTC), 2015,26 - 29 May 2015, San Diego, CA, USA. Piscataway, NJ, Piscataway, NJ: IEEE, 2015.

[131]   D. Phokharatkul, A. Wisitsoraat, T. Lomas, A. Tuantranont, 3D hollow carbon nanotetrapods synthesized by three-step vapor phase transport, Carbon 80, (2014), 325–338.

[132]   M.F. Ashby, The properties of foams and lattices, Philosophical transactions. Series A, Mathematical, physical, and engineering sciences 364, 1838, (2006), 15–30.

[133]   H. Yang, N. Wang, Y. Ren, L. Cai, Z. Chen, Q. Xu, Supercritical CO2-assisted preparation of 3D graphene-pyrrole/carbon nanotubes/polyaniline Nanoarchitectures for efficient supercapacitor electrodes, Materials Letters 139, (2015), 471–474.

[134]   Z. Chen, C. Xu, C. Ma, W. Ren, H.-M. Cheng, Lightweight and flexible graphene foam composites for high-performance

electromagnetic interference shielding, Advanced materials (Deerfield Beach, Fla.) 25, 9, (2013), 1296–1300.

[135]   C. Moreno-Castilla, F.J. Maldonado-Hódar, Carbon aerogels for catalysis applications: An overview, Carbon 43, 3, (2005), 455–465.

[136]   E. Bekyarova, K. Kaneko, Microporous Nature of Ce,Zr-Doped Carbon Aerogels, Langmuir 15, 21, (1999), 7119–7121.

[137]   F.J. Maldonado-Hódar, C. Moreno-Castilla, J. Rivera-Utrilla, Y. Hanzawa, Y. Yamada, Catalytic Graphitization of Carbon Aerogels by Transition Metals, Langmuir 16, 9, (2000), 4367–4373.

[138]   F.J. Maldonado-Hódar, C. Moreno-Castilla, A.F. Pérez-Cadenas, Catalytic combustion of toluene on platinum-containing monolithic carbon aerogels, Applied Catalysis B: Environmental 54, 4, (2004), 217–224.

[139]   T.F. Baumann, G.A. Fox, J.H. Satcher, N. Yoshizawa, R. Fu, M.S. Dresselhaus, Synthesis and Characterization of Copper-Doped Carbon Aerogels, Langmuir 18, 18, (2002), 7073–7076.

[140]   C.D. Saquing, T.-T. Cheng, M. Aindow, C. Erkey, Preparation of Platinum/Carbon Aerogel Nanocomposites Using a Supercritical Deposition Method, J. Phys. Chem. B 108, 23, (2004), 7716–7722.

[141]   F. Béguin and E. Frackowiak (ed.), Supercapacitors: Materials, Systems, and Applications. Weinheim: Wiley-VCH Verlag GmbH & Co., 2013.

[142]   G. Zu, J. Shen, L. Zou, F. Wang, X. Wang, Y. Zhang, X. Yao, Nanocellulose-derived highly porous carbon aerogels for supercapacitors, Carbon 99, (2016), 203–211.

[143]   L. Wang, Y. Zhou, J. Qiu, Influence of pore structures on the electrochemical performance of asphaltene-based ordered mesoporous carbons, Microporous and Mesoporous Materials 174, (2013), 67–73.

References

[144]   D. Lozano-Castelló, D. Cazorla-Amorós, A. Linares-Solano, S. Shiraishi, H. Kurihara, A. Oya, I nfluence of pore structure and surface chemistry on electric double layer capacitance in non-aqueous electrolyte, Carbon 41, 9, (2003), 1765–1775.

[145]   Y. Huang, F. Lai, L. Zhang, H. Lu, Y.-E Miao, T. Liu, Elastic Carbon Aerogels Reconstructed from Electrospun Nanofibers and Graphene as Three-Dimensional Networked Matrix for Efficient Energy Storage/Conversion, Scientific Reports 6, (2016), 31541.

[146]   L.-Z. Fan, T.-T. Chen, W.-L. Song, X. Li, S. Zhang, High nitrogen-containing cotton derived 3D porous carbon frameworks for high-performance supercapacitors, Scientific Reports 5, (2015), 15388.

[147]   S. Jin, H. Deng, L. Zhan, W. Qiao, L. Ling, Synthesis of 3D hierarchical porous carbon as electrode material for electric double layer capacitors, New Carbon Materials 27, 2, (2012), 87–92.

[148]   Market Report, Global Catalyst Market. 3rd ed., March/2015.

[149]   H.O. Pierson, Handbook of Chemical Vapor Deposition (CVD): Principles, Technology, and Applications. 2nd ed. Norwich, New York: Noyes Publications/William Andrew Publishing, LLC, 1999.

[150]   J. W. Matthews (ed.), Epitaxial growth, Part B. New York, 1975.

[151]   M.J. Hampden-Smith TK, Chemical vapor deposition of metals: Part 1. An overview of CVD processes, Chem. Vap. Deposition, 1, (1995), 8–23.

[152]   K.L. Choy, Chemical vapour deposition of coatings, Progress in Materials Science, 48, (2003), 57–170.

[153]   H.S. Nalwa (ed.), Handbook of nanostructured materials and nanotechnology. 1st ed. San Diego (CA): Academic Press, 2000.

[154]   H. Ur Rashid, K. Yu, M.N. Umar, M.N. Anjum, K. Khan, N. Ahmad, M.T. Jan, CATALYST ROLE IN CHEMICAL VAPOR

162

DEPOSITION(CVD) PROCESS: A REVIEW, Rev. Adv. Mater. Sci. 40, (2015), 235–248.

[155]   K.D. Karlin (ed.), Progress in Inorganic Chemistry: John Wiley & Sons, 1994.

[156]   F.C. Frank, J. H. van der Merwe, One-dimensional dislocations. II. Misfitting monolayers and oriented overgrowth 198, 1053, (1949), 216–225.

[157]   F.C. Frank, J.H. van der Merwe, One-Dimensional Dislocations. I. Static Theory, Proceedings of the Royal Society A: Mathematical, Physical and Engineering Sciences 198, 1053, (1949), 205–216.

[158]   F.C. Frank, J.H. van der Merwe, One-Dimensional Dislocations. III. Influence of the Second Harmonic Term in the Potential Representation, on the Properties of the Model, Proceedings of the Royal Society A: Mathematical, Physical and Engineering Sciences 200, 1060, (1949), 125–134.

[159]   I. N. Stranski, L. Krastanow, Zur Theorie der orientierten Ausscheidung von Ionenkristallen aufeinander, Sitzungsber. Akad. Wiss. Wien. Math.-Naturwiss. 146, (1938), 125–134.

[160]   M. Volmer AW, Keimbildung in übersättigten Gebilden, Z. phys. Chem 119, (1926), 277–301.

[161]   A.C. Jones, M.L. Hitchman (ed.), Chemical Vapour Deposition: Precursors, Processes and Applications. 1st ed. London: Royal Society of Chemistry, 2009.

[162]   B. Salanon, C. Barreteau, M.C. Desjonquères, D. Spanjaard, Energy of defects on surfaces of copper, Computational Materials Science 17, 2-4, (2000), 269–274.

[163]   K. Sangwal, R. Rodríguez - Clemente, "2. Review of Crystal Growth Processes", Solid State Phenomena 17-18, (1991), 11–38.

[164]   Y.K. Mishra, S. Kaps, A. Schuchardt, I. Paulowicz, X. Jin, D. Gedamu, S. Freitag, M. Claus, S. Wille, A. Kovalev, S.N. Gorb, R. Adelung, Fabrication of Macroscopically Flexible and Highly Porous 3D Semiconductor Networks from Interpenetrating Nanostructures by a Simple Flame Transport Approach, Particle & Particle Systems Characterization, 30, (2013), 775–783.

[165]   J. Marx, S. Garlof, H. Beisch, P. Huber, A. Kityk, B. Fiedler, Manufacturing and properties of hierarchical graphitic structuresfor the application as supercapacitors. Lisbon, 2017.

[166]   J. Marx, M.R.D. Lewke, D. Smazna, Y.K. Mishra, R. Adelung, K. Schulte, B. Fiedler, Processing, growth and thermodynamic calculations of carbon foam with a hollow tetrapodal morphology-Aerographite, Applied Surface Science 470, (2019), 535–542.

[167]   H. Salmang, H.Scholze, Keramik. Berlin, Heidelberg: Springer Berlin Heidelberg, 1982.

[168]   AMERICAN SOCIETY FOR TESTING AND MATERIALS, Standard Test Methods for Plane-Strain Fracture Toughness and Strain Energy Release Rate of Plastic Materials, D 5045 – 99: Annual Book of ASTM Standards. [October 26, 2017].

[169]   S. Urbonaite, S. Wachtmeister, C. Mirguet, E. Coronel, W.Y. Zou, S. Csillag, G. Svensson, EELS studies of carbide derived carbons, Carbon 45, 10, (2007), 2047–2053.

[170]   CEMES, IMN laboratories, ESTEEM 2, METSA SFµ, EELS Database. [January 18, 2018]; Available from: https://eelsdb.eu/spectra/.

[171]   M.A. Worsley, S.O. Kucheyev, J.H. Satcher, A.V. Hamza, T.F. Baumann, Mechanically robust and electrically conductive carbon nanotube foams, Appl. Phys. Lett. 94, 7, (2009), 73115.

[172]   Y. Feng, H. Zheng, Z. Zhu, F. Zu, The microstructure and electrical conductivity of aluminum alloy foams, Materials Chemistry and Physics, 78, (2002), 196–201.

[173]   K.P. Dharmasena, H.N.G. Wadley, Electrical Conductivity of Open-cell Metal Foams, J. Mater. Res. 17, 03, (2002), 625–631.

[174]   A.V. Neimark, Y. Lin, P.I. Ravikovitch, M. Thommes, Quenched solid density functional theory and pore size analysis of micro-mesoporous carbons, Carbon 47, 7, (2009), 1617–1628.

[175]   S. Chandrasekaran, Development of nano-particle modified polymer matrices for improved fibre reinforced composites. Dissertation. Hamburg, 2014.

[176]   S.A. Esfarjani, S. Dworkin, J. Mostaghimi, B. Simard, K. S. Kim, G. Soucy, A. Shahverdi (ed.), CFD Simulation of Single-walled Carbon Nanotube Growth in an RF Induction Thermal Plasma Process: American Institute of Aeronautics and Astronautics, 2011.

[177]   J.-P. Randin EY, Differential capacitance study on the basal plane of stress-annealed pyrolytic graphite, J. Electroanal. Chem. Interfacial Electrochem. 36, (1972), 257–276.

[178]   B. Marinho, M. Ghislandi, E. Tkalya, C.E. Koning, G. de With, Electrical conductivity of compacts of graphene, multi-wall carbon nanotubes, carbon black, and graphite powder, Powder Technology 221, (2012), 351–358.

[179]   A. Meyer-Plath, G. Orts-Gil, S. Petrov, F. Oleszak, H.-E. Maneck, I. Dörfel, O. Haase, S. Richter, R. Mach, Plasma-thermal purification and annealing of carbonnanotubes, Carbon 50, 10, (2012), 3934–3942.

[180]   E.L.K. Chng, H.L. Poh, Z. Sofer, M. Pumera, Purification of carbon nanotubes by high temperature chlorine gas treatment, Physical chemistry chemical physics PCCP 15, 15, (2013), 5615–5619.

References

[181]   P. Mahalingam, B. Parasuram, T. Maiyalagan, S. Sundaram, Chemical Methods For Purification Of Carbon Nanotubes-A Review, J. Environ. Nanotechnol 1, 1, (2012), 53–61.

[182]   M. Sevilla, A.B. Fuertes, Catalytic Graphitization of carbons by various metals, Carbon, 44, (2006), 468–474.

[183]   A. Oya, S. Otani, Catalytic Graphitization of carbons by various metals, Carbon, 17, (1979), 131–137.

[184]   F. Tuinstra, J.L. Koenig, Raman Spectrum of Graphite, The Journal of Chemical Physics 53, 3, (1970), 1126–1130.

[185]   D.S. Knight, W.B. White, Characterization of diamond films by Raman spectroscopy, J. Mater. Res., 4, 2, (1989), 385–393.

[186]   D.S. Olson, M.A. Kelly, S. Kapoor, S.B. Hagstrom, A mechanism of CVD diamond film growth deduced from the sequential deposition from sputtered carbon and atomic hydrogen, J. Mater. Res., 9, (1994), 1546–1551.

[187]   J. Zhang, P. An Hua, X. Wang, Z. Wang, Structural evolution and growth mechanism of graphene domains on copper foil by ambient pressure chemical vapor deposition, Chemical Physics Letters, 536, (2012), 123–128.

[188]   F.A. Weirich, A Study of Reduction of zinc oxide by hydrogen and methane. Master Theses, 1926.

[189]   J.A. Kitchener, S. Ignatowicz, The reduction equilibria of zinc oxide and zinc silicate with hydrogen, Trans. Faraday Soc., 47, (1951), 1278–1286.

[190]   J.A. Clarke, D.J. Fray, The standard Gibbs free energy of the reaction $Zn(g) + H2O(g) = ZnO(s) + H2(g)$ over the temperature range 900 to 1300 K, J. Chem. Thermodynamics 10, (1978), 892–894.

[191]   J. Marx, J.-C. Berns, C. Spille, M. Mintken, R. Adelung, M. Schlüter, B. Fiedler, A theoretical CFD study of the CVD process for the manufacturing of ahighly porous 3D carbon foam, Chemical Engineering & Technology, (2019).

[192]   R. Beams, L.G. Cancado, L. Novotny, Raman characterization of defects and dopants in graphene, JOURNAL OF PHYSICS: CONDENSED MATTER 27, 8, (2015), 83002.

[193]   J. Marx, H. Beisch, S. Garlof, B. Fiedler, Structural improvement of a bio-inspired 3D globular carbon foam by a continously thermal treatment: A comprehensive study, Advanced Materials Science 2, 4, (2017), 1–7.

[194]   A.C. Ferrari, J.C. Meyer, V. Scardaci, C. Casiraghi, M. Lazzeri, F. Mauri, S. Piscanec, D. Jiang, K.S. Novoselov, S. Roth, A.K. Geim, Raman spectrum of graphene and graphene layers, Physical Review Letters 97, 18, (2006), 187401.

[195]   S. Chandrasekaran, Development of nano-particle modified polymer matrices for improved fibre reinforced composites. Dissertation. Hamburg, 2014.

[196]   T. Tagawa, T. Miyata, Size effect on tensile strength of carbon fibers, Materials Science and Engineering: A 238, 2, (1997), 336–342.

[197]   L. Kong, H. Liu, W. Cao, L. Xu, PAN fiber diameter effect on the structure of PAN-based carbon fibers, Fibers Polym 15, 12, (2014), 2480–2488.

[198]   J. Marx, A. Brouschkin, S. Roth, D. Smazna, Y.K. Mishra, H. Wittich, K. Schulte, R. Adelung, B. Fiedler, Fundamentals of the temperature-dependent electrical conductivity of a 3D carbon foam - Aerographite-, Synthetic Metals 235, (2018), 145–152.

[199]   J.E. Fischer, H. Dai, A. Thess, R. Lee, N.M. Hanjani, D.L. Dehaas, R.E. Smalley, Metallic resistivity in crystalline ropes of single-wall carbon nanotubes, Phys. Rev. B 55, 8, (1997), R4921–R4924.

[200]   Y. Matsuda, J. Tahir-Kheli, W.A. Goddard, Definitive Band Gaps for Single-Wall Carbon Nanotubes, J. Phys. Chem. Lett. 1, 19, (2010), 2946–2950.

[201]   J. Marx, S. Roth, A. Brouschkin, D. Smazna, Y.K. Mishra, K. Schulte, R. Adelung, B. Fiedler, Tailored crystalline width and wall thickness of an annealed 3D carbonfoam composites and its mechanical property, Carbon, 142, (2019), 60–67.

[202]   F.H. Gojny, M.H.G. Wichmann, B. Fiedler, K. Schulte, Influence of different carbon nanotubes on the mechanical properties of epoxy matrix composites - A comparative study, Composites Science and Technology 65, 15-16, (2005), 2300–2313.

[203]   S. Chandrasekaran, N. Sato, F. Tölle, R. Mülhaupt, B. Fiedler, K. Schulte, Fracture toughness and failure mechanism of graphene based epoxy composites, Composites Science and Technology 97, (2014), 90–99.

[204]   J. Marx, F. Wilhelmy, H. Beisch, B. Fiedler, Manufacturing of a hierarchical carbon foam with tailored catalytically Me/MexOy particles, Vacuum, 155, (2018), 490–495.

[205]   B. Fiedler, J. Marx, F. Wilhelmy, Katalysatoren und Filtermaterial mit Metall/Metalloxiden in 3D graphitischen und hierarchischen Strukturen mit hoher spezifischer Oberfläche.

[206]   E. Ventosa, A. Tymoczko, K. Xie, W. Xia, M. Muhler, W. Schuhmann, Low temperature hydrogen reduction of high surface area anatase and anatase/β-TiO$_2$ for high-charging-rate batteries, ChemSusChem 7, 9, (2014), 2584–2589.

[207] R. Sundararaman, C. Song, Catalytic decomposition of benzothiophenic and dibenzothiophenic sulfones over MgO-based catalysts, Applied Catalysis B: Environmental 148-149, (2014), 80–90.

[208] J. Carbajo, M. Jiménez, S. Miralles, S. Malato, M. Faraldos, A. Bahamonde, Study of application of titania catalysts on solar photocatalysis: Influence of type of pollutants and water matrices, Chemical Engineering Journal 291, (2016), 64–73.

[209] NIST, NIST-JANAF Thermochemical Tables. [August 11, 2017]; Available from: http://kinetics.nist.gov/janaf/.

[210] R. Larsen, S. Ha, J. Zakzeski, R.I. Masel, Unusually active palladium-based catalysts for the electrooxidation of formic acid, Journal of Power Sources 157, 1, (2006), 78–84.

[211] X. Xu, K. Shuai, B. Xu, Review on Copper and Palladium Based Catalysts for Methanol Steam Reforming to Produce Hydrogen, Catalysts 7, 6, (2017), 183.

[212] T. Graham, On the Absorption and Dialytic Separation of Gases by Colloid Septa, Phil. Trans. R. Soc. Lond. 156, (1866), 399–439.

Curriculum Vitae

Name:	Marx, Janik
Date of birth:	03.11.1989
Place of birth:	Hermeskeil, Germany

Educational qualifications:

1996-2000	Grundschule Malborn
2000-2003	Regionale Schule Thalfang
2003-2006	Erich-Kästner Realschule Hermeskeil
2006-2010	Gymnasium Hermeskeil, Degree: Abitur
10/2010-12/2013	TU Ilmenau Studies of Materials Science, Degree: B.Sc.
10/2013-10/2015	TU Ilmenau Studies of Materials Science, Degree: M.Sc.
12/2015-02/2018	Research assistant (Wissenschaftlicher Mitarbeiter) at Institute of Polymer and Composites, Hamburg University of Technology (TUHH)
03/2018-05/2018	Post-doc at electron microscopy unit (BEEM), Hamburg University of Technology (TUHH)
06/2018-present	Health regeneration